# Modification of Jet-Properties in Ultrarelativistic d+Au, Cu+Cu and Au+Au Collisions at $\sqrt{s_{NN}} = 200 GeV$

A Dissertation Presented

by

Wolf Gerrit Holzmann

to

The Graduate School

in Partial Fulfillment of the Requirements

for the Degree of

Doctor of Philosophy

in

Chemistry
(Chemical Physics)

Stony Brook University

May 2006

Stony Brook University

The Graduate School

Wolf Gerrit Holzmann

We, the dissertation committee for the above candidate for the Doctor of Philosophy degree, hereby recommend acceptance of the dissertation.

_____
Michael G. White
Professor of Chemistry

_____
Roy A. Lacey
Professor of Chemistry

_____
John M. Alexander
Professor of Chemistry

_____
Mark D. Baker
Brookhaven National Laboratory

This dissertation is accepted by the Graduate School.

_____
Graduate School

ii

# Abstract of the Dissertation

# Modification of Jet-Properties in Ultrarelativistic d+Au, Cu+Cu and Au+Au Collisions at $\sqrt{s_{NN}} = 200 GeV$

by

Wolf Gerrit Holzmann

Doctor of Philosophy

in

Chemistry
(Chemical Physics)

Stony Brook University

2006

A transition from hadronic matter to a plasma of deconfined quarks and gluons (QGP) is predicted to occur for energy densities $\epsilon \approx 0.6 - 1.0 GeV/fm^3$

[Kar02] by Quantum Chromodynamics (QCD), the theory of strong interactions. Such a plasma is believed to have existed only a few $\mu$s after the Big Bang. The production and study of the QGP is the subject of very intense research currently undertaken at the Relativistic Heavy Ion Collider (RHIC) at Brookhaven National Laboratory. Prior to fragmentation into a jet of hadrons, a hard scattered parton can lose energy as it propagates through the high energy density matter formed in heavy ion collisions at RHIC. This energy loss is expected to be sensitive to several properties of the medium including its gluon density, formation time and the path length traversed. The energy loss also results in the modification of jet topologies and yields which in turn serve as a powerful tomographic short-wavelength probe of the collision medium. In this work, the method of two-particle azimuthal correlation functions is used to measure the correlations due to jets and elliptic flow in d+Au, Cu+Cu and Au+Au collisions at $\sqrt{s_{NN}} = 200$GeV. The jet correlations measured in Cu+Cu and Au+Au collisions, are separated via a novel decomposition technique to obtain the jet associated particles per trigger hadron. These distributions show evidence for strong centrality dependent shape modifications for particles of intermediate transverse momentum produced in Cu+Cu and Au+Au collisions but not for d+Au . They also indicate that jet associated protons and mesons (pions and kaons) are similarly modified by the medium. This discovery is compatible with several recent theoretical predictions for jet modification in a strongly interacting

QGP, including the formation of jet- induced "mach cones", reminiscent of the sonic boom produced in a fluid when the speed of sound is exceeded. These new experimental results provide an important basis for further study of the transport properties of the high energy density matter produced in heavy ion collisions at RHIC.

# Contents

# List of Figures

# List of Tables

# Acknowledgments

First and foremost, I am deeply indebted to my research adviser, Roy Lacey, for his patient academic (and personal) guidance over the years. His passion for doing and communicating innovative and creative science has and always will be a great source of inspiration. It has been fun being his student. I am also very grateful to the members of my advancement to candidacy and dissertation committees for helpful feedback and encouragement at the "milestones" along the way. John Alexander deserves my special thanks. His friendly encouragement and advise on many matters scientific and academic have in no small part shaped my development during the last 5-6 years. I am thankful to the (past and present) members of the nuclear chemistry gang. I specially thank N. N. Ajitanand for help with simulations, quality assurance and fruitful discussions and A. Taranenko for discussions, help with calibrations and proof reading an early version of this thesis.

I believe will certainly be more relieved than I about my graduation, further

Joerg, Erwin and the late Martha to whom I dedicate this dissertation.

# Chapter 1

# Introduction

Quantum Chromodynamics (QCD), the theory of strong interaction, predicts that a transition from a phase of ordinary hadronic matter to a color deconfined phase of quarks and gluons, called the Quark Gluon Plasma (QGP), should occur in the high temperature and low density region of the nuclear phase diagram [Shu80]. Figure 1.1 shows results for the energy density ($\epsilon/T^4$) and temperature ($T/T_C$) of QCD matter from lattice gauge theory simulations (Fig. reproduced from Ref. [Han01]). The Stefan-Boltzmann limit is indicated by $\epsilon_{SB}/T^4$. It is noteworthy, that the curve in Fig. 1.1 never reaches the limit for an ideal gas of quarks and gluons. Lattice QCD calculations like those in Figure 1.1 indicate that a critical energy density of $\epsilon_C \approx 0.6 - 1 GeV/fm^3$ and temperature of $T_C \approx 170 MeV$ (*i.e.* of the order of a trillion Kelvin) are needed for QGP creation [Kar02]. Energy densities and temperatures of that magnitude might have existed a few $\mu$s after the

Big Bang. If these conditions could be recreated in the laboratory, it would be possible to gain experimental insight into the evolution of the early universe. When heavy ions are accelerated to almost the speed of light and allowed to collide (cf. Fig. 1.2 (a)), a large amount of energy is released in a small volume, resulting in the production of matter with extremely high energy density as schematically indicated in Fig. 1.2 (b). Therefore, ultra-relativistic heavy ion collisions provide effective pathways to the creation of a QGP.
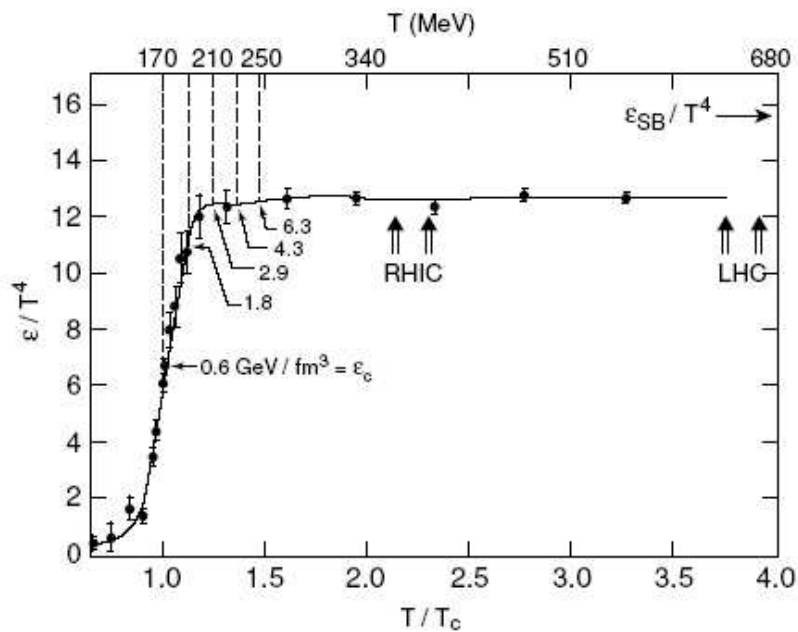


**Figure 1.1:** *Results from lattice gauge theory simulations with three quark flavors. Energy density $\epsilon/T^4$ is plotted versus the temperature $T/T_C$. The Stefan-Boltzmann limit is indicated by $\epsilon_{SB}/T^4$. Figure reproduced from Ref. [Han01].*
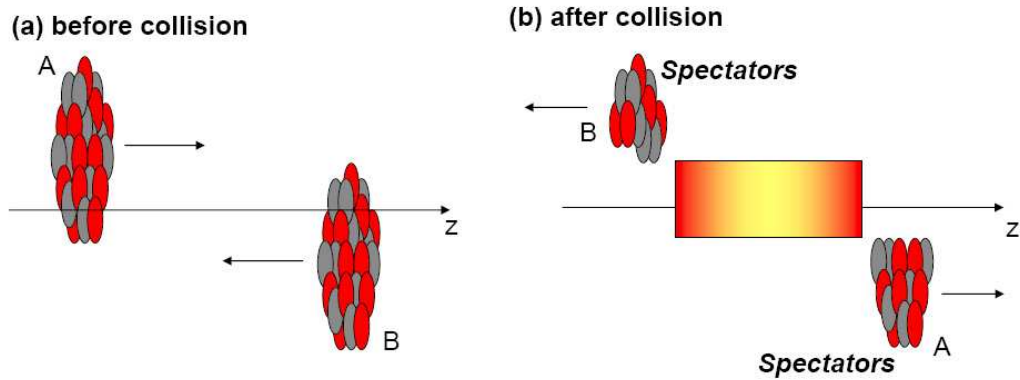
**Figure 1.2:** *Schematic illustration of a heavy ion collision. The nuclei are Lorentz contracted (see text).*

## 1.1 Heavy Ion Collisions as Pathways to a QGP

The Relativistic Heavy Ion Collider (RHIC) at Brookhaven National Laboratory in Upton NY, provides the most energetic beams of heavy ions, currently available. The production and study of the QGP is the subject of very intense research by the four experimental collaborations at RHIC [A$^+$05b, A$^+$05a, B$^+$05, A$^+$05f].

An important step in the experimental program has to be the verification that the necessary prerequisites for the creation of a deconfined phase are fulfilled. Estimates of the energy density can be made from the transverse

energy ($E_T$) distributions with a Bjorken ansatz [Bjo83]. Such estimates give energy densities in excess of $5 GeV/fm^3$ for central Au+Au collisions at a center of mass energy per nucleon pair $\sqrt{s_{NN}} = 200 GeV$ [A$^+$05c]. This value is clearly much higher than $\epsilon_C \approx 1 GeV/fm^3$.

An analysis of particle ratios in Au+Au collisions at RHIC with a thermal model that essentially assumes complete chemical equilibration, can describe the data with one common equilibration temperature, as shown in Fig. 1.3 [BMRS03]. The temperature predictions by the model are $T_{chem} \approx 176 MeV$ and $T_{chem} \approx 177 MeV$ for $\sqrt{s_{NN}} = 130 GeV$ (left panel) and $\sqrt{s_{NN}} = 200 GeV$ (right panel), respectively. These values are very close to the critical temperature obtained from lattice QCD calculations [Kar02].
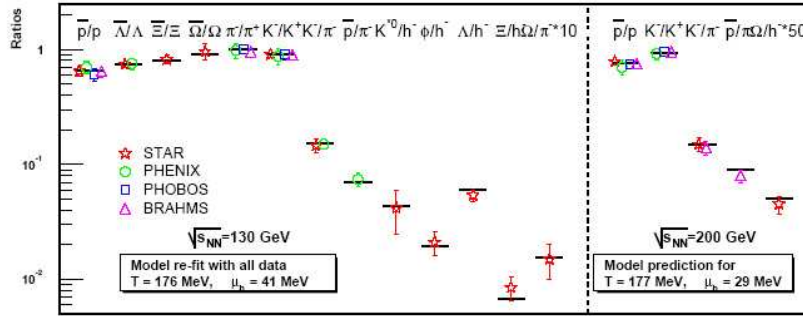


**Figure 1.3:** *Thermal model fits to particle ratios in Au+Au collisions at RHIC. Results for $\sqrt{s_{NN}} = 130 GeV$ are given in the left panel and results for $\sqrt{s_{NN}} = 200 GeV$ are depicted in the right panel. Figure reproduced from Ref. [BMRS03].*

A time-honored method of probing for thermalized matter is the inves-
tigation of various probes with respect to the entrance channel of the reac-
tion [Gho50]. The idea behind such studies is that one can create the same
system via different pathways. If the collision medium was thermalized, the
decay of the matter should not be reflective of how it was formed. A recent
preliminary measurement of the charged particle pseudorapidity density in
Cu+Cu collisions at $\sqrt{s_{NN}} = 200 GeV$ by the PHOBOS collaboration is
identical (within errors) to their earlier measurement of the same quantity
at the same energy and for the same number of participating nucleons in the
collision [R$^+$]. This result suggests that thermalized matter may indeed be
formed in Au+Au and Cu+Cu collisions at top RHIC energy.

A schematic view of a semicentral heavy ion collision in the transverse
plane is given in Fig. 1.4 (a). One notices an approximately elliptical overlap
region, where the short axis of the ellipse is aligned with the azimuth of the
reaction plane of the collision ($\Psi_{RP}$). If the matter is thermalized, pressure
gradients can develop, that predominantly drive particle emission along the
reaction plane (cf. Fig. 1.4 (b)), thereby transforming the initial spatial
anisotropy (Fig. 1.4 (a)) into an effective momentum anisotropy (Fig. 1.4
(c)) [Oll92].

This phenomenon, commonly referred to as "elliptic flow", is sensitive
to the early stages of a heavy ion collision and can give valuable informa-
tion pertaining to issues of thermalization, pressure estimates and possibly
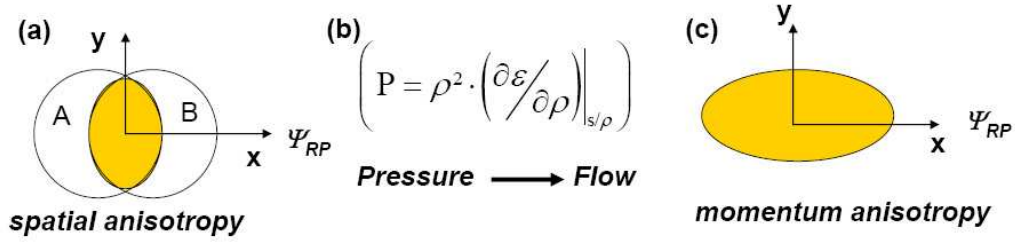
**Figure 1.4:** *Schematic illustration of elliptic flow (see text).*

the equation of state (EOS)[SG86, Oll92]. The azimuthal distribution of particles with respect to the reaction plane can be described via a Fourier decomposition. For symmetry reasons, the odd Fourier coefficients vanish if taken in a symmetric window around midrapidity, and elliptic flow can be identified with the second harmonic Fourier coefficient of this distribution [P+98], generally known as $v_2$ (see Eq. 1.1).

$$\frac{dN}{d(\phi - \Psi_R)} \propto 1 + 2v_2 cos2(\phi - \Psi_R) \tag{1.1}$$

A representative set of elliptic flow results from RHIC can be found in Ref. [Lac05]. Figure 1.5 depicts the azimuthal anisotropy parameter $v_2$ for mesons (pions and kaons) as a function of transverse momentum ($p_T$) and collision centrality for Au+Au collisions at $\sqrt{s_{NN}} = 200 GeV$, as reported in [Lac05]. Very large $v_2$ values are measured, suggesting early thermalization, substantial pressure build up and strongly interacting matter in Au+Au collisions at top RHIC energy.
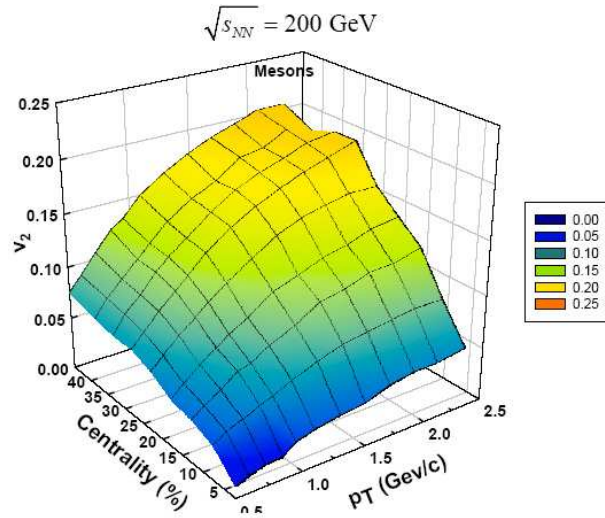
**Figure 1.5:** *Azimuthal anisotropy parameter $v_2$ (see text) for mesons (pions and kaons) as a function of transverse momentum ($p_T$) and collision centrality for Au+Au collisions at $\sqrt{s_{NN}} = 200 GeV$. Figure reproduced from Ref. [Lac05].*

Taken together, the results reviewed in this section suggest that chemically equilibrated, thermalized, strongly interacting matter with energy density in excess of the value required for the creation of a deconfined phase is produced in Au+Au collisions at RHIC.

## 1.2 Jet Modification as a Tomographic Probe of the Medium

In the early phases of a hadronic collision (e.g. $p + p \rightarrow h + X$), two partons from the incoming nucleons can undergo a large momentum transfer ("hard") scattering. The two hard scattered partons will eventually fragment into sprays (or "jets") of hadrons, narrowly focused along the leading parton trajectories. The component of the jet fragment's transverse momentum perpendicular to the parton transverse momentum is usually denoted $j_T$ and appears to be approximately constant with energy for fragments of sufficiently high momentum [A$^+$80]. The parton-parton center of mass system is not identical with the nucleon-nucleon center of mass system and therefore, the two jets can be created with a substantial (pseudo)rapidity gap ($\Delta\eta_{dijet} \approx 1 - 2$) between them. However, the outgoing parton pair will be approximately back-to-back in the transverse plane, barring an intrinsic net transverse momentum $\sqrt{2}k_T$. This $k_T$ smearing is roughly gaussian.

The leading order cross section for the process $p + p \rightarrow h + X$ can be calculated perturbatively in QCD and is given by

$$\frac{d\sigma_{pp}}{dyd^2p_T} = K \sum_{abcd} \int dx_a dx_b f_a(x_a, Q_a^2) f_b(x_b, Q_b^2) \frac{d\sigma}{d\hat{t}}(ab \rightarrow cd) \frac{D_{h/c}}{\pi z_c} \qquad (1.2)$$

Here, $f(x, Q^2)$ denotes the parton distribution function (PDF) for a parton with momentum fraction $x$, $d\sigma/d\hat{t}$ indicates the hard-scattering cross-section

and $D_{h/c}$ is the fragmentation function that gives the probability for a parton of flavor $c$ to fragment into hadrons $h$, carrying a given fraction of the jet momentum $z_c = p_h/p_c$. The process is illustrated schematically in Fig. 1.6. Jet fragmentation has been extensively studied in $e^+ + e^-$ interactions and
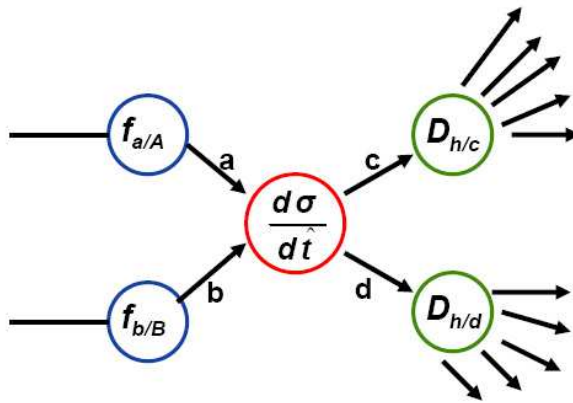


**Figure 1.6:** *Schematic illustration of the process $p + p \rightarrow h + X$ (see text).*

in hadronic collisions (see e.g. [A$^+$00, A$^+$97] and [K$^+$79, A$^+$79a]). Parton distribution functions can be obtained from the proton structure functions, which have been measured in abundance in deep inelastic scattering (DIS) experiments (see e.g. Ref. [TA05]).

In brief, jets in hadronic collisions are rather well understood experimentally and on theoretical grounds.

Since jet fragments strongly cluster in phase-space, jets can be reconstructed statistically via a multi-particle correlation function analysis. Figure 1.7 schematically illustrates the case of (di)jet induced azimuthal two particle correlations (red curve) above an isotropic (flat) underlying event (blue line). Pairs from the same jet produce a narrow peak at $\Delta\phi = 0$. Pairs formed with one particle each from the opposing jets appear at $\Delta\phi = \pi$. The away-side peak is broader than the near-side peak, reflecting the independent fragmentation of both jets and the acoplanarity of the (di)jet in the transverse plane.

In a heavy ion collision, a significant amount of high energy density matter is produced. In 1982, J.D. Bjorken conjectured that a hard scattered parton traversing this matter can lose energy before it fragments into hadrons [Bjo82], effectively "quenching" the yield of high transverse momentum particles from jet fragmentation (cf. Fig. 1.8 (b)). This effect should be observable in the two particle correlation function as a reduction of the away-side peak in Fig. 1.7. The near-side peak is not expected to be significantly affected, since triggering on a high transverse momentum particle is believed to preferentially select unquenched jets from the surface. Another proposed modification to the jet characteristics is acoplanarity broadening due to collisional energy loss [App86, Bla86]. This effect is expected to result in stochastic broadening of the away-side peak in the correlation function.

Jet-modification is believed to be sensitive to several properties of the
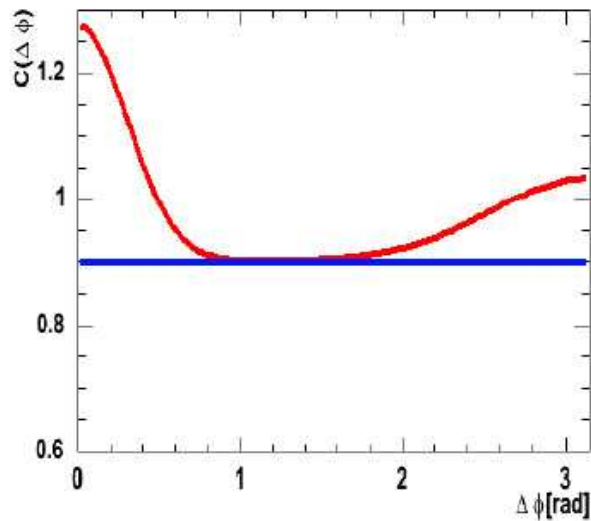
**Figure 1.7:** *Schematic illustration of (di)jet induced $\Delta\phi$ correlations (red curve) above a flat underlying event (blue line). Pairs from the same jet produce a narrow peak at $\Delta\phi = 0$. Pairs formed with one particle each from the opposing jets appear at $\Delta\phi = \pi$. The away-side peak is broader than the near-side peak, reflecting the acoplanarity of the (di)jet in the transverse plane.*

medium, such as the gluon density, it's formation time and the path length traversed [WG92]. The manifestation of jet modifications in the data are specific and can be probed for, therefore enabling jets to be utilized as tomographic short wavelength probes of the high energy density matter created in heavy ion collisions. Several aspects make jets particularly attractive in that regard: (i) Jets are created early and are therefore sensitive to the initial phases of a heavy ion collision. (ii) Jet properties and their modifications can

be calculated in perturbative QCD (see e.g. [BSZ00]). (iii) The jet probe can be calibrated in hadronic (p+p) collisions at RHIC, where vacuum fragmentation is assumed. Cold nuclear matter effects can be measured in d+Au collisions (cf. Fig. 1.8 (a)), allowing to attribute any additional modification in heavy ion collisions to the high energy density medium, created in those collisions (cf. Fig. 1.8 (b)).
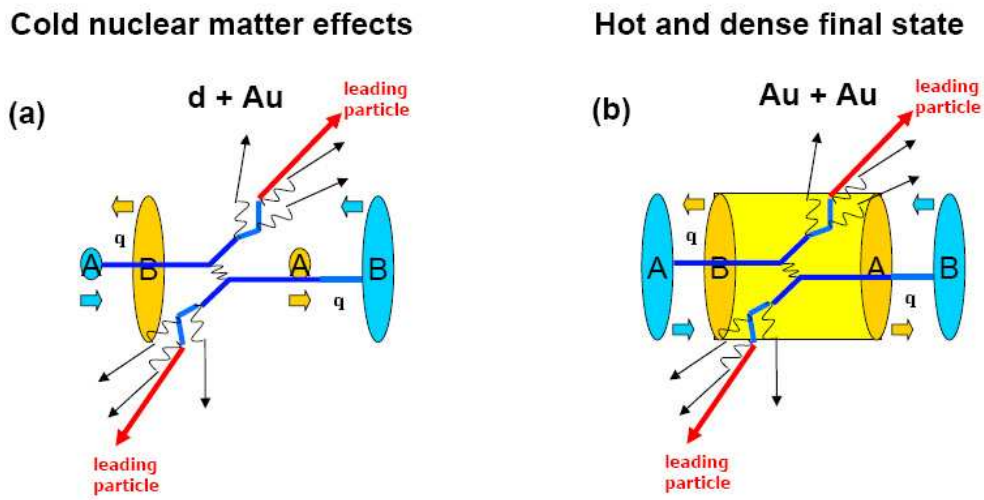


**Figure 1.8:** *Schematic illustration of jet production in d+Au (a) and Au+Au collisions (b) (see text).*

## 1.3    Objectives of this Dissertation

This work attempts a systematic study of jet modification in ultrarelativistic heavy ion collisions at RHIC. To this end, two particle azimuthal correlation functions are utilized to measure jet mediated correlations and harmonic correlations due to elliptic flow in Au+Au and Cu+Cu collisions at $\sqrt{s_{NN}} = 200 GeV$. A novel decomposition technique is applied to extract jet pair distributions with respect to collision centrality, transverse momentum, particle species and colliding system from the heavy ion collisions. These distributions are compared to jet correlation measurements in d+Au collisions at the same energy where no high energy density medium is believed to be created.

The dissertation is organized as follows. Chapter 2 gives an overview of the PHENIX detector and discusses the subsystems relevant for this work in more detail. Chapter 3 presents the correlation function formalism and describes the decomposition techniques utilized to extract jet pair distributions from the correlation function. Following this discussion, chapter 4 details the steps undertaken to obtain robust correlation functions from the data, and chapter 5 explains their decomposition into jet and elliptic flow components. Chapter 6 finally presents the results and discusses the findings. A conclusion and suggestions for further study are presented in chapter 7.

# Chapter 2

# Experimental Setup

The d, Au and Cu beams for this analysis were provided by the Relativistic Heavy Ion Collider (RHIC) at Brookhaven National Laboratory in Upton, New York. RHIC has been designed to collide a variety of species over a wide range of center of mass energies. All measurements presented here are for the center of mass energy per nucleon pair of $\sqrt{s_{NN}} = 200 GeV$. The data were recorded with the PHENIX detector, one of four heavy ion experiments at RHIC. PHENIX is a multipurpose experiment, designed to measure electromagnetic probes of the medium and charged hadrons that emerge from the hot collision zone. To this end, a multitude of subsystems are employed [A$^+$03a]. Two spectrometer arms, each covering 90° in azimuth, are utilized for measurements of electrons, photons and hadrons in the central rapidity region ($-0.35 < \eta < 0.35$). Two other spectrometer

arms at forward and backward rapidities are designed for muon measurements.  Three detectors (Zero-Degree Calorimeters, Beam-Beam Counters and a Multiplicity-Vertex Detector) are placed close to the beam pipe. This set of detectors is used to determine global event information.  The 2004 PHENIX detector configuration is illustrated in Fig 2.1.  The upper panel shows a view along the beam direction and the lower panel shows a side view of the detector.  The PHENIX coordinate system is right-handed and chosen such that the z-axis is oriented along the beam pipe in the direction of the north muon arm. The x-axis points into the west central arm and the y-axis is perpendicular to the other two axes. One Central Magnet and two Muon Magnets with iron yokes and water cooled copper coils generate an axial magnetic field for the central arm and a radial field for the muon arms, respectively.  Since the muon arms are not utilized in this work, only the central arm magnetic field is discussed. This field exhibits a rapid radial fall off from it's maximum value at the center.  This fall off appears approximately gaussian [A$^+$03k].  Figure 2.2 depicts the magnetic field lines as reported in [A$^+$03k].  The field strength varies for different magnet configurations as indicated in Ref. [A$^+$03k]. During the 2002 and 2003 experimental runs, the field strength at the center of the detector was about 0.48T and somewhat larger for later runs.

The PHENIX detector layout is described in detail in Ref. [A$^+$03a].  Here, we only give an overview of the detector subsystems relevant to the presented
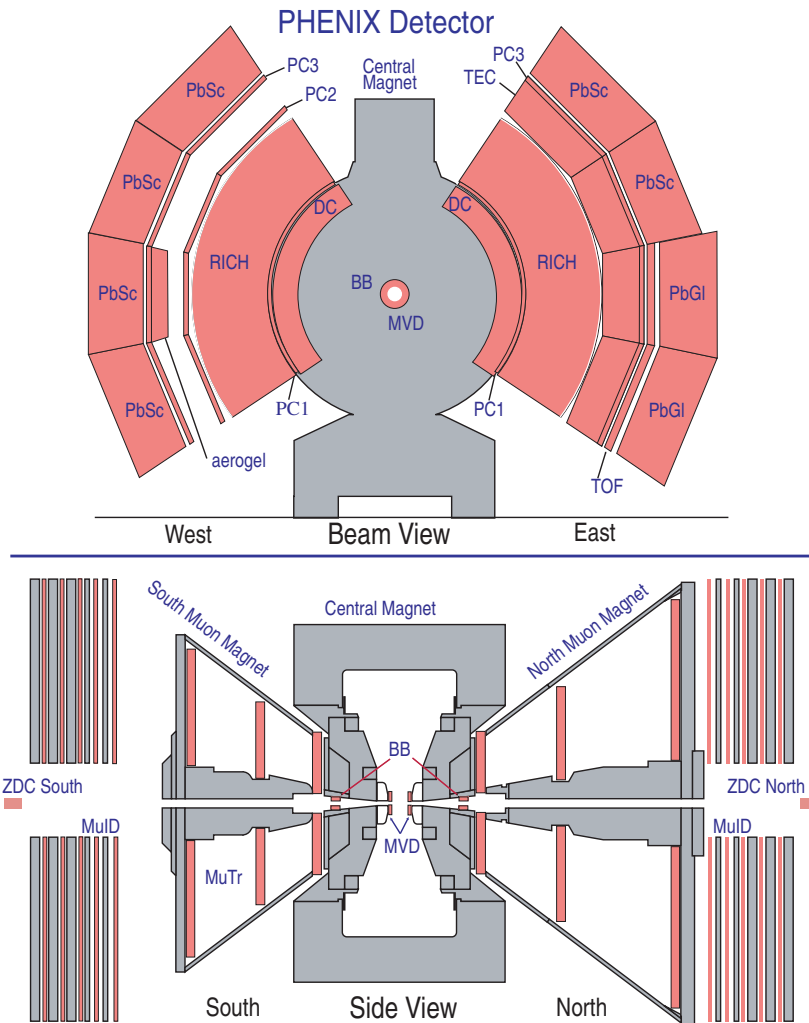
**Figure 2.1:** *PHENIX Run4 detector configuration. A view along the beam pipe (upper panel) and a side view of the detector (lower panel) are depicted.*

analysis.
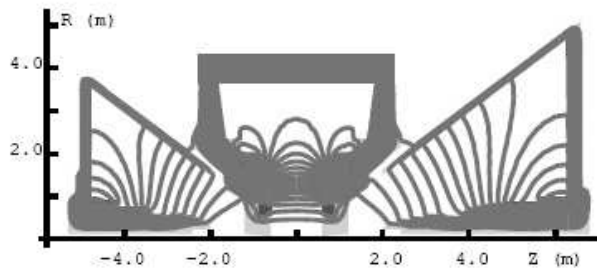
**Figure 2.2:** *Magnetic field lines for the muon and central-arm magnets of PHENIX. The z-axis of the figure coincides with the z-axis of the PHENIX coordinate system (see text). Figure reproduced from Ref. [A+03k].*

## 2.1 Global Detectors

Several detectors determine the necessary global event information. The two Zero-Degree Calorimeters (ZDC) measure spectator neutrons and are used to determine the time and the location of the collision along the beam axis (i.e., the z-vertex). The two Beam-Beam Counters (BBC) also give the collision time and z-vertex. The BBC's have full azimuthal coverage and can be used to construct the azimuth of the reaction plane in each event. In combination, the ZDC/BBC detectors provide information for the minimum bias trigger and are utilized to measure the collision centrality.

## 2.1.1 The Zero-Degree Calorimeters

Two compact hadronic Zero-Degree Calorimeters (ZDC) with tungsten absorber plates [A$^+$03b] are installed close to the beam pipe at a distance of 18 m north and south of the interaction point, placing them at very forward ($|\eta| > 6$) pseudorapidities. Since the ZDC's are located behind the beam dipole magnets, the bending of charged particles away from the ZDC allows for a determination of the deposited energy of spectator neutrons with a resolution of 20%. The ZDC's also provide a coincidence signal for the minimum bias level one trigger and permit for the reconstruction of the z-vertex from the time difference in both detectors. Therefore, they are well suited to monitor luminosity during data taking.

## 2.1.2 The Beam-Beam Counters

The two Beam-Beam Counters, each comprised of 64 Cherenkov telescopes with quartz glass radiators, are positioned along the beam axis at $\pm 1.44$ m relative to the center of the interaction region. They are referred to as BBCN (North) and BBCS (South), respectively [A$^+$03i]. Each BBC array is installed around the beam pipe and thus has full azimuthal coverage. Each covers a pseudorapidity acceptance $|\eta| = 3$ - 3.9.

The BBC's measure the uncorrected arrival time $T_{raw}$ of charged particles from the collision via the average of the hit times. After subtraction of

an offset determined by an iterative minimization of the residual times of all BBC elements, one obtains the corrected arrival time $T_{corr} = T_{raw} - T_{offset}$. This procedure results in a timing resolution of 52 ± 4 ps [A$^+$03i]. The corrected arrival time provides the start time for the time of flight (ToF) measurements with the ToF detector and Electromagnetic Calorimeter (Em-Cal) subsystems.

The z-vertex position of the collision can be obtained from the time difference in both BBC's with a resolution of 6 mm [A$^+$03i]. The collision vertex and the number of hits in the BBC photomultipliers are essential ingredients for the PHENIX minimum bias trigger. The trigger efficiency was evaluated via Monte Carlo simulations and found to be 92 ± 2 % of the inelastic cross section for Au+Au collisions [A$^+$03i] and 88.5 % of the d+Au cross section [A$^+$05d], respectively.

Utilizing a Glauber model Monte Carlo simulation [A$^+$04b], the collision centrality can be inferred from any variable that is a monotonic function of the impact parameter (b), such as total multiplicity, total transverse energy, etc. The BBC charge sum fulfills this requirement and cuts in this distribution are used to determine the centrality in d+Au and Cu+Cu collisions. In Au+Au collisions, the centrality is obtained by making cuts in the space of ZDC versus BBC analog response. Figure 2.3 depicts the two dimensional plot of BBC charge sum versus the energy deposited in the ZDC as reported in [A$^+$03i]. The centroid of the distribution is indicated by the solid green
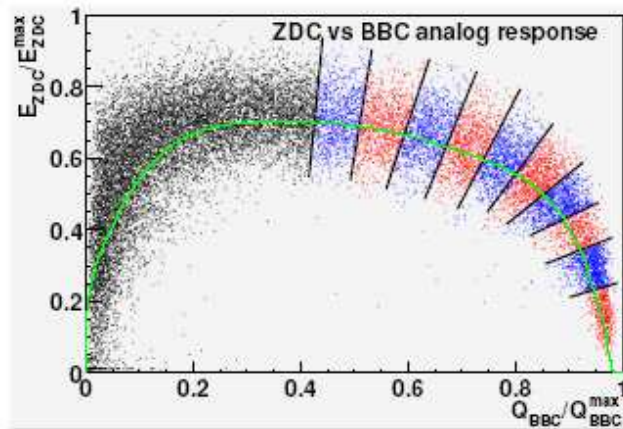
**Figure 2.3:** *BBC charge sum versus the energy deposited in the ZDC. The centroid of the distribution is indicated by the solid green line, and the lines perpendicular to it mark centrality bins in steps of 5 % of the total geometric cross section (Figure taken from [A⁺03i])*

line, and the lines perpendicular to it mark centrality bins in steps of 5 % of the total geometric cross section.

Their full azimuthal coverage makes the BBC's ideally suited to reconstruct the impact parameter direction for flow studies [A⁺03e]. A particularly attractive feature in this regard is the relatively large pseudorapidity gap between the north and south BBC's ($\Delta\eta > 6$) which serves to minimize non-flow contributions to the reaction plane determination [A⁺03e].

## 2.2 Central Arm Detectors

The detector subsystems in the two central arm spectrometers are stacked in layers (see Fig. 2.1). For the analysis presented here, two wire chambers, the Drift Chamber (DC) and the first Pad Chamber plane (PC1) provided the primary charged particle tracking. Tracks were also linked to the third and outermost Pad Chamber plane (PC3) to reject background from conversions, albedo and decays. Electron detection in PHENIX is performed with the Ring Imaging Cherenkov (RICH) detector. For our analysis, we used the RICH to *reject* electron contributions to charged tracks. Particle identification was achieved through time-of-flight measurements with the Time-of-Flight Hodoscope (ToF) and/or the PbSc electromagnetic calorimeter. The ToF wall provides excellent timing resolution but only limited coverage. The PbSc sectors provide hadron identification (albeit with a somewhat poorer timing resolution) for the part of the central arm acceptance not covered by the ToF.

### 2.2.1 The Drift Chamber

Two identical Drift Chamber cylinders with a longitudinal extent of 2 m are located in a residual magnetic field at 2-2.4 m referenced to the beam-axis. The gas volume is filled with a 50%/50% mixture of argon and ethane. The DC contains two groups of wire planes. The first group of twelve wire planes

(X wires) measure trajectories of charged particles in the $r - \phi$ direction with a track finding efficiency of $> 99$ % and a two-track resolution of 2 mm [A$^+$03h]. The second group of eight stereowire planes (U,V wires) provide a measurement of the z-coordinate. Due to the low stereo angle and the small number of wires, this measurement does not give the optimal resolution. To obtain the most accurate measurement of the longitudinal track component, the DC stereo wires, the Pad Chamber and the BBC z-vertex position information are combined (see section 2.2.3). Wire planes in front of the drift chamber reference radius (R=2.2 m) are labeled X1,U1,V1 and those behind the reference radius are denoted X2,U2 and V2.

### 2.2.2 The Pad Chambers

The Pad Chambers are multiwire proportional chambers and are installed outside of the magnetic field region. They consist of a wire plane, enclosed in a gas volume by two cathode walls. One of the cathode planes is substructured into pixels with pad readout, the other consists of an etched copper layer. The cathode panels have a sandwich structure that provides sufficient strength so that little to no additional frame support is needed. This design results in a greatly reduced radiation thickness, keeping the creation of conversion electrons to a minimum. The operating gas for the Pad Chamber (like for the DC) is a 1:1 mixture of argon and ethane.

Three separate Pad Chamber planes, covering a total area of 88 $m^2$, are used to determine three dimensional hit information for charged particle tracks. The first plane (PC1) at radial distance of 2.5 m is mounted to the Drift Chamber. The third Pad Chamber plane (PC3) is located 4.9 m away from the beam pipe between the RICH and EmCal detectors (see Fig 2.1). Track projection from the DC to PC3 plays an important role in background rejection. The PC1 and PC3 planes are present in both arms, while the second plane (PC2) is only installed in the west arm at a radial distance of 4.2 m behind the RICH detector. The PC2 is not used in this analysis. The Pad Chamber layout is depicted in Fig. 2.1.

## 2.2.3 Charged Particle Tracking

Primary charged particle tracking in PHENIX is performed with the Drift Chamber and PC1 subsystems [M$^+$02]. First, a combinatorial Hough transform is used to convert the measured charge points in the X1 and X2 wires in the Drift Chamber into two dimensional tracks in a space defined by the two angles $\phi_{dc}$ and $\alpha$. Here, $\phi_{dc}$ is the azimuthal angle of the track at it's intersection with the DC reference radius R (see section 2.2.1) and $\alpha$ is the inclination angle between the track and a straight line drawn from it's intersection with R to the collision vertex as illustrated in Fig. 2.4. In this space, n hits from the same track produce a spike with amplitude n(n-1)/2. Following this pro-
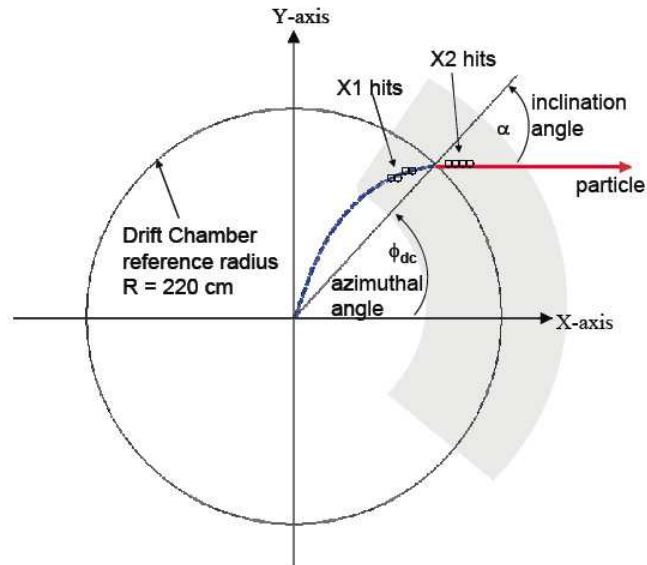
**Figure 2.4:** *Schematic illustration of track reconstruction in the transverse plane of the Drift Chamber (see text). A similar picture can be found in Ref. [M⁺02].*

cedure, PC1 hits that lie within 2 cm of the track in the transverse plane are projected back to the BBC z-vertex to determine the track z-coordinate. The underlying assumption is, that (due to the radial magnetic field in the central arm) tracks will bend very little in the z-direction. This assumption is generally safe, except at the edges of the magnetic field. In this step, occasional ambiguities between multiple PC1 hits are resolved by utilizing the z-coordinate information from the DC stereo wires. The track model assigns a quality variable to the track that reflects it's reconstruction history.

Once three dimensional track information is available, detailed knowledge of the magnetic field allows for the reconstruction of the momentum vector.

Since the central magnetic field is non uniform, a lookup table is used to numerically calculate the field integral and iteratively reconstruct the particle's momentum (p) and azimuthal ($\phi_0$) and polar ($\theta_0$) angle at the vertex. The momentum resolution in Au+Au collisions is $\delta p/p \approx 0.7\% \oplus 1\% p/GeV$.

For the procedure described above, all tracks are assumed to be primary tracks originating at the vertex. A shortcoming of this approach is that low momentum decay daughters can be falsely reconstructed as high momentum tracks. To reject background coming from albedo, conversion electrons and decays, the tracks are projected to the PC3 plane and compared with pad chamber hit information. Tracks that fall outside a specified matching window are rejected.

## 2.2.4   The Ring Imaging Cherenkov Detector

In each central arm, a Ring Imaging Cherenkov (RICH) detector is mounted after the PC1 and used for electron identification. If an electron traverses the $CO_2$ filled RICH volume with a velocity greater than the speed of light in the medium, Cherenkov light is radiated and reflected by two intersecting spherical mirrors onto two detectors with 40 modules of 32 photomultiplier tubes each (cf. Fig. 2.5). With $CO_2$ as operating gas, the heavier pions start to fire the RICH above $p_T \approx 4.65 GeV/c$ and therefore good electron/pion separation is achieved below this value. A more detailed description of the
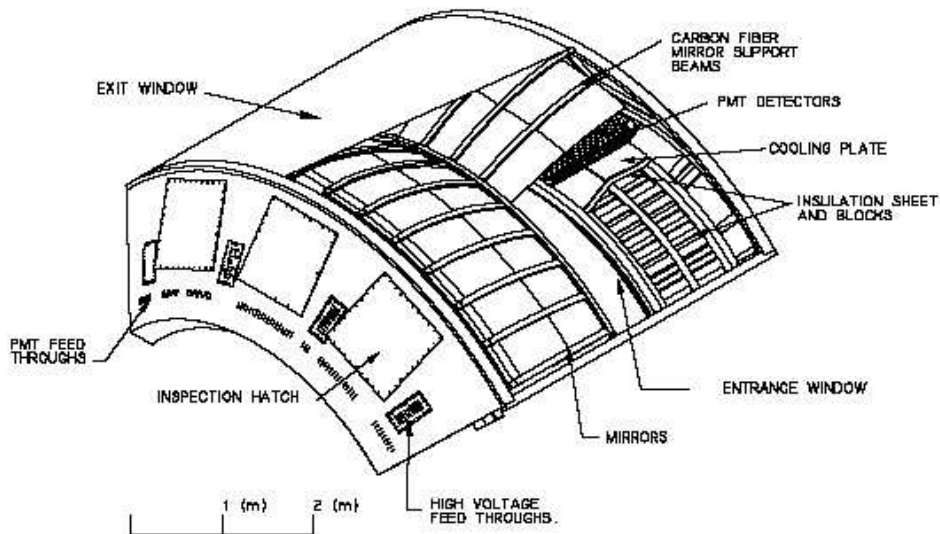
**Figure 2.5:** *Layout of the RICH detector for one of the central arms (see text). Figure reproduced from Ref. [A+03h].*

RICH detector layout and performance can be found in Ref. [A$^+$03h]. In this analysis the RICH detector is only used to reject electron contributions to the charged track sample.

## 2.2.5 The Time-Of-Flight Detector

The Time-of-Flight (ToF) Hodoscope is mounted in the east arm of PHENIX between the PC3 and EmCal detectors. It is comprised of 10 ToF panels, each of which has 96 Bicron BC404 plastic scintillation counters that are read out by a photomultiplier tube at each end. The ToF gives position and time

information. The spatial information is used to match hit positions with the projections from the track model. Particles are identified by correlating their time-of-flight with the momentum measured by the Drift Chamber. With a timing resolution of about 120-130 ps, the ToF wall allows to identify pions and kaons up to a transverse momentum $p_T = 2.4 GeV/c$ and can be used to separate protons from mesons up to $p_T = 4 GeV/c$. A detailed design report and further information on the ToF subsystem is given in Ref. [A$^+$03h].

## 2.2.6 The Electromagnetic Calorimeter

The Electromagnetic Calorimeter (EmCal) consists of two subsystems. Six sectors of lead-scintillator (PbSc) detectors and two sectors of lead-glass (PbGl) detectors cover the full central arm acceptance of PHENIX. Both set of detectors have been designed to measure electrons and photons with excellent timing and good position and energy resolution. They also provide a very good measurement of the hadronic energy. The hadronic response of the PbSc detector is well understood. The hadronic response of the PbGl is not. For this reason, and also because of the better timing resolution, the PbSc is the calorimeter of choice for hadron identification in this work. The design and performance of the EmCal is reported in Ref. [A$^+$03j]. In what follows, we will therefore only focus on the most important features of the PbSc detector. The PbSc is a sampling calorimeter made of a large number

of "towers". A total of 66 sampling scintillator cells and lead tiles are combined in an alternating pattern to form such a tower. Light is collected via wavelength shifting fibers that are directly connected to the cells and read out by a phototube. An illustration of a typical PbSc module layout is given in Fig. 2.6 (Fig. taken from Ref. [A+03j]). Four towers form a module and 36 modules form a supermodule. Each sector consists of 18 supermodules. Electromagnetic and hadronic particles deposit energy differently in a mod-
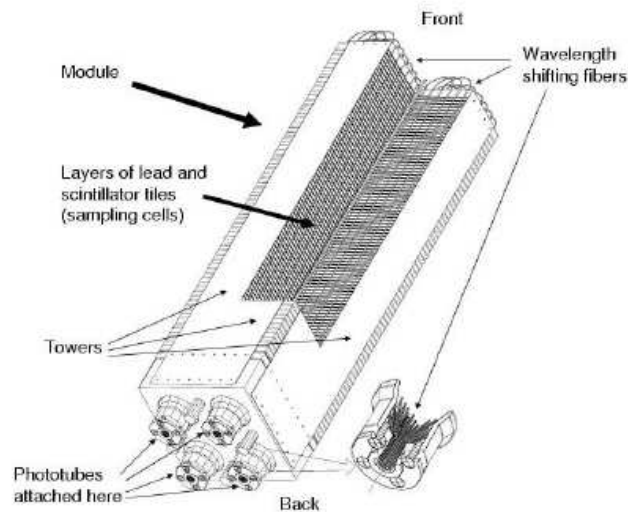


**Figure 2.6:** *Layout of a PbSc module. Figure reproduced from Ref. [A+03j]*

ule and the shower shape can be used to distinguish between them [A+03j]. In addition, towers can be linked with track projections to facilitate hadron identification. The timing resolution for hadrons after calibration is of the

order of 400 ps, resulting in proton identification up to $p_T = 2.5 GeV/c$ and pion to kaon separation up to $p_T = 1.2 GeV/c$. This is illustrated by Fig. 2.7 which depicts the correlation between time-of-flight and charge times inverse momentum for the East2 sector in d+Au collisions. Although the timing
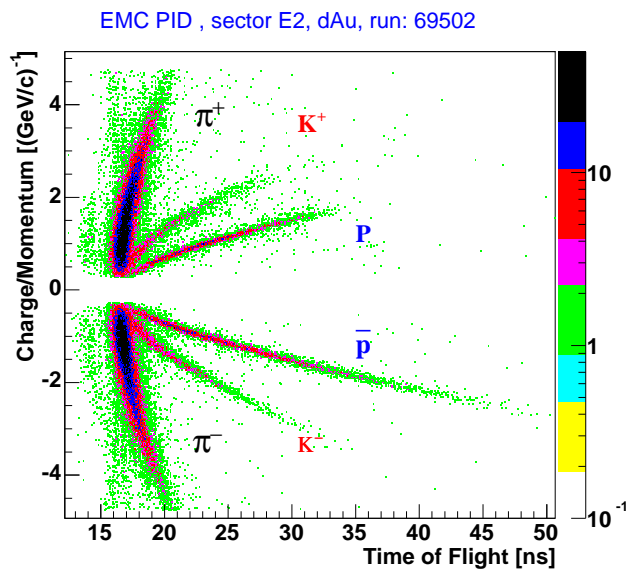
**Figure 2.7:** *Correlation between time-of-flight and charge times inverse momentum for the East2 EmCal sector in d+Au collisions. Figure courtesy A. Taranenko.*

resolution of the PbSc is not nearly as good as that for the ToF wall, it has a much larger acceptance. In fact, as can be seen from Fig. 2.1, the ToF is actually mounted directly in front of the PbGl sectors, so that the combination of PbSc calorimeters and ToF detector provide continuous hadron identification coverage for the central arms of PHENIX. This is certainly a desirable feature for correlation studies described in the ensuing chapters.

# Chapter 3

# The Correlation Function Method

Azimuthal correlation measurements between two or more particles provide an important probe for the properties and the decay-dynamics of the hot and dense matter created in ultrarelativistic heavy ion collisions and have a long historical standing in the field [W$^+$91, L$^+$93]. At RHIC energies, they allow for the simultaneous and systematic study of elliptic flow and (di)jet modification. The former can give invaluable insights on reaction dynamics and the equation of state [T$^+$01, K$^+$01, HKH$^+$01, H$^+$04]. The latter affords tomographic information about the high energy density matter [Bjo82, App86, Bla86]. Here, we define the azimuthal correlation function and discuss the methodologies used to decompose it into it's respective harmonic (or flow) and (di)jet components.

## 3.1 The Two Particle Azimuthal Correlation Function

The correlation function in relative azimuthal angle between two particles ($\Delta\phi = (\phi_1 - \phi_2)$), is generated as the ratio of a foreground distribution $N_{cor}$, which is constructed from coincident particle pairs within the same event, to a background distribution $N_{mix}$, generated by randomly pairing particles from different events within the same centrality and vertex classes;

$$C\left(\Delta\phi\right) \propto \frac{N_{cor}\left(\Delta\phi\right)}{N_{mix}\left(\Delta\phi\right)}. \tag{3.1}$$

If both particles come from the same $p_T$ selection, one speaks of "fixed $p_T$ correlations". The case of each particle from a different $p_T$ bin is designated "assorted $p_T$ correlations". In the latter case, the particle with higher transverse momentum will be called the "trigger" particle, and the lower $p_T$ partner the "associated" particle. This distinction, although customary, is somewhat arbitrary.

The foreground distribution contains the physics correlations which can be obscured by experimental efficiency/acceptance effects. Any physics correlation will be absent when two particles from unrelated events are selected to form a pair. The background distribution is therefore a measure of the experimental pair acceptance/efficiency in $\Delta\phi$. The operational assumption behind a correlation function analysis is that the pair acceptance/efficiency

effects cancel when the ratio of foreground to background distribution is formed. The correlation function then reveals the true correlation shape, free of the blurring acceptance/efficiency effects. This is demonstrated below.

The probability distributions (integrated over the detector pseudorapidity or $\eta$ acceptance) for measuring single particles $p(\phi)$ and particle pairs $p(\phi_1, \phi_2)$ can be expressed as

$$p(\phi) = A(\phi) \frac{dN}{d\phi} \tag{3.2}$$

$$p(\phi_1, \phi_2) = A(\phi_1, \phi_2) \frac{d^2N}{d\phi_1 d\phi_2} \tag{3.3}$$

where $A(\phi)$ and $A(\phi_1, \phi_2)$ are the acceptance/efficiency functions for single particles and particle pairs, respectively. $A(\phi_1, \phi_2)$ is commonly very well approximated by the product of single particle acceptance/efficiency functions $A(\phi_1, \phi_2) = A(\phi_1) \times A(\phi_2)$. The azimuthal distribution of particle pairs before detection is denoted $d^2N/d\phi_1 d\phi_2$ and only contains physics correlations between the two particles. Similarly, the single particle distribution before detection is given by $dN/d\phi$ and is a constant. Using Eqs. 3.2 and 3.3 we can rewrite the correlation function

$$C(\Delta\phi) \quad \propto \quad \frac{\int \frac{d\phi_1}{2\pi} p(\phi_1) p(\phi_1 - \Delta\phi)}{\int \frac{d\phi_1}{2\pi} p(\phi_1) \int \frac{d\phi_2}{2\pi} p(\phi_2)} \tag{3.4}$$

$$\propto \quad \frac{A(\phi_1, \phi_2)}{A(\phi_1) A(\phi_2)} \frac{dN}{d\Delta\phi} \propto \frac{dN}{d\Delta\phi} \tag{3.5}$$

As can be seen from Eq. 3.5, azimuthal acceptance and detector efficiencies

cancel in the ratio of foreground to background distribution and $C(\Delta\phi)$ is related to the efficiency corrected distribution of azimuthal pair separations $dN/d\Delta\phi$ only by a constant. The area normalized correlation function

$$C\left(\Delta\phi\right) = \frac{N_{cor}\left(\Delta\phi\right)}{N_{mix}\left(\Delta\phi\right)} \frac{\int d\Delta\phi N_{mix}(\Delta\phi)}{\int d\Delta\phi N_{cor}(\Delta\phi)} \tag{3.6}$$

can thus be interpreted as the efficiency corrected probability distribution for correlated particle pairs within the detector pseudorapidity acceptance.

## 3.2 The Two-Source Model

In p+p and d+Au collisions at RHIC, the two particle correlation function is well described by attributing all correlation to (di)jets and assuming an uncorrelated (i.e. isotropic) underlying event [Rak04].

$$C(\Delta\phi) = a_\circ + J(\Delta\phi) \tag{3.7}$$

In Eq. 3.7 $J(\Delta\phi)$ is the component of the correlation function that is due to (di)jet correlations, hereafter referred to as jet-function, and $a_\circ$ denotes the background level of the underlying event.

By contrast, in heavy ion collisions at RHIC, pressure gradients can build up, that can give rise to elliptic flow which drives particle emission preferentially toward the reaction plane [Oll92]. On an event by event basis the elliptic flow induced single particle distribution relative to the reaction plane

($\Psi_R$) is given by a second order harmonic function [P$^+$98]

$$\frac{dN}{d(\phi - \Psi_R)} = A\left(1 + 2v_2 cos2(\phi - \Psi_R)\right) \tag{3.8}$$

with amplitude $v_2$. From Eq. 3.8 it follows that the underlying event in heavy ion collisions need not be isotropic.

Indeed, the two-particle correlation function in Au+Au collisions at RHIC can be fully described by only *two sources* of azimuthal correlations: (di)jet correlations $J(\Delta\phi)$ and a harmonically modulated underlying event, due to elliptic flow $H(\Delta\phi)$ [A$^+$03c, Aji03, Chi03, A$^+$03d].

It can be shown [Sta05], that in the presence of flow Eq. 3.7 becomes

$$C(\Delta\phi) = a_\circ H(\Delta\phi) + J(\Delta\phi), \tag{3.9}$$

where $H(\Delta\phi)$ is a second order harmonic function, whose amplitude is given by the product of the anisotropy amplitudes of the distribution of "trigger" and "associated" particles relative to the reaction plane (cf. Eq. 3.8), i.e. $v_{2,trig}$ and $v_{2,assoc}$, respectively.

$$H(\Delta\phi) = [1 + 2(v_{2,trig} \times v_{2,assoc})cos2(\Delta\phi)] \tag{3.10}$$

# 3.3 Decomposition of the Correlation Function

It follows from the above discussion that a thorough investigation of possible modifications to the (di)jet pair distribution in Au+Au collisions requires the separation of the jet-signal from the underlying harmonic "background". Reliable procedures for such a decomposition are detailed in Refs. [Sta05, A+05e]. Consequently, only the main steps of the procedure are outlined below.

## 3.3.1 The ZYAM Subtraction Technique

Through rearranging Eq. 3.9 we see that $J(\Delta\phi)$ can be extracted by building the difference between the correlation function $C(\Delta\phi)$ and the harmonic component $a_\circ H(\Delta\phi)$.

$$J(\Delta\phi) = C(\Delta\phi) - a_\circ H(\Delta\phi). \tag{3.11}$$

This requires robust knowledge of both the normalization ($a_\circ$) and the strength of the harmonic amplitude ($v_2$). The value of $a_\circ$ can be fixed by requiring that the value of the jet-function is zero at the minimum $\Delta\phi_{min}$ [A+05e],

$$J(\Delta\phi_{min}) = 0. \tag{3.12}$$

This approach has been referred to as the "Zero Yield At Minimum" or ZYAM approach [A+05e] and it's particular strength is that no functional

form for J($\Delta\phi$) need to be assumed. A robust practical implementation [A$^+$05e] determines the minimum by changing $a_\circ$ until the harmonic background touches a functional fit to the correlation function $a_0 H(\Delta\phi_{min}) = C(\Delta\phi_{min})$. This method minimizes effects related to statistical fluctuations of the data points. The systematic error on $a_\circ$ associated with the fitting procedure can be estimated by considering a variety of functional forms that each give a good representation of the data.

It is straightforward, to extract the harmonic amplitude ($v_2$) from the azimuthal single particle distribution with respect to the reaction plane $\Psi_R$ (Eq. 3.8) [P$^+$98]. The reaction plane can be reconstructed and corrected for dispersion following the procedures outlined in Ref. [P$^+$98]. For a reliable $v_2$ measurement it is important that the reaction plane itself is reconstructed free of non-flow biases. In PHENIX, the relatively large pseudorapidity gap between the north and south BBC's ($\Delta\eta > 6$) serves to significantly reduce such non-flow contributions to the reaction plane determination [A$^+$03e]. Further minimization of non-flow biases to the measured $v_2$ is achieved by demanding a large pseudorapidity gap between the reaction plane and the particles correlated with it ($\Delta\eta_{(\phi-\Psi_R)} > 3$) [A$^+$03e]. The $v_2$ so extracted is a weighted average of the azimuthal anisotropies of both sources and varies with transverse momentum ($p_T$) and centrality [A$^+$03e]. To avoid potential $v_2$-biases it is important to determine $v_2$ from the same dataset that is used for the generation of the correlation function.

The reliability of the ZYAM decomposition technique was tested exten-
sively with detailed Monte Carlo simulations in Ref. [A$^+$05e]. These investi-
gations took the limited PHENIX aperture into account and were performed
for a variety of input jet-functions. A typical set of results from these
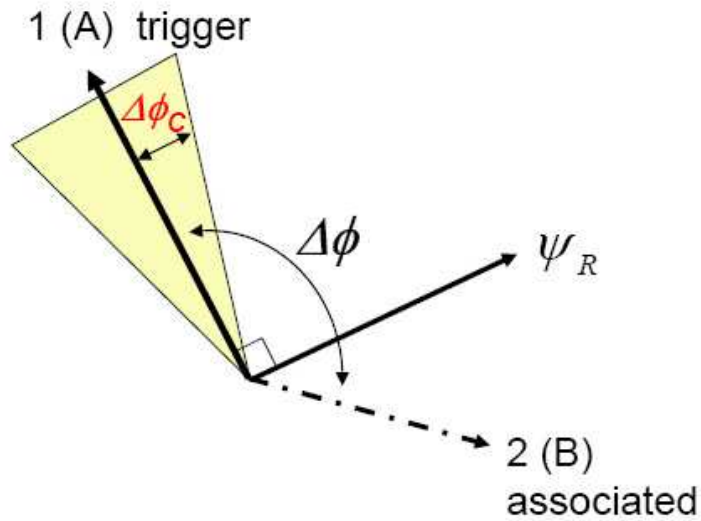


**Figure 3.1:** *Schematic illustration for out-of-plane correlations (see text). The
trigger particle (A) is selected in a constraint window $\Delta\phi_C$ perpendicular to the
reaction plane $\Psi_R$ and correlated with associated partner particles (B).*

simulation studies is given in Fig. 3.2. The azimuthal correlation function
(filled circles in panel (b)) was generated from simulated data that was passed
through a PHENIX $\phi$ and $\eta$ acceptance filter. The amplitude (cf. Eq. 3.10)
of the harmonic component H($\Delta\phi$) (dashed line) in panel (b) was determined
from a fit with Eq. 3.8 to the azimuthal distribution of simulated particles

with respect to the event plane (panel (a)). The extracted jet-function J($\Delta\phi$) was then obtained by subtracting H($\Delta\phi$) from the correlation function following Eq. 3.9 and the ZYAM prescription. J($\Delta\phi$) is shown in panel (b) as filled squares. The solid line depicts the input jet-function, as determined by tagging the jet particles in the simulation. There is overall excellent agreement between the extracted jet-function and the input jet-function in Fig. 3.2, showing that robust retrieval of J($\Delta\phi$) is achieved.

The method can also be applied to cases for which the trigger particle is constrained relative to the reaction plane. In this case, the harmonic amplitude of H($\Delta\phi$) is given by the product of $v_2$ for the constrained trigger particle and the $v_2$ of the unconstrained associated particle ($(v_2^t)^c \times v_2$). It has been shown in Refs. [BEF$^+$04, BO04] that the anisotropy parameter for the constrained trigger particle $(v_2^t)^c$ depends on the width (or "bite") of the angular constraint $\Delta\phi_c$, it's orientation relative to the reaction plane $\phi_c$, and the event plane resolution $\Delta\Psi_R$ (cf. Fig. 3.1). For the specific case, where the constraint window is selected perpendicular or parallel to the reaction plane, the $v_2^t$ values out-of-plane and in-plane ($(v_2^t)^{out}$ and $(v_2^t)^{in}$, respectively) are given by Eqs. 3.13 and 3.14, respectively [BEF$^+$04].
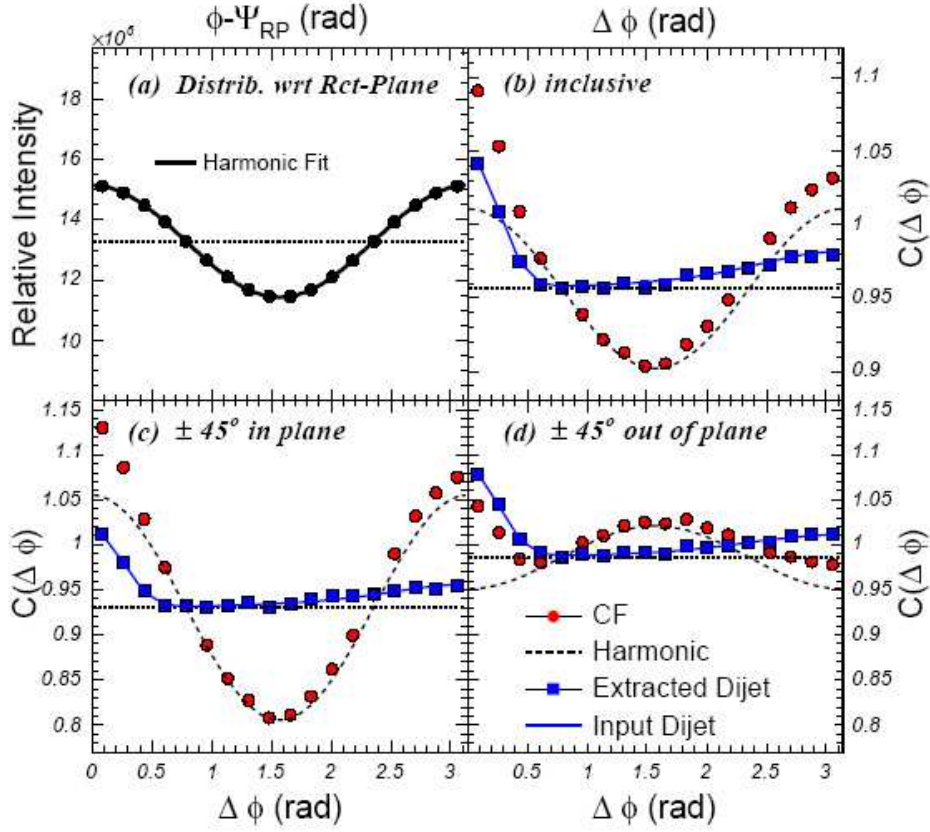
**Figure 3.2:** *ZYAM decomposition of Monte Carlo simulated correlation functions (see text). Panel (a) shows the azimuthal distribution of simulated particles relative to the reaction plane. Panel (b) depicts a simulated inclusive correlation function (red cricles), with harmonic component (dashed line) and input jet pair distribution (solid blue line) referenced to the background level $a_o$ (dash-dotted line). The ZYAM subtracted jet pair distribution is shown as blue squares. Good overall agreement is observed between extracted and input jet pair distributions. Panel (c) and (d) are the same as (b) but for trigger particle selections parallel and perpendicular to the reaction plane. Figure reproduced from Ref. [A[+]05e].*

$$(v_2^t)^{out} = \left( \frac{2v_2^t\left(\Delta\phi_c\right) - \sin\left(2\Delta\phi_c\right)\left\langle\cos\left(2\Delta\Psi_R\right)\right\rangle}{2\left(\Delta\phi_c\right) - 2v_2^t\sin\left(2\Delta\phi_c\right)\left\langle\cos\left(2\Delta\Psi_R\right)\right\rangle} \right)$$

$$+ \left( \frac{\frac{v_2^t}{2}\sin\left(4\Delta\phi_c\right)\left\langle\cos\left(4\Delta\Psi_R\right)\right\rangle}{2\left(\Delta\phi_c\right) - 2v_2^t\sin\left(2\Delta\phi_c\right)\left\langle\cos\left(2\Delta\Psi_R\right)\right\rangle} \right) \quad (3.13)$$

$$(v_2^t)^{in} = \left( \frac{2v_2^t\left(\Delta\phi_c\right) + \sin\left(2\Delta\phi_c\right)\left\langle\cos\left(2\Delta\Psi_R\right)\right\rangle}{2\left(\Delta\phi_c\right) + 2v_2^t\sin\left(2\Delta\phi_c\right)\left\langle\cos\left(2\Delta\Psi_R\right)\right\rangle} \right)$$

$$+ \left( \frac{\frac{v_2^t}{2}\sin\left(4\Delta\phi_c\right)\left\langle\cos\left(4\Delta\Psi_R\right)\right\rangle}{2\left(\Delta\phi_c\right) + 2v_2^t\sin\left(2\Delta\phi_c\right)\left\langle\cos\left(2\Delta\Psi_R\right)\right\rangle} \right) \quad (3.14)$$

Results from simulations in which such constraints have been applied are summarized in panels (c) and (d) of Fig.3.2 for trigger particles within a 90° window in-plane and out-of-plane, respectively. The input jet-function is reliably extracted in these cases, as well.

### 3.3.2   The Harmonic Extinction Technique

The difficulties in the decomposition of the two particle correlation function in heavy ion reactions (as compared to d+Au or p+p collisions) stem from the harmonic modulation of the underlying event in these collisions. This is indicated by Eq. 3.9. If one had a technique to reduce Eq. 3.9 to Eq. 3.7, all correlation strength in the correlation function could be directly attributed to jets. Such a technique has been developed in Ref. [A+05e].

This technique utilizes azimuthal correlation functions in which the trigger particles are selected in a window perpendicular to the reaction plane, *ie.* out-of-plane correlations. For these distributions, the harmonic amplitude of

the trigger particle, $v_2^t$, is given by Eq. 3.13 [BEF$^+$04]. Upon careful examination of this equation one can see, that $(v_2^t)^{out}$ can change phase from negative to positive values as the reaction plane resolution $\Delta\Psi_R$ and/or the constraint bite $\Delta\phi_c$ are broadened. This implies, that under certain conditions, $(v_2^t)^{out}$ can be set to zero (which is equivalent to setting $H(\Delta\phi) = 1$). Usually, the reaction plane resolution is dictated by the experimental constraints, but $\Delta\phi_c$ can be selected so that the harmonic correlations are extinguished [A$^+$05e].

Fig. 3.3 shows an example of the harmonic extinction method [A$^+$05e]. Two simulated correlation functions for pure harmonic correlations with an input $v_2 \sim 0.16$ are depicted. The circles indicate the unconstrained correlation function which exhibits sizable anisotropy. The squares represent the correlation function where the trigger particle is selected in a window perpendicular to the reaction plane. The width of this window $\Delta\phi_c$ has been adjusted, so that $(v_2^t)^{out} = 0$ [A$^+$05e]. This out-of-plane correlation function is flat and does not show any correlations as expected if the harmonic term has been reliably extinguished. A particular asset of this technique is that the correlation function directly reveals the correlation shape for the jet function, i.e. $C(\Delta\phi) = a_\circ + J(\Delta\phi)$, without the obscuring effect of the harmonic correlations.
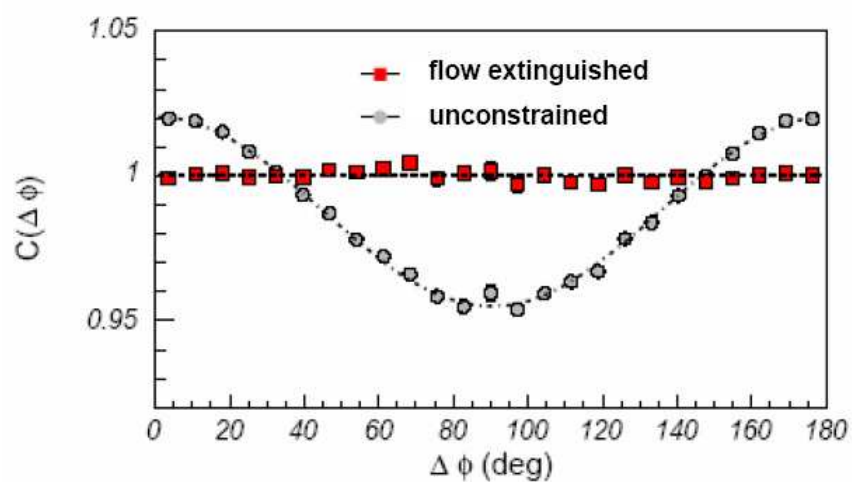
**Figure 3.3:** *Simulated correlation functions for pure harmonic correlations. The circles indicate the unconstrained correlation function. The squares represent the out-of-plane correlation function where the trigger particle is selected in a window perpendicular to the reaction plane. The width of this window $\Delta\phi_c$ has been adjusted, so that $v_{2,trig} = 0$. Data from [A+05e].*

## 3.4 Extracting Yields from Correlation Functions

In addition to the study of jet-topologies, it is often desirable to extract yield information from the correlation function as well. In sections 3.3.1 and 3.3.2 we have introduced techniques to obtain the jet-pair distribution J($\Delta\phi$) from the correlation function. The integral of this distribution can be related to the fraction of jet-correlated particle pairs (PF) [Sta05, A$^+$05e]. This is done, by summing $J(\Delta\phi)$ and $C(\Delta\phi)$ over all bins in $\Delta\phi$ and forming the ratio of these two sums, respectively,

$$PF = \frac{\sum_i J(\Delta\phi_i)}{\sum_i C(\Delta\phi_i)}.$$ (3.15)

The jet pair fraction is the central quantity from which we calculate all other desired yield information.

Historically, jet correlation studies were assorted $p_T$ studies and it was found advantageous to express jet induced yields obtained from these measurements as conditional yields [A$^+$79a]. The conditional yield (CY) is defined as the ratio of jet-correlated pairs per trigger particle.

$$CY = \frac{N_{pairs}^{jet}}{N_{trig}^{all}}$$ (3.16)

One immediately recognizes Baye's theorem at work, here. Given that one finds a trigger particle, the CY gives the probability for finding a jet-associated

partner particle. The interpretation of the conditional yield is thus straight-forward in experiments where all trigger particles can be attributed to jets (such as in $e^+ + e^-$ collisions). In the two source model, the trigger particles can be an admixture of jet particles and background particles. Therefore, some care needs to be taken when interpreting conditional yield information in heavy ion collisions.

One can calculate the efficiency corrected conditional yield from the pair fraction as follows. First one multiplies PF by the ratio of the average number of detected particle pairs per event $\langle N_d^{pair} \rangle$, to the product of the detected singles rates $\langle N_d^{trig} \rangle$, $\langle N_d^{assoc} \rangle$. This gives the jet pair production over and above the uncorrelated background. The assumption that enters here, is that the pair efficiency can be well approximated by the product of single particle efficiencies. Multiplying this efficiency corrected quantity with the efficiency corrected singles rate, $\langle N_{eff}^{assoc} \rangle$, for the associated $p_T$ bin, gives the efficiency corrected conditional yield [Sta05, A$^+$05e].

$$CY = PF \times \frac{\langle N_d^{pair} \rangle}{\langle N_d^{trig} \rangle \times \langle N_d^{assoc} \rangle} \times \langle N_{eff}^{assoc} \rangle. \qquad (3.17)$$

The average number of efficiency corrected jet pairs per event is obtained from the conditional yield by multiplication with the efficiency corrected number of trigger particles per event

$$\langle N_{jet,eff}^{pair} \rangle = CY \times \langle N_{eff}^{trig} \rangle. \qquad (3.18)$$

# Chapter 4

# Data Reduction and Analysis

The results in this thesis were obtained from data that were recorded during the second, third, fourth and fifth running period of PHENIX. These periods are designated by the labels Run2, Run3, Run4 and Run5, respectively, and often included several collision species and beam energies. In this dissertation, results are shown for Run2 Au+Au collisions, Run3 d+Au collisions, Run4 Au+Au collisions and Run5 Cu+Cu collisions (all at $\sqrt{s_{NN}} = 200 GeV$). The main focus of this chapter is to report on the steps undertaken to obtain robust correlation functions from all four datasets. These procedures include detailed quality assurance (QA) studies which specifically contain a technique to address time-dependent efficiency fluctuations within the data. Single particle and particle pair cut evaluations are described, and extensive tests of the efficacy and reliability of the correlation functions are reported.

It should be noted, that the four independent datasets were analyzed (and portions of the results published) at quite different times. While the basic analysis strategies are similar, the following sections reflect the different analysis requirements of these datasets as well as chronological improvements in methodology. Here it bears mentioning, that a lot of data handling procedures (such as the matching to outer detectors, ToF and EmCal timing calibrations, etc.) have been developed over time by many different people in PHENIX. These procedures have for the most part been standardized and are widely used throughout the collaboration.

## 4.1 Run, Event and Track Selections

A period of consecutive data taking is called a run [1] and assigned a unique number. For ease of use, data pertaining to runs are often broken up into smaller groups, called segments. Each segment holds the tracks and global information of approximately 10000 collisions (events). First, bad runs are rejected based on run-by-run quality assurance. Tracks from collisions which have passed a set of event selection criteria are then examined further. Correlation functions are only constructed from the collection of "good tracks".

---

[1] The term run is somewhat ambiguous, since it is used both for the overall experimental running period as well as for consecutive periods of data taking during this period. Here, the term run will generally refer to the latter case and the experimental running periods will be explicitly called Run2-Run5

### 4.1.1 Run Selection

After using standard PHENIX Quality Assurance (QA) and run-database information to reject "bad runs", an additional set of run-by-run QA studies was performed. For this purpose, the run dependence of several quality-check variables was examined. Runs that showed any significant variation in these variables were assumed to be pathological and excluded from further analysis. Variables under study include the mean and width of the BBC vertex distribution, the average centrality per run, the mean transverse momentum of particles as reconstructed by the track model, a test for variations in drift chamber efficiency via the ratio of west-arm to east-arm multiplicities, the mean of the PC3 track matching distributions (*before* calibration) and the mean and width of the PbSc timing distributions.

As an example, Fig. 4.1 shows the run dependence for a subset of these quality variables for the Run4 Au+Au data set. They are very stable with run number. The few outliers were excluded from the analysis. A similarly careful run-by-run QA was performed for all four datasets.

### 4.1.2 Event and Track Selection

Event selection was relatively simple, and after assuring that only good collisions were accepted, several track quality variables were inspected to reject bad tracks.
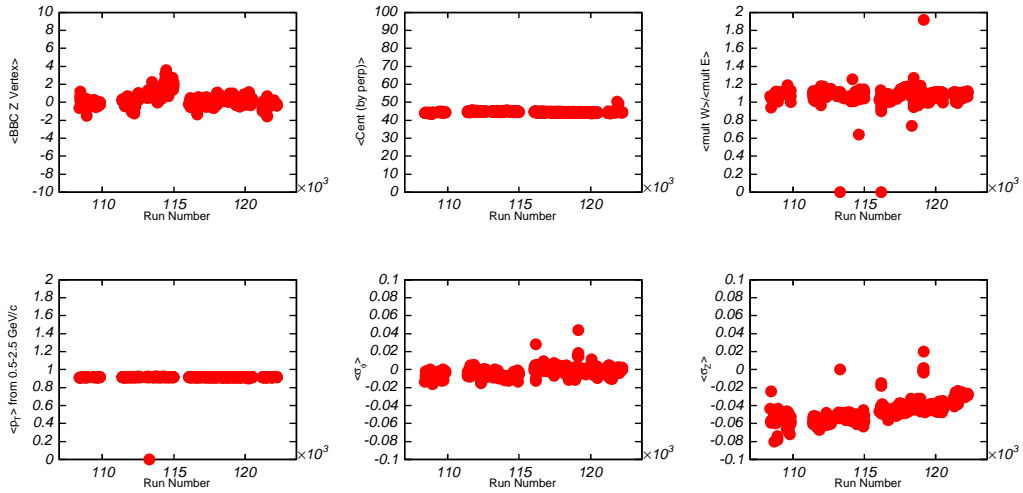
**Figure 4.1:** *Run dependence of quality-check variables for Run4 Au+Au collisions. Variables from top left to bottom right are the mean of the BBC vertex distribution, the average centrality per run, the ratio of west-arm to east-arm multiplicities, the mean transverse momentum of particles as reconstructed by the track model, the mean of the centrality distribution and the mean of the PC3 track matching distributions in azimuth and zed (before calibration, see text). Overall the Run4 data set was very stable. Outliers were removed from the analysis.*

**Event Selection**

Events were required to have fired the Local LVL1 Minimum Bias trigger and have their z-vertex (as determined by the BBC) within a ± 30 cm range.

**Track Selection**

Several selection criteria are common to all the presented analyses. Only high quality tracks from the track model were used. These tracks either have their z-coordinate uniquely determined by the PC1 hit information (quality variable = 63 following PHENIX convention), or in case of ambiguity, by the DC stereowires (quality variable = 31 following PHENIX convention). All tracks were required to have a minimum transverse momentum of $p_{T,min} = 0.3 GeV/c$. To remove edge effects in the Drift Chamber, all tracks were subjected to a fiducial cut on the z-coordinate from the track model of $\mid z \mid$ <75 cm and the polar angle at the vertex $\mid \theta_0 - \frac{1}{2}\pi \mid$ <0.34. Electrons were rejected by excluding tracks from the analysis that have fired one or more phototubes in the RICH detector.

The single particle cut that varied for the different analyses is the matching condition applied to the relationship between the track-model projections and the measured PC3 hits. These cuts were made in terms of the standard deviation in the distribution of $\Delta z$ and $\Delta \phi$ matching residuals, i.e $\sigma_z$ and $\sigma_\phi$, respectively. Either box cuts ($\sigma_z < x$ and $\sigma_\phi < y$) or radial cuts

($\sqrt{\sigma_z^2 + \sigma_\phi^2} < z$) were applied, as necessary.

Initial matching to the outer detectors was not optimized for the d+Au dataset. Consequently, a correction factor was applied to $\sigma_z$ and $\sigma_\phi$. The distributions of matching residuals can show very different trends with $p_T$ and centrality, depending on the charge and z-position of the tracks [Jia03]. Therefore, it was important to correct the matching for positive and negative tracks in the north and south sides of each arm separately. This procedure is outlined, below.

A fit with a gaussian plus offset to the $\sigma_Z$ and $\sigma_\phi$ distributions gave centroids and widths. Figure 4.2 shows the $p_T$ dependence of these values obtained from the $\sigma_\phi$ distributions in 0-20% most central collisions. The upper left panel of Fig. 4.2 depicts the gaussian means for the east arm and the upper right panel shows the corresponding widths. The red data points represent results for positively charged tracks, and the blue data points are results for negatively charged tracks. Open and filled circles denote data for the north and south side of the east arm, respectively. The lower left and right panels show the identical results to the upper left and right panels, but for the west arm of PHENIX. Correct $\sigma_Z$ and $\sigma_\phi$ distributions should have their mean at zero and a width of one. Clearly, strong momentum dependent deviations from the expected values can be observed in Fig.4.2. A similar view is again provided in Fig. 4.3. The layout is analogous to Fig. 4.2 but the depicted results are for the z-matching residuals in 40-60% collisions.

The $p_T$ dependence of the means and widths for $\sigma_z$ and $\sigma_\phi$ distributions was parameterized as a function of centrality and corrected for deviations. The matching corrections were frozen for $p_T > 2.5 GeV/c$. Above this $p_T$ cut-off the matching deviations did not vary much, in accordance with the fact that high momentum tracks form essentially straight lines. Figs. 4.4 and 4.5 show the same quantities as Figs. 4.2 and 4.3, but after the matching corrections are applied. These data clearly indicate significant improvement in the distribution of matching residuals.

Following the calibration of the matching distributions, it is important to carefully determine the effect of matching cuts on the raw $p_T$ spectrum to optimize background rejection. This is explored in Fig. 4.6. The left upper panel in the figure depicts three different uncorrected $p_T$-spectra. The red spectrum was generated without any matching requirement. The blue circles indicate the spectrum after a $|\sigma_z|$ <2.5 and $|\sigma_\phi|$ <2.5 box-cut was applied. The green circles show the $p_T$ spectrum after it was subjected to a radial matching cut of $\sqrt{\sigma_z^2 + \sigma_\phi^2}$ <2. Clearly, the application of a matching cut results in significant background rejection at large transverse momentum. This is demonstrated in the lower left panel of Fig.4.6 which shows the ratio of the uncorrected spectrum without matching requirement to the spectrum generated with radial PC3 association. The ratio of the uncorrected spectrum to the spectrum with the box cut (lower right panel), seems to indicate similarly good background rejection. To further discriminate between radial

and box cuts, the upper right panel shows the ratio of the spectrum with radial matching cut to it's analogue with the box cut. From this plot, one concludes that the radial cut leads to a lower efficiency without resulting in a significant increase in background rejection. Given this, a 2.5 $\sigma$ cut on the PC3 matching on z and $\phi$ was applied in the d+Au analysis. Similar tests were performed for all data sets and resulted in the determination of the following matching requirements.

- d+Au : $|\sigma_z|$ <2.5 and $|\sigma_\phi|$ <2.5

- Au+Au : $\sqrt{\sigma_z^2 + \sigma_\phi^2}$ <2

- Cu+Cu : $\sqrt{\sigma_z^2 + \sigma_\phi^2}$ <2
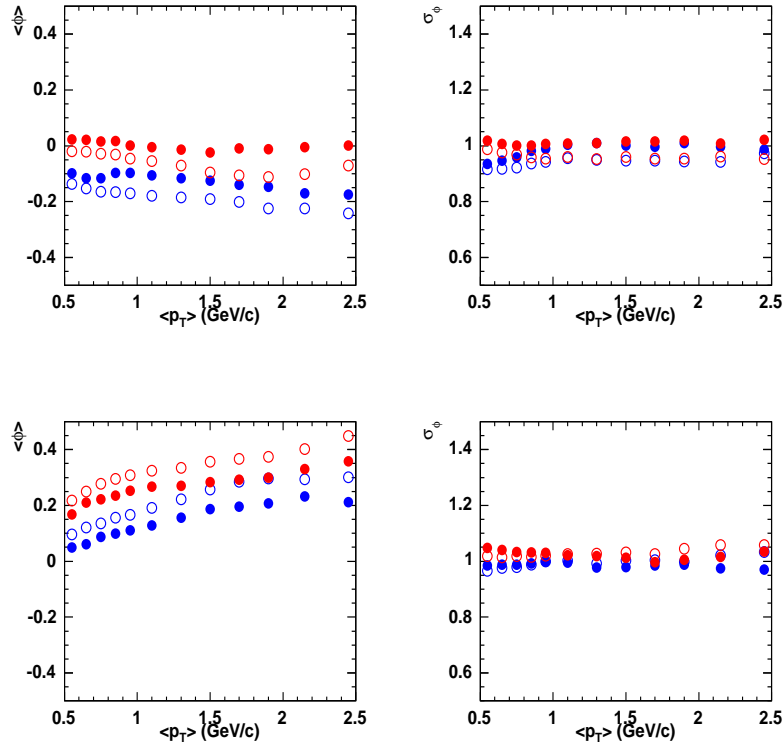
**Figure 4.2:** *Uncorrected mean and width of the $\sigma_\phi$ distribution as a function of $p_T$ for centrality 0-20% . The upper left panel depicts the gaussian means for the east arm and the upper right panel shows the corresponding widths. The red data points represent results for positively charged tracks, and the blue data points are results for negatively charged tracks. Open and filled circles denote data for the north and south side of the east arm, respectively. The lower left and right panels show the identical results to the upper left and right panels, but for the west arm. Correct matching distributions should have their mean at zero and a width of one. Momentum dependent deviations from the expected values can be observed.*

**Figure 4.3:** *Uncorrected mean and width of the $\sigma_z$ distribution as a function of $p_T$ for centrality 40-60% . The upper left panel depicts the gaussian means for the east arm and the upper right panel shows the corresponding widths. The red data points represent results for positively charged tracks, and the blue data points are results for negatively charged tracks. Open and filled circles denote data for the north and south side of the east arm, respectively. The lower left and right panels show the identical results to the upper left and right panels, but for the west arm. Correct matching distributions should have their mean at zero and a width of one. Momentum dependent deviations from the expected values can be observed.*

**Figure 4.4:** *Corrected mean and width of the $\sigma_\phi$ distribution as a function of $p_T$ for centrality 0-20% . The upper left panel depicts the gaussian means for the east arm and the upper right panel shows the corresponding widths. The red data points represent results for positively charged tracks, and the blue data points are results for negatively charged tracks. Open and filled circles denote data for the north and south side of the east arm, respectively. The lower left and right panels show the identical results to the upper left and right panels, but for the west arm. Correct matching distributions should have their mean at zero and a width of one.*
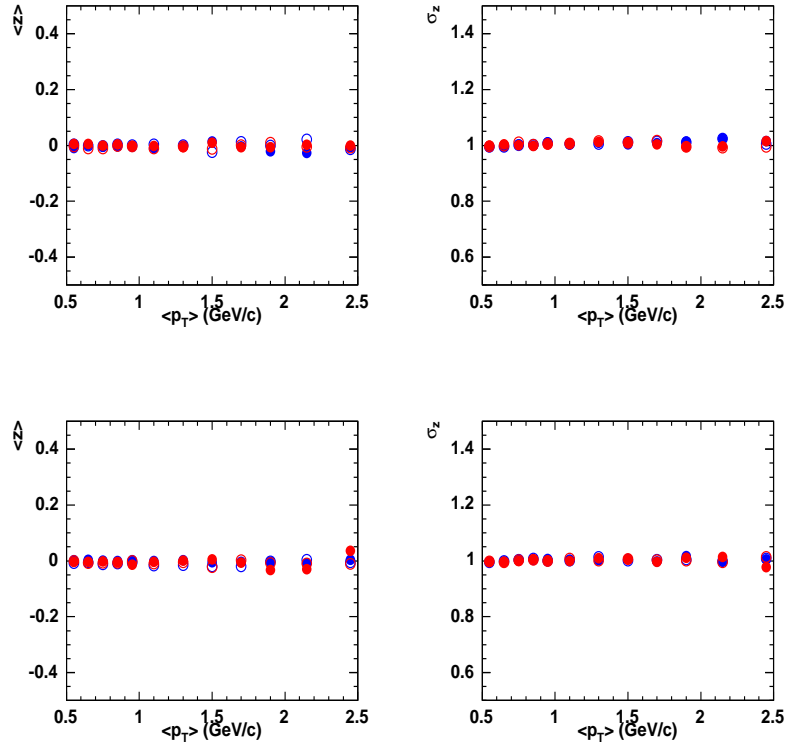
**Figure 4.5:** *Corrected mean and width of the $\sigma_z$ distribution as a function of $p_T$ for centrality 40-60% . The upper left panel depicts the gaussian means for the east arm and the upper right panel shows the corresponding widths. The red data points represent results for positively charged tracks, and the blue data points are results for negatively charged tracks. Open and filled circles denote data for the north and south side of the east arm, respectively. The lower left and right panels show the identical results to the upper left and right panels, but for the west arm. Correct matching distributions should have their mean at zero and a width of one.*
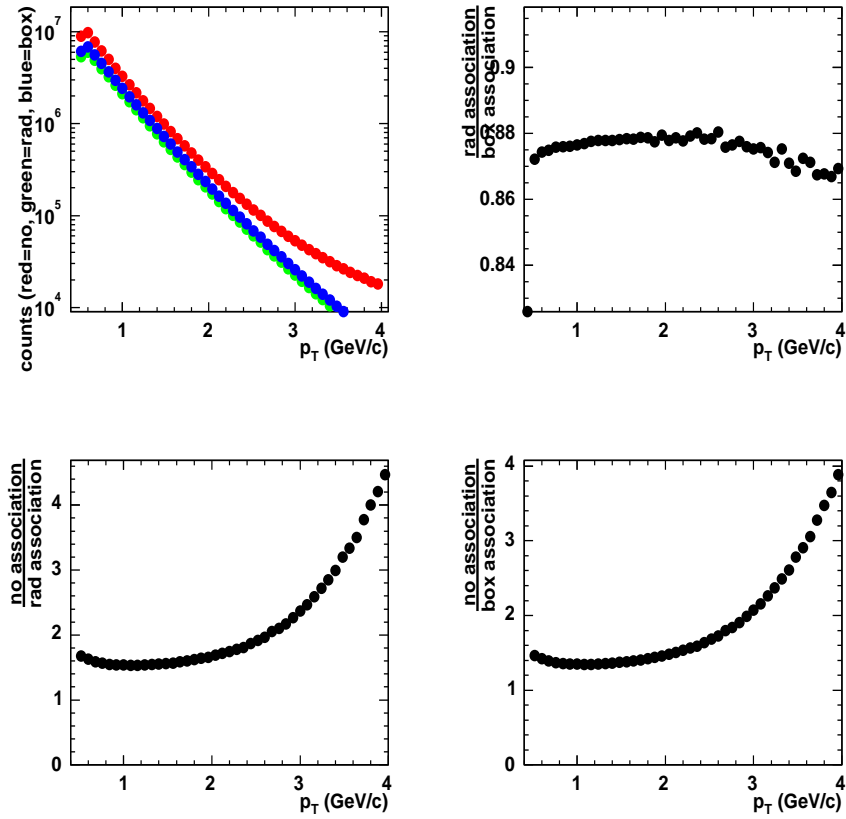
**Figure 4.6:** *The left upper panel depicts three different uncorrected $p_T$-spectra. The red spectrum was generated without any matching requirement. The blue circles indicate the spectrum after a 2.5σ box matching cut was applied. The green circles show the spectrum after it was subjected to a radial matching cut of <2σ. The lower left panel shows the ratio of the red to the green spectrum and the lower right panel shows the ratio of the red to the blue spectrum. The upper right panel shows the ratio of the green to the blue spectrum.*

**Particle Identification**

Particles are identified in the TOF detector and the PbSc via cuts in the mass square ($m^2$) distribution. The $m^2$ can be calculated from the following formula:

$$m^2 = \frac{p^2}{c^2}\left(\left(\frac{t_{tof}c}{L}\right)^2 - 1\right) \tag{4.1}$$

Here, p is the particle's momentum as measured by the Drift Chamber, $t_{tof}$ is the time-of-flight, L is the path length the particle traverses from the vertex to the detector and $c$ is the speed of light.

The mass squared distribution from the PbSc for intermediate transverse momentum particles ($1 < p_T < 2.5 GeV/c$) in Run4 Au+Au collisions is shown in Fig. 4.7. The $\pi$, $K$ and $p$ peaks are clearly distinguishable. Some merging between the $\pi$ and $K$ peaks is observed, but the $p$ peak is very well separated from the mesons. The solid lines in Fig. 4.7 indicate the particle identification cuts that were employed. For the purposes of this work, pions and kaons in the region $-0.3 < m^2 < 0.3 GeV^2$ are designated mesons and protons with mass square $0.7 < m^2 < 1.3 GeV^2$ are called baryons. These cuts maximize baryon/meson separation while simultaneously preserving statistics. The highest transverse momentum window in which associated particles are identified for the correlation analysis presented here, ranges from $1.6 < p_T < 2.0 GeV/c$. The mass squared distribution for this bin is given in Fig.4.8. An estimate of kaon contamination to the baryon window can
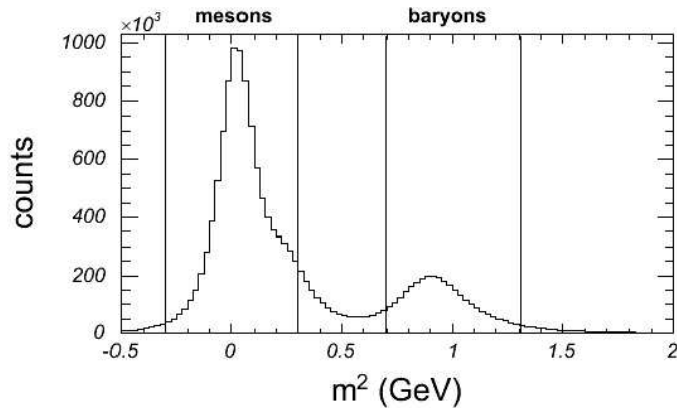
**Figure 4.7:** *Mass square distribution in the PbSc for particles $1 < p_T < 2.5 GeV/c$ from Run4 Au+Au collisions. Particle identification cuts are indicated by the vertical lines.*

be made by simultaneously fitting three gaussian peaks to this distribution. The kaon and pion peaks have become virtually indistinguishable, so that the relative peak position of kaons to pions needs to be fixed from a fit to the low $p_T$ mass squared distribution, where both peaks are well separated. All other parameters in the fit are allowed to vary. The fitted curve is represented by the blue solid line in the figure and the solid black, red and green lines indicate it's respective pion, kaon and proton components. The tails of the gaussian kaon peak hardly contribute any yield to the baryon identification window above $m^2 = 0.7 GeV^2$. The estimated contribution is $\sim 0.22\%$. A similar fit which has been constrained to give maximal K/p overlap clearly does not reproduce the data well (cf. Fig.4.9). The kaon contribution to

baryons for this upper estimate is still below $\sim 3\%$, suggesting that suffi-ciently clean baryon and meson samples are selected by the cuts chosen for this analysis.
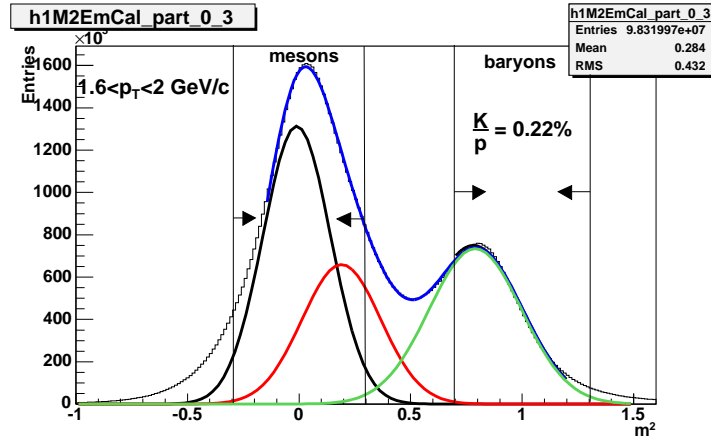


**Figure 4.8:** *Example mass square distribution in the PbSc for particles $1.6 < p_T < 2.0 GeV/c$ from Run4 Au+Au collisions. The blue line indicates a simultaneous fit to the data with three gaussian peaks. The solid black, red and green lines denote respective pion, kaon and proton components from this fit. The relative separation of pion and kaon peaks has been fixed, all other parameters are allowed to vary freely. Particle identification cuts are indicated by the vertical lines.*
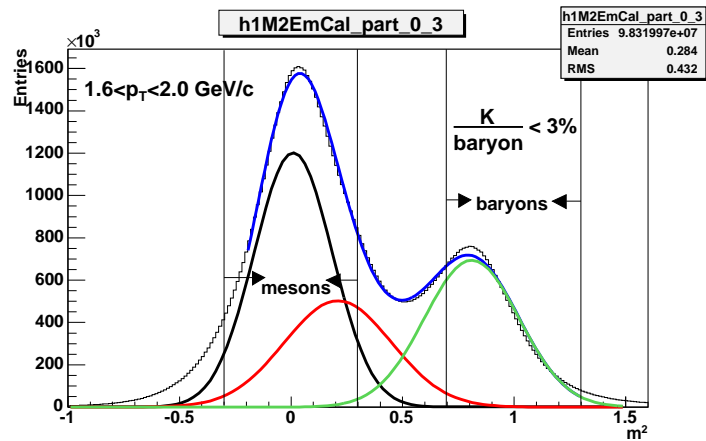
**Figure 4.9:** *Example mass square distribution in the PbSc for particles $1.6 < p_T < 2.0 GeV/c$ from Run4 Au+Au collisions. The blue line indicates a simultaneous fit to the data with three gaussian peaks. The solid black, red and green lines denote respective pion, kaon and proton components from this fit. The fit has been constrained to give a maximum kaon/proton overlap. Particle identification cuts are indicated by the vertical lines.*

## 4.2 Extracting Correlation Functions

Section 3.1 introduced the correlation function in azimuthal pair separation ($C(\Delta\phi)$, where $\Delta\phi = (\phi_1 - \phi_2)$) as the ratio of a foreground distribution $N_{cor}$, constructed with correlated particle pairs from the same event, and a background distribution $N_{mix}$, obtained by randomly pairing particles from different events within the same centrality and vertex classes.

$$C\left(\Delta\phi\right) \propto \frac{N_{cor}\left(\Delta\phi\right)}{N_{mix}\left(\Delta\phi\right)} \tag{4.2}$$

This section reports on the extraction of robust correlation functions from the data.

### 4.2.1 Subtleties of Mixed Pair Distributions

In the ideal case of a perfect detector, the distribution of particle pairs from the same event would only contain physics correlations, and it would be sufficient to determine $N_{cor}$ to reproduce those correlations. However, no detector is perfect and thus the shape of $N_{cor}$ will generally reflect both physics correlations as well as detector acceptance and efficiency effects. Pairs that are obtained by mixing particles from different events do not carry the physics correlations of interest. In an ideal detector, the background distribution $N_{mix}$ would thus be isotropic. In a realistic detector it reproduces the detector acceptance and efficiency. Therefore, the correlation function accurately

recovers the true physics correlations, since detector acceptance and efficiency cancel in the ratio of foreground to background distribution, as demonstrated analytically in section 3.1. For this to be strictly true, though, the event averaged background distribution has to accurately reproduce the pair-acceptance/efficiency of the event averaged foreground distribution. Several experimental effects need to be carefully accounted for, to assure that this requirement is met.

The experimental acceptance is different if a collision happens at the midpoint of the PHENIX detector, or more toward the edges. This effect can be controlled by only pairing particles from events that belong to the same z-vertex class. Only events with BBC z-vertex of $\pm$ 30 cm are used to construct the correlation function, and a division of the vertex distribution into 12 classes ($\pm 5$ cm each) is sufficient to avoid the possible effects of a varying acceptance with collision vertex position. To further ensure sampling from events with similar multiplicity, the background distribution was constructed from mixed events having the same centrality range as the events of the foreground distribution.

There are two other important experimental effects that can introduce distortions in the correlation function; time dependent efficiency fluctuations can result in the event averaged background distribution not correctly reproducing the acceptance/efficiency function of the event averaged foreground distribution. Furthermore, track merging and/or splitting effects can distort

the correlation functions at small angles. Occasionally, the track model reconstructs a track multiple times, resulting in a family of tracks for which almost every parameter is similar. This effect is referred to as track splitting or "ghosting" and will manifest itself as a peak at low angles in the correlation function. Track merging arises from the fact, that the foreground distribution has to reflect the two track resolution of the detector, while (in principle) pairs of tracks that are randomly combined in the background could be infinitely close. Track merging will result in a dip at the correlation function at small $\Delta\phi$.

In the following, we describe these effects in greater detail and report on the analysis steps taken to minimize their influence. In addition, we describe many of the tests undertaken to insure the generation of robust correlation functions from the data.

### Influence of Time-dependent Efficiency Fluctuations on Mixed Pair Distributions

On occasion one or more high voltage modules can temporarily fail during data taking, resulting in a change of the detector efficiency. If this happens with sufficient frequency over the duration of a Run, significant time dependent efficiency fluctuations could be introduced in the data. Generating background pairs by mixing particles from events with very different efficiencies can result in the background distribution not faithfully reproducing the

pair-efficiency of the foreground distribution. A correlation function that has been formed by taking the ratio of foreground to background distributions with different pair-efficiencies, can exhibit sizable distortions, depending on the magnitude of the efficiency fluctuations.

Fig. 4.10 demonstrates this effect. Four correlation functions are shown which were obtained from simulated events in which particles were detected with a slow varying time-dependent efficiency (Simulation courtesy N. N. Ajitanand). The efficiency fluctuations were modeled after the real data. The upper panels depict correlation functions for the case of isotropic particle emission. In the absence of pathological effects, these correlation functions should be flat. The left upper panel shows a case where the background distribution was constructed from events separated by long time periods and therefore characterized by different efficiencies. This correlation function exhibits sizable spurious correlations. The right upper panel demonstrates that the correlation function becomes flat, when foreground and background distributions are generated from events close in time, that have similar efficiency. The left lower panel and right lower panel also depict correlation functions obtained by mixing particles across regions of fluctuating efficiency and with the same efficiency, respectively. However, for these correlation functions particle emission followed a harmonic pattern. The lower left correlation function with different average pair efficiency for foreground and background clearly indicates that mixing across regions of fluctuating efficiency can serve

to distort the correlation signal which is reproduced correctly by the lower right correlation function, generated from events with the same efficiency.

**Reducing Time-dependent Efficiency Fluctuations**

A novel QA technique has been used to reliably identify time-dependent efficiency fluctuations in the data, thereby allowing to carefully select run groups with similar pair efficiency for background mixing. This method relies on the idea that the background distribution obtained by mixing particles from unrelated events is a measure of the pair acceptance/efficiency. Following this idea, a simple concept has been developed. Since each run is comprised of various segments whose numbers ascend with time, variations in the mixed event distribution with run segment can be interpreted as signals for a time dependent change in the particle pair efficiency. Consequently, mixed event background distributions were generated for each run segment, and the ratio of the integrated pair yield for 0-90° and 90-250° (of the unfolded mixed event distribution) was studied as a function of run segment. In the absence of time-dependent efficiency fluctuations, the mixed event background distributions for different run segments are expected to be identical and this ratio would be constant. Figure 4.11 shows representative examples of the segment dependence of the integrated yield ratio for the Run2 dataset. Segments from the same run are shown with the same color. For the most part, the runs
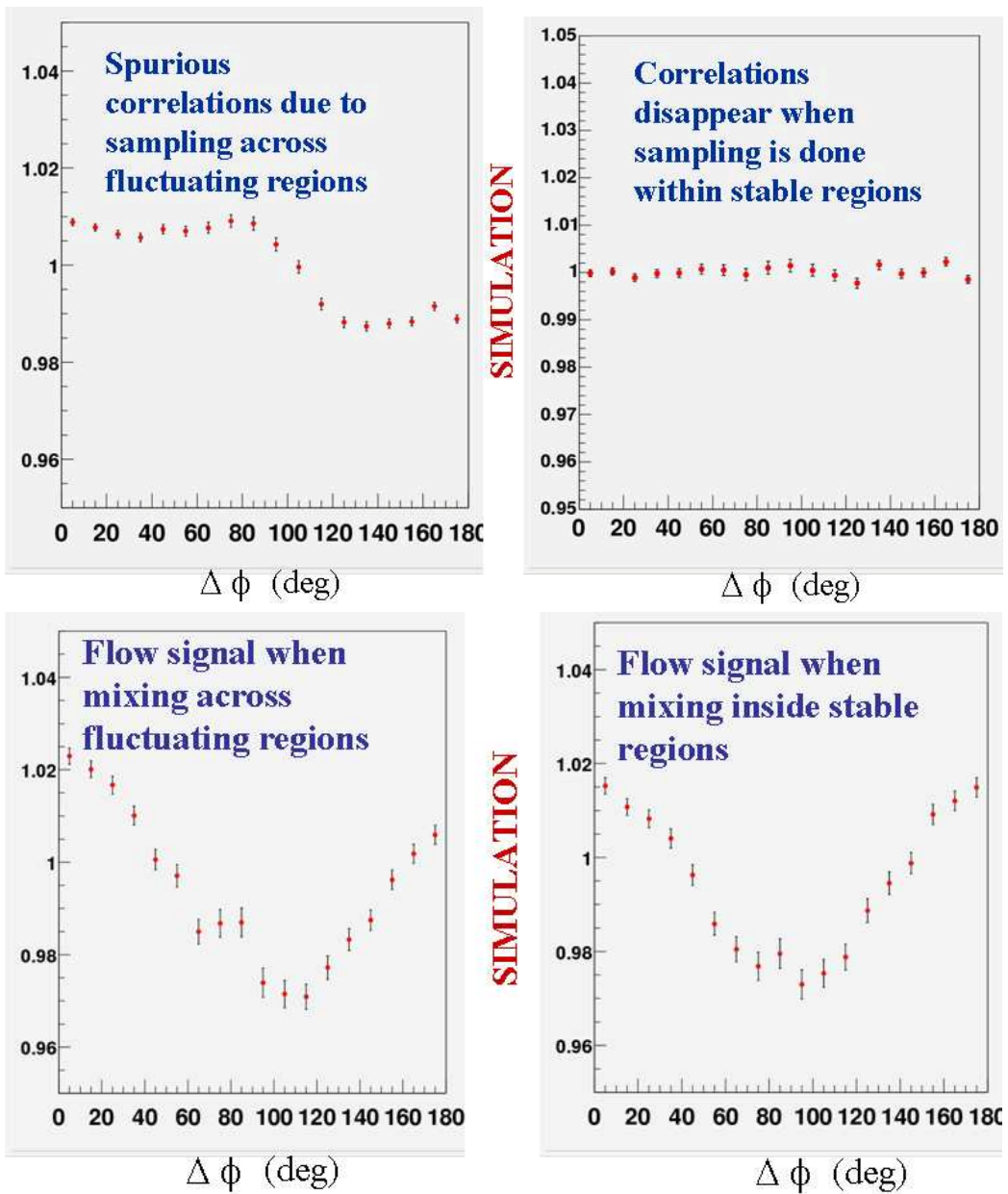
**Figure 4.10:** *Simulated correlation functions. Upper left panel: Isotropic particle emission and background construction across events of varying efficiency. Upper right panel: Isotropic particle emission and background construction from events with the same efficiency. Lower panel same as upper panel but for harmonic particle emission. Simulation results courtesy N. N. Ajitanand.*

were pretty stable, but several cases can be identified in which the pair efficiency varies rapidly within a run. These latter runs have been denoted "bad" and excluded from further analysis. A similar pair QA study has been performed for the Run4 and Run5 datasets (Au+Au and Cu+Cu collisions at $\sqrt{s_{NN}} = 200 GeV$, respectively). The pair efficiency for these later datasets was found to be much more stable than that for Run 2. To further minimize the influence of time dependent pair efficiency fluctuations, the mixed event background is constructed by only pairing particles from events that belong to the same run (called "proximity mixing"). This is done, so that variations of pair-efficiency across runs do not influence the construction of the mixed pair distribution. It should be noted at this stage, that the utilization of mixing techniques that require the crossing of run boundaries requires sufficient care to insure that mixing only takes place within a group of runs with the same average pair efficiency.
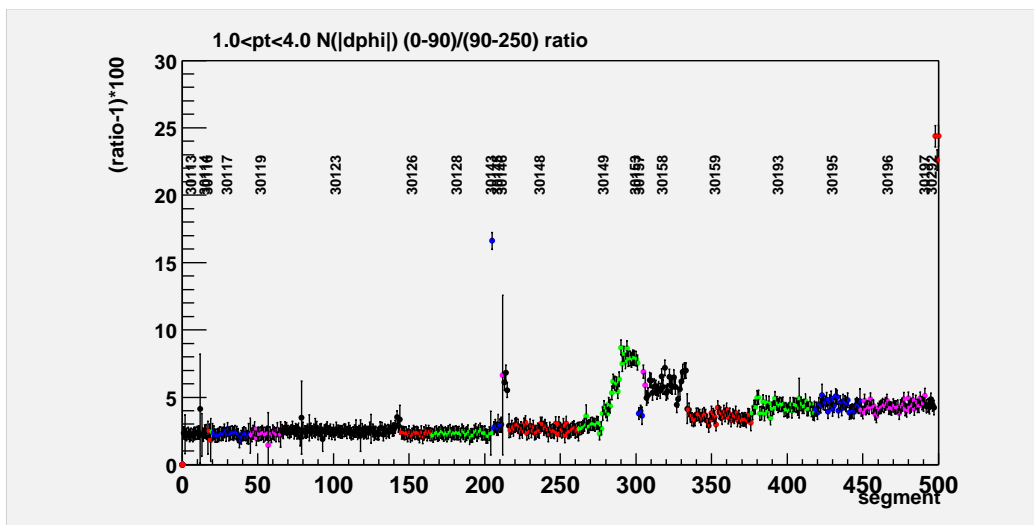
**Figure 4.11:** *Mixed-pair yield ratio (0-90°/90-250°) vs. run segment for several runs as indicated. Figure courtesy N. N. Ajitanand.*

## 4.2.2   Determining Pair Cuts

In earlier parts of this chapter it was pointed out that track splitting ("ghost-ing") or track merging can result in the foreground and background distribu-tion not having the same pair-acceptance/efficiency at small angles. When the correlation function is generated as the ratio of these two distributions, distortions at small $\Delta\phi$ can result. It is therefore important to carefully evaluate the track pair efficiency as a function of centrality and $p_T$, in or-der to determine regions of over-/under-efficiencies. The standard procedure for correlation analyses is to build correlation functions in the relevant pair-efficiency variables. If foreground pairs from the same event and background pairs formed with tracks from different events had the same pair-efficiency, these correlation functions would be flat. Any deviation from a flat distri-bution is an indication for pair-inefficiencies or over-efficiencies and serves to determine a robust set of pair cuts. After these cuts have been applied to foreground and background, both distributions should have the same pair-efficiency which will then cancel when the correlation function is formed. The procedure is common to all datasets. In what follows, the process is illustrated, and a complete list of pair-cuts for each data set is given.

A first cut, that needs to be applied when studying identified particles is the rejection of all tracks that share the same EmCal tower or ToF slat. This cut removes tracks with bad timing information from the sample, and

significantly reduces track splitting effects [C$^+$05].

Prime variables for the study of pair cuts are $\Delta\phi_{dc}$ (the relative azimuthal difference of two tracks at the DC reference radius) and $\Delta zed$ (the separation of two tracks in the z-coordinate from the track model). Figure 4.12 depicts the two dimensional correlation function in these quantities for Run4 Au+Au collisions after tracks that share the same EmCal tower (ToF slat) were removed. This correlation function is relatively flat, except at small $\Delta\phi_{dc}$ and $\Delta zed$, where track merging produces a dip and track splitting results in a double peak structure. This double peak can be traced to pair contributions from different charge combinations. Figure 4.13 shows the same correlation functions for opposite charge pairs (left panel) and same charge pairs (right panel). Clearly, different regions of pair in-efficiencies and over-efficiencies can be identified in the charge separated correlation functions. These regions sum to the observed structures in the charge averaged $\Delta\phi_{dc}$-$\Delta zed$-plane.

A more differential view of track efficiencies is provided in Figs. 4.14, 4.15 and 4.16 which represent correlation functions in $\Delta\phi_{dc}$ for several $\Delta zed$ projections of same charge pairs, as indicated. Figure 4.14 shows $\Delta\phi_{dc}$ correlation functions for $\Delta zed < 1cm$ (left panel) and $1 < \Delta zed < 2cm$ (right panel). Figure 4.15 depicts the same correlation functions for $2 < \Delta zed < 3cm$ (left panel) and $3 < \Delta zed < 4cm$ (right panel). Finally, Fig. 4.16 shows $\Delta\phi_{dc}$ correlation functions for $4 < \Delta zed < 5cm$ (left panel) and $5 < \Delta zed$ (right panel). It is interesting to note, that track splitting mainly contributes

to the $\Delta\phi_{dc}$ correlation function for $\Delta zed < 1cm$. For projections with $\Delta zed > 1cm$, track merging effects dominate.

These studies suggest, that two different sets of pair cuts for opposite charge and same charge pairs are needed for the Run4 data. Such a strong charge correlation was not observed in the earlier Run2 and Run3 datasets, and could probably be attributed to the increased magnetic field strength for the later running periods.
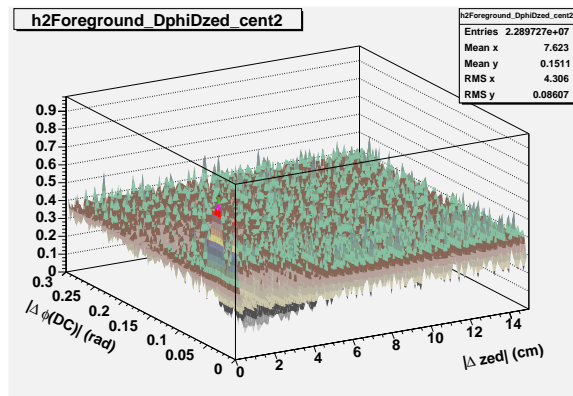


**Figure 4.12:** *Two-dimensional correlation function in $\Delta\phi_{dc}$ and $\Delta zed$ for charged track pairs after pairs of particles that share the same EmCal tower were removed. One observes clearly areas of track merging and track splitting (ghosting).*

Another view of the track merging and splitting problem is given in Fig. 4.17, which examines the difference in PC1 radial projections ($\Delta R_{PC1} = \sqrt{(ppc1x_1 - ppc1x_2)^2 + (ppc1y_1 - ppc1y_2)^2 + (ppc1z_1 - ppc1z_2)^2}$, with ppc1x, ppc1y and ppc1z being the projected coordinates in x, y and z-direction from
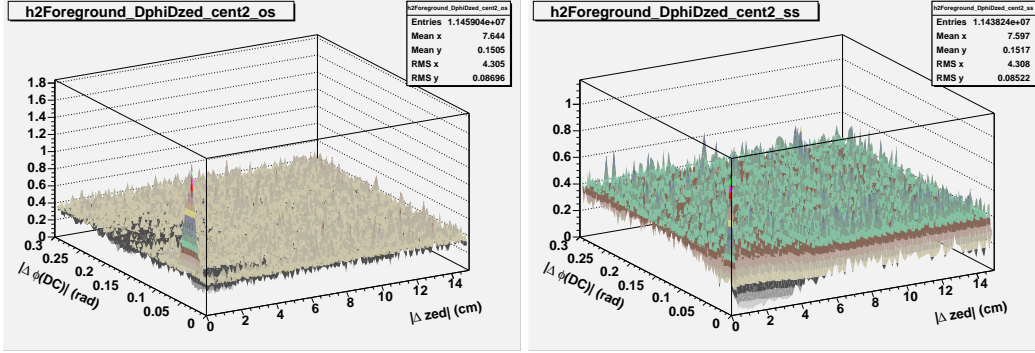
**Figure 4.13:** *Two-dimensional correlation functions in $\Delta\phi_{dc}$ and $\Delta zed$ for opposite charge pairs (left panel) and same charge pairs (right panel) after pairs of particles that share the same EmCal tower were removed. Different charge combinations show enhancements and deficiencies in different regions that combine to the observed structures in the charge averaged $\Delta\phi_{dc}$-$\Delta zed$-plane.*
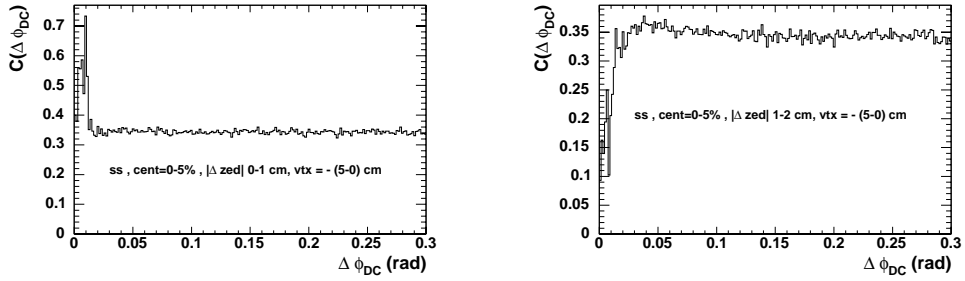


**Figure 4.14:** *$\Delta\phi_{dc}$ correlation function for same charge pairs with $0 < \Delta zed < 1$ cm (left panel) and $1 < \Delta zed < 2$ cm (right panel). Pairs of particles that share the same EmCal tower were removed.*
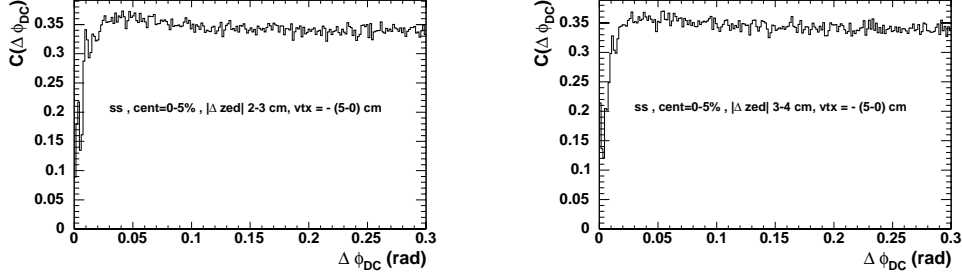
**Figure 4.15:** $\Delta\phi_{dc}$ *correlation function for same charge pairs with* $2 < \Delta zed < 3$ *cm (left panel) and* $3 < \Delta zed < 4$ *cm (right panel). Pairs of particles that share the same EmCal tower were removed.*
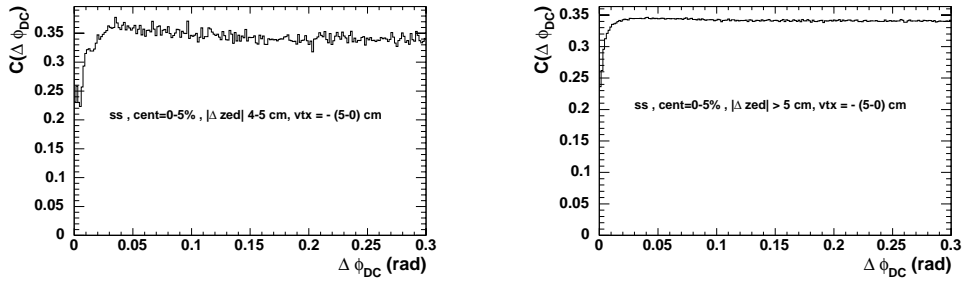


**Figure 4.16:** $\Delta\phi_{dc}$ *correlation function for same charge pairs with* $4 < \Delta zed < 5$ *cm (left panel) and* $5 < \Delta zed$ *cm (right panel). Pairs of particles that share the same EmCal tower were removed.*

the track model) for track pairs from Cu+Cu. The right panel depicts the foreground distribution (black data points) and background distribution (red data points) in this variable. Both distributions have been normalized at

large $\Delta R_{PC1}$. One observes, that foreground and background are very similar except at small $\Delta R_{PC1}$. This is emphasized in the left panel, which shows the ratio of the two distributions. One can clearly see the effects of track splitting at $\Delta R_{PC1} < 2cm$ and track merging at $\Delta R_{PC1} < 7cm$. In order to
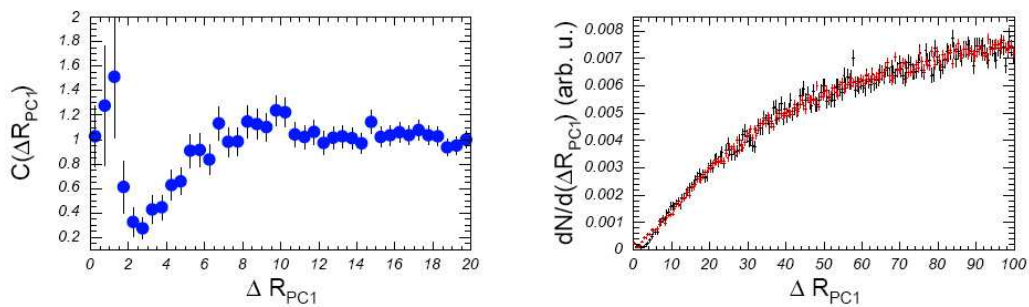


**Figure 4.17:** *Right panel: foreground (black) and background (red) distributions in PC1 radial projections $\Delta R_{PC1}$. Left panel: The ratio of both distributions. Results are for Cu+Cu collisions.*

trace track merging (ghosting) throughout the detector layers, it is instructive to investigate the correlation between the differences in PC1 and PC3 radial projections. Figure 4.18 shows two-dimensional correlation functions for the difference in PC1 and PC3 radial projections generated for opposite charge (left panel) and same charge pairs (right panel) in Run4 Au+Au collisions. The regions of pair inefficiencies and over-efficiencies differ in the two correlation functions, indicating that separate cuts are required for pairs of opposite or same charge tracks. It is worthwhile to mention, that since the PC3 is mounted directly before the EmCal, $\Delta R_{EmCal}$ could also be used
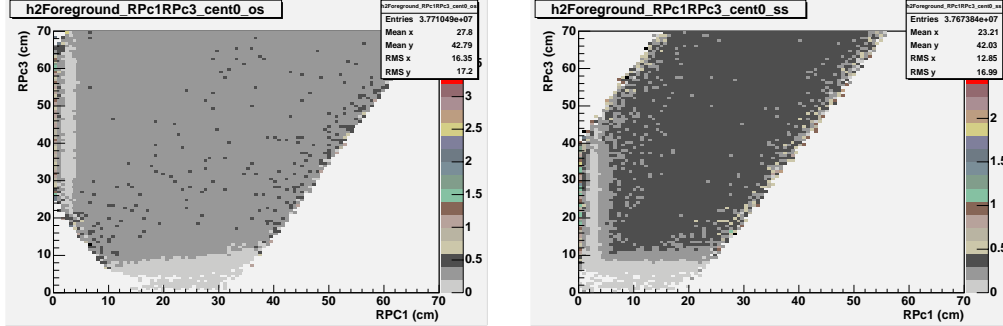
**Figure 4.18:** *Two-dimensional correlation functions in $\Delta R_{PC3}$ and $\Delta R_{PC1}$ for opposite charge pairs (left) and same charge pairs (right) after pairs of particles that share the same EmCal tower were removed. One observes clear regions of track merging and track splitting (ghosting). The data are from Run4 Au+Au*

instead of $\Delta R_{PC3}$, to evaluate the pair inefficiencies. Such an approach has been used for the Run2 Au+Au data set. From the correlation functions in Fig. 4.18, the following cuts on $\Delta R_{PC3}$ and $\Delta R_{PC1}$ are determined. Same charge pairs: $\Delta R_{PC1} >7$ cm and $\Delta R_{PC3} >14$ cm. Opposite charge pairs: $\Delta R_{PC1} >5$ cm and $\Delta R_{PC3} >14$ cm.

A careful investigation of $\Delta\phi_{dc}$ distributions (for different selections of $\Delta zed$) after the cuts in $\Delta R_{PC3}$ and $\Delta R_{PC1}$ have been applied can serve to identify any residual pair inefficiencies. Such a study is illustrated for opposite charge pairs by Figs. 4.19, 4.20 and 4.21. Although the distributions in Figs. 4.19 - 4.21 look much better than before the PC1-PC3 cuts were invoked, small, residual track merging effects are indeed present in these

distributions and can easily be removed by the appropriate cuts in $\Delta\phi_{dc}$. The identical investigation for same charge pairs gave similar results. The complete list of cuts used to remove track splitting (ghosting) and track merging for the different data sets is given in Tab. 4.1.
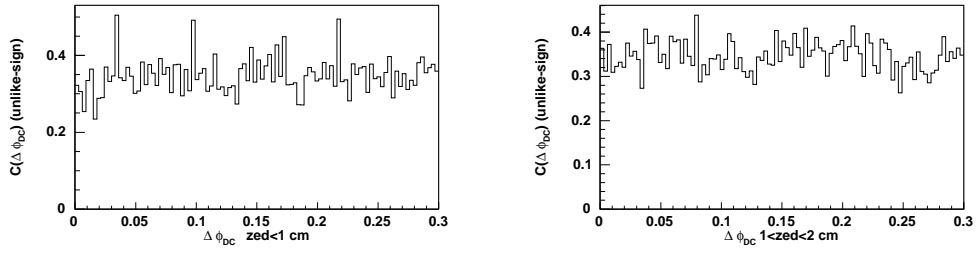


**Figure 4.19:** $\Delta\phi_{dc}$ *correlation function for same charge pairs with* $0 < \Delta zed < 1$ *cm (left panel) and* $1 < \Delta zed < 2$ *cm (right panel). Pairs of particles that share the same EmCal tower were removed and* $\Delta R_{PC1}$ *and* $\Delta R_{PC3}$ *cuts have been applied.*
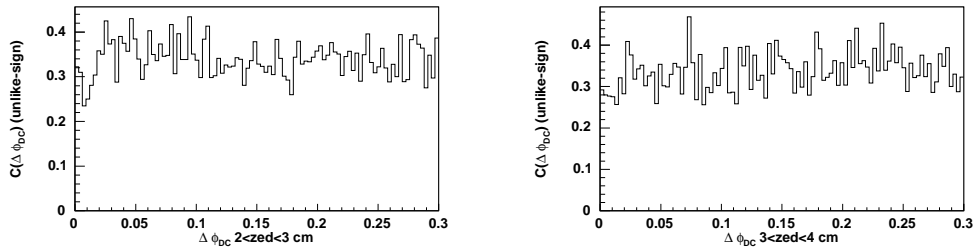


**Figure 4.20:** $\Delta\phi_{dc}$ *correlation function for same charge pairs with* $2 < \Delta zed < 3$ *cm (left panel) and* $3 < \Delta zed < 4$ *cm (right panel). Pairs of particles that share the same EmCal tower were removed and* $\Delta R_{PC1}$ *and* $\Delta R_{PC3}$ *cuts have been applied.*
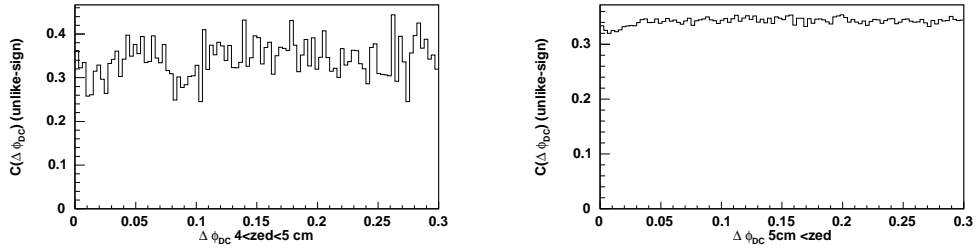
**Figure 4.21:** $\Delta\phi_{dc}$ *correlation function for same charge pairs with* $4 < \Delta zed < 5$ *cm (left panel) and* $5 < \Delta zed$ *cm (right panel). Pairs of particles that share the same EmCal tower were removed and* $\Delta R_{PC1}$ *and* $\Delta R_{PC3}$ *cuts have been applied.*

**Table 4.1:** *Pair cuts utilized for the four data sets in this analysis.*

| Data set and pair cuts |
|:---:|
| Run3 d+Au |
| $\Delta R_{PC1} > 7cm, \Delta R_{PC3} > 14cm,$ |
| $\Delta\phi_{dc} > 0.03rad, \Delta zed > 0.28cm$ |
| Run2 Au+Au |
| $\Delta R_{PC1} > 7cm, \Delta R_{EmCal} > 16cm,$ |
| $\Delta\phi_{dc} > 0.02rad$ for $\Delta zed < 5cm$ |
| and $\Delta\phi_{dc} > 0.01rad$ for $\Delta zed > 5cm$ |
| Run4 Au+Au like sign |
| $\Delta R_{PC1} > 7cm, \Delta R_{PC3} > 14cm,$ |
| $\Delta\phi_{dc} > 0.02rad$ for $\Delta zed < 5cm$ |
| and $\Delta\phi_{dc} > 0.01rad$ for $\Delta zed > 5cm$ |
| Run4 Au+Au unlike sign |
| $\Delta R_{PC1} > 5cm, \Delta R_{PC3} > 14cm, \Delta\phi_{dc} > 0.05rad$ |
| Run5 Cu+Cu like sign |
| $\Delta R_{PC1} > 7cm, \Delta R_{PC3} > 15cm$ |
| $\Delta\phi_{dc} > 0.03rad$ if $\Delta zed < 0.5cm$ |
| and $\Delta\phi_{dc} > 0.01rad$ for $\Delta zed > 0.5cm$ |
| Run5 Cu+Cu unlike sign |
| $\Delta R_{PC1} > 7cm, \Delta R_{PC3} > 15cm$ |
| $\Delta\phi_{dc} > 0.1rad$ if $\Delta zed < 1cm$ |
| and $\Delta\phi_{dc} > 0.01rad$ for $\Delta zed > 1cm$ |

## 4.2.3 Checks for Robust Correlation Functions

After applying the pair-QA and pair-cut studies described above, several tests were made to check and cross check the robustness and stability of the resulting correlation functions. These tests included (i) a check for whether or not the correlation functions were invariant to different mixing techniques, and (ii) a check to see if the correlation functions generated by summing over several data subsets comprising the entire data set, gave the same result as the sum of the averaged individual correlation functions generated from the individual runs which comprise the full data set. The availability of Au+Au data from two distinct running periods (Run2 (2002) and Run4 (2004)) also provides for an additional level of cross checks. That is, if robust correlation functions have been obtained, they should be identical within statistical errors, for both running periods.

**Invariance of Correlation Functions to Mixing Techniques**

Different algorithms can be employed to generate the mixed event background distribution for a correlation function analysis. If utilized correctly, they should all lead to the same mixed event distribution and consequently the same correlation function. Deviations from that expectation could arise if sampling is incomplete or if one of the methods suffers from pathologies

of one sort or another. Here, it is investigated whether the extracted correlation functions are indeed invariant under the two most commonly used mixing techniques.

The first of these techniques, the rolling buffer method, correlates all particles in an event that pass a set of track selection criteria with all other particles from a different event, that also fulfill the same selection criteria.

By contrast, the random track method constructs a "pseudo" event by randomly selecting particles, each from a different event. An important constraint is that no two particles are picked from the same event. Mixed background pairs are then created analogous to foreground pairs by building pair combinations from the tracks in the pseudo event.

These two procedures differ in that the first results in track mixing which spans a very short period of data taking. The second needs deep pools to avoid reusing a single track multiple times ("oversampling"). This requirement very often makes it necessary to cross run boundaries when building a mixed pair distribution with the random track method. It was demonstrated in section 4.2.1 that the construction of a mixed pair background from runs with different average pair efficiency can lead to distortions in the correlation function. Therefore, great care needs to be taken in the random track method to ensure the grouping of runs with similar pair efficiency.

This was achieved by first grouping runs based on the ratio of the integrated pair yield for the 0-90° and 90-250° regions in the unfolded mixed

event distribution, as described earlier. To make sure that all runs in a group have the same average pair efficiency, the mixed event background of every run was divided by the average mixed-event background of the group and area normalized. If the pair efficiency of the run matches the average pair efficiency of it's run group, this ratio should be flat over the whole $\Delta\phi$ range with a value of one.

This is demonstrated by Figs. 4.22 and 4.23 which show examples of improper and proper run grouping, respectively. Turning first to the left panel in Fig. 4.22, the single particle $\phi$ distributions for a specific run in the group (black histogram) is compared to the average $\phi$ distribution of the run group (red histogram). The area normalized ratio of the mixed event background of the run to the average mixed-event background of the entire run group is depicted in the right panel. Sizable distortions in this ratio indicate a bad run grouping.

Figure 4.23 shows the same quantities as Fig 4.22, but this time for a proper run grouping. That is, the ratio of mixed event background distributions is flat at one, demonstrating that the run under investigation has the same average pair efficiency as the entire run group.

Once proper run grouping had been established, the random track mixing method was utilized to generate a full set of correlation functions. The black data points in Fig. 4.24 depict a representative correlation function from this set. In the example given here, the trigger particle has been constrained in a
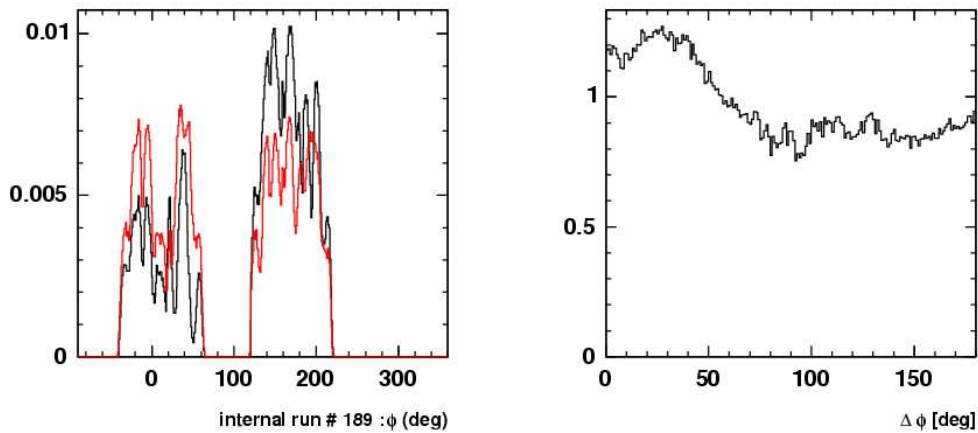
**Figure 4.22:** *Example of improper run-grouping. The left panel shows a comparison of the single particle $\phi$ distribution of a representative run (black histogram) to the average $\phi$ distribution of its run group (red histogram). The area normalized ratio of the mixed event background of the run to the average mixed-event background of the run group is depicted in the right panel.*

window perpendicular to the reaction plane to yield an out-of-plane correlation function (see section 3.3.1). Therefore the harmonic component of the correlation function has a shifted phase compared to an inclusive correlation function. Also shown in Fig. 4.24 is the same correlation function generated via the rolling event buffer method (red data points). Both correlation functions agree to within statistical errors.

Similar comparisons for other correlation functions yielded equally good agreement, indicating that the correlation functions presented in this work do not depend on the choice of mixing technique. This is attributable to
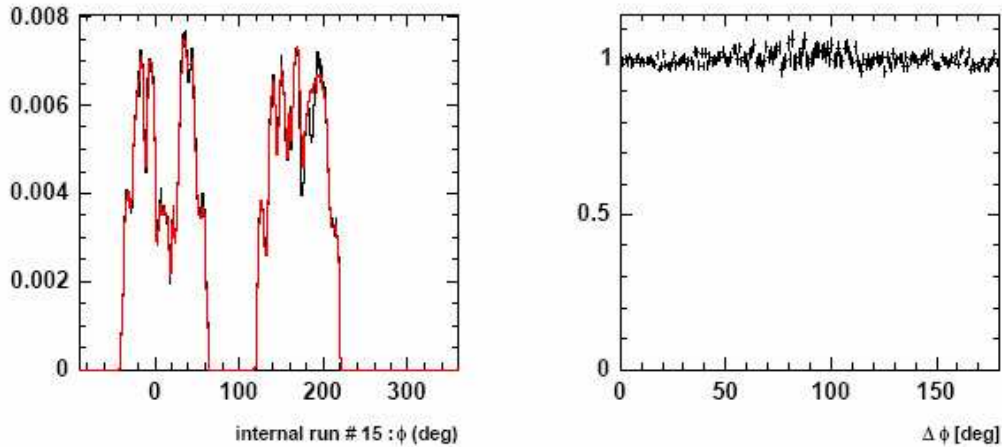
**Figure 4.23:** *Example of proper run-grouping. The left panel shows a comparison of the single particle $\phi$ distribution of a representative run (black histogram) to the average $\phi$ distribution of its run group (red histogram). The area normalized ratio of the mixed event background of the run to the average mixed-event background of the run group is depicted in the right panel.*

the careful studies made to establish a robust set of pair-cuts etc. Final correlation functions for this dissertation were generated via the rolling buffer mixing method.

## Average of Ratios vs. Ratio of Sums

If robust correlation functions have been obtained, they should be invariant under the method of averaging used. That is, the correlation functions generated by summing over several data subsets comprising the entire data set (the ratio of sums), are expected to give the same result as the sum of
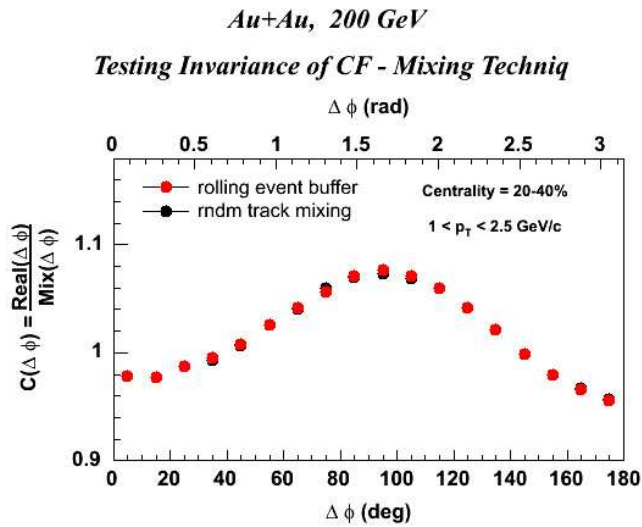
**Figure 4.24:** *Comparison of out-of-plane fixed-$p_T$ ($1 < p_T < 2.5$ GeV/c) corre-lation functions obtained via two different methods for generating the mixed-event distribution. The red data points denote the correlation function generated via the event-based mixing technique and the black data points represent the correlation function obtained via random track mixing. The centrality range is 20-40%.*

the averaged individual correlation functions generated from the individual runs which comprise the full data set (average of ratios). This is verified in Fig.4.25 which shows excellent agreement between the correlation functions obtained via the ratio of sums (black data points) and average of ratios (red data points)
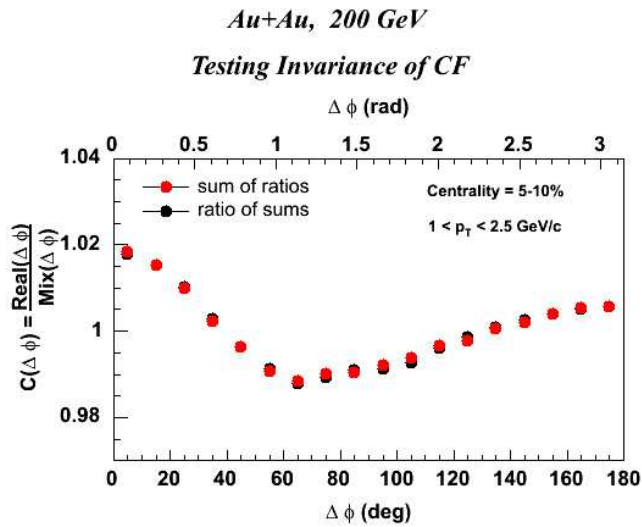
**Figure 4.25:** *Comparison of correlation functions obtained via the ratio of sums (black data points) and the average of ratios (red data points). (see text)*

## Comparison of Au+Au correlation functions from Run2 and Run4

An additional check if stable correlation functions have been generated is to compare the correlation functions across running periods. If the correlation functions are stable, the expectation is that they should be essentially the same for both datasets. The detector may change over time, the physics, however, should not. Fig. 4.26 compares fully identified Au+Au correlation functions from Run4 to Run2 correlation functions obtained for the same cuts from a separate analysis (Run2 data courtesy A. Taranenko). In this case, both the trigger and the associated partner particle for the correlation functions in Fig. 4.26 are identified as either a meson or a baryon. Run4

results are shown as filled colored symbols and Run2 results are depicted as open circles. Good agreement between the two datasets is indeed observed for all correlation functions.
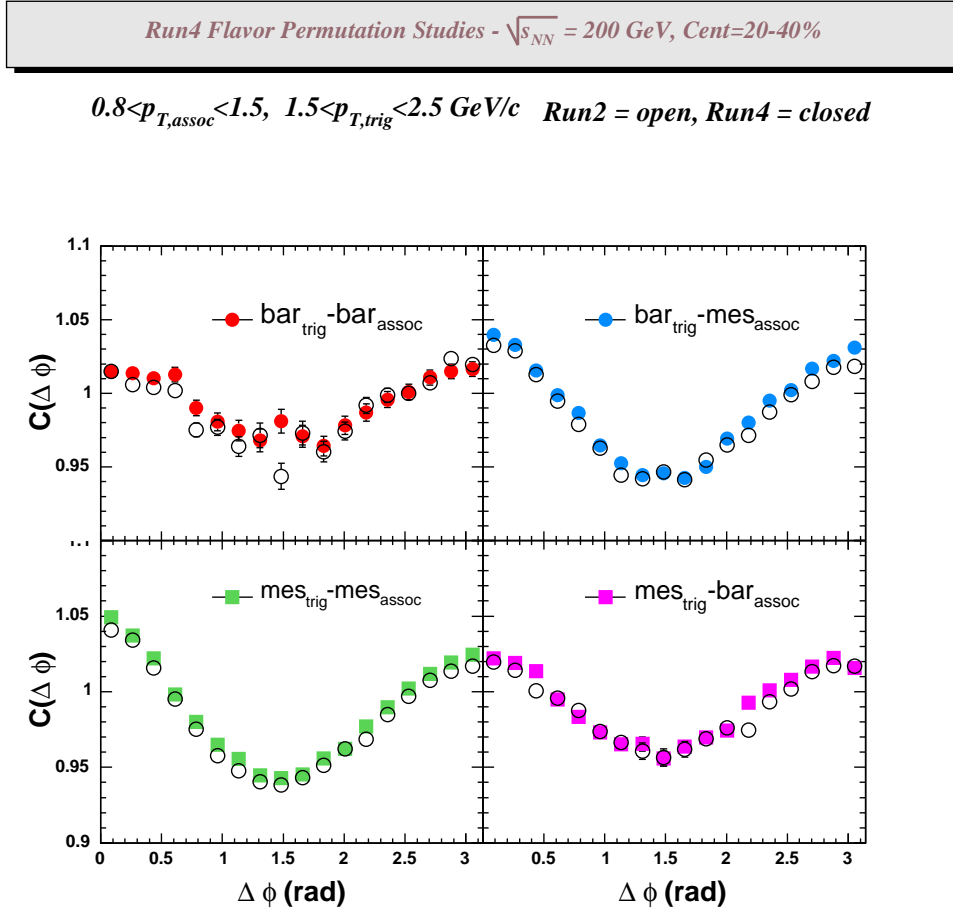
**Figure 4.26:** *Comparison of correlation functions with identified trigger and partner particles from Run2 and Run4. Run4 results are shown as filled, colored symbols and Run2 results are depicted as open circles. Good agreement between the two datasets is evidenced by all correlation functions. (Run2 data courtesy A. Taranenko)*

# Decomposition of Correlation Functions

Once robust correlation functions have been obtained, it is necessary to separate the jet-signal from the underlying event. Different decomposition procedures based on a two source model were described in chapter 3. This chapter reports on the application of those procedures to the experimental correlation functions. Section 5.1 focuses on the characterization of jet pair distributions in d+Au. After discussion of the extraction of the $v_2$ parameter via the reaction plane method, the correlation functions in Au+Au and Cu+Cu are decomposed into their respective (di)jet and flow components.

## 5.1 Decomposition of d+Au Correlation Functions

Figure 5.1 depicts four assorted $p_T$ correlation functions for 0-80% d+Au collisions. Two $p_T$ windows for the trigger hadron and associated partner particle are explored. In panels (a,b) the trigger hadron is chosen between $2.5 < p_T < 4 GeV/c$ and in panels (c,d) the trigger $p_T$ selection is $4 < p_T < 6 GeV/c$. The associated $p_T$ window is either $1.5 < p_T < 2 GeV/c$ for panels (a) and (c) or $2 < p_T < 2.5 GeV/c$ for panels (b) and (d). One clearly observes a double peak structure, indicative of (di)jet correlations. These peaks narrow in width and grow in amplitude as the $p_T$ of either the trigger (cf. panel (a) and (c)) or the associated particle (cf. panel (a) and (b)) is raised. If the $p_T$ range for both particles is high enough, the double peak signal emerges clearly over a flat (ie, isotropic) background (see panel (d)). This $p_T$-dependence of the peaks is characteristic of correlations dominated by jets. Consequently, contributions from harmonic correlations due to flow were assumed to be negligible and all azimuthal correlation in d+Au collisions is attributed to (di)jets and an isotropic underlying event;

$$C(\Delta\phi) = a_\circ + J(\Delta\phi), \tag{5.1}$$

where $J(\Delta\phi)$ is the (di)jet function and $a_\circ$ represents the isotropic background level of the underlying event. The jet function in d+Au collision

was parameterized by the sum of two Gaussians, each of which represents the distribution of hadrons resulting from jet fragmentaion of the near- and away-side jet, respectively. Thus, the correlation function was fitted with the function

$$C(\Delta\phi) = a_\circ \left( 1 + \frac{\lambda_N}{\sqrt{2\pi}\sigma_N} e^{-\Delta\phi^2} + \frac{\lambda_A}{\sqrt{2\pi}\sigma_A} e^{-(\Delta\phi-\pi)^2} \right). \qquad (5.2)$$

Here, $\sigma_N$ ($\sigma_A$) is the Gaussian width of the near-side (away-side) peak. Similarly, $\lambda_N$ and $\lambda_A$ are the respective Gaussian amplitudes for the near-side and away-side peaks. The normalization is such, that $a_\circ \times (Gauss_N(\Delta\phi) + Gauss_A(\Delta\phi)) = J(\Delta\phi)$. The dotted line in Fig. 5.1 shows the fit to the data with Eq. 5.2. As can be seen, the fit function gives a fairly good representation of the data. One can also generate correlation functions for different charge combinations of the particles in the pair. Figure 5.2 shows such correlation functions for opposite charge pairs (left panel) and same charge pairs (right panel) for 0-20% most central d+Au collisions (red data points upper row) and a peripheral selection of 40-80% collisions (blue data points lower row). The near-side peak amplitude is very sensitive to the charge combination of the pair. This near side peak is significantly higher for opposite charge pair correlations and comparatively suppressed for same charge pair correlations. Such behavior is expected for jets from charge ordering along the fragmentation chain [A+97]. The fact that the away-side peak remains
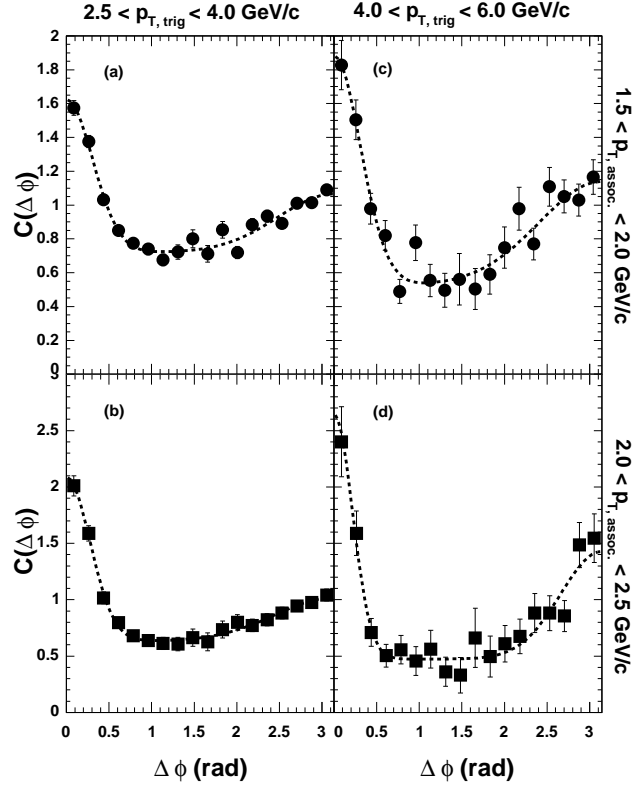
**Figure 5.1:** *Representative correlation functions for 0-80% d+Au collisions. Two $p_T$ windows for the trigger hadron and associated partner particle are explored. In panels (a,b) the trigger hadron is chosen between $2.5 < p_T < 4 GeV/c$ and in panels (c,d) the trigger $p_T$ selection is $4 < p_T < 6 GeV/c$. The associated $p_T$ window is either $1.5 < p_T < 2 GeV/c$ for panels (a) and (c) or $2 < p_T < 2.5 GeV/c$ for panels (b) and (d). The dotted lines are fits to the data with Eq. 5.2.*

unchanged when the charge selection is switched, merely reflects the independent fragmentation of the away-side jet. The correlation functions in Fig. 5.2 have also been fitted with Eq. 5.2 (smooth line in the figure) and the gaussian widths for near and away side peaks have been extracted (Table 5.1). Within statistical errors, they show no apparent dependence on the charge of the pair as expected from jet fragmentation. This result also suggests very little (if any) contributions from particle decays to the near-side peak at these $p_T$ selections. Further yield and width information is also extracted

**Table 5.1:** *Gaussian widths of jet peaks for same charge and opposite charge pair correlations in d+Au*

| | Centrality = 0-20% | |
|---|---|---|
| charge selection | near-side peak width | away-side peak width |
| opposite | $19.51 \pm 1.07°$ | $35.88 \pm 5.13°$ |
| same | $16.30 \pm 2.18°$ | $35.66 \pm 6.04°$ |
| | Centrality = 40-80% | |
| charge selection | near-side peak width | away-side peak width |
| opposite | $19.82 \pm 1.18°$ | $38.77 \pm 5.62°$ |
| same | $22.02 \pm 3.79°$ | $38.74 \pm 6.49°$ |

from the fits. These results are reported in the next chapter.
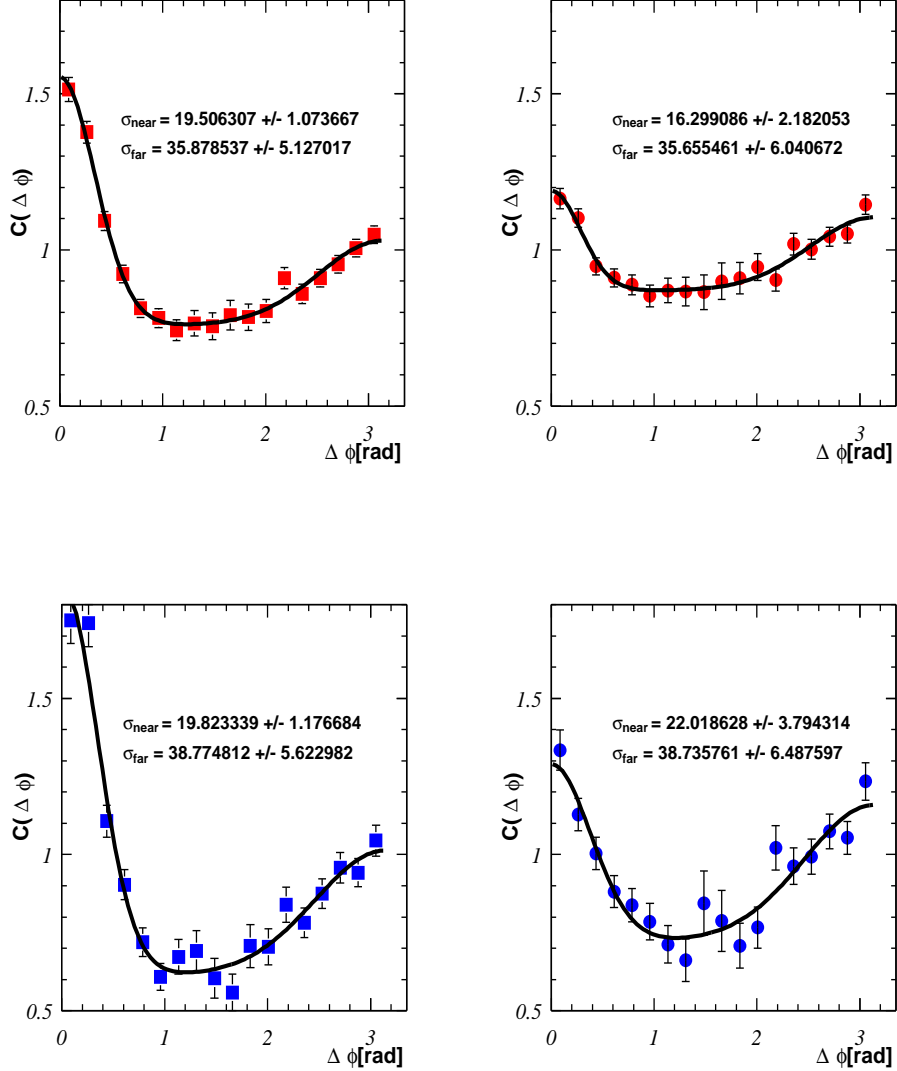
**Figure 5.2:** *d+Au charged hadron correlation functions for two centrality selections: 0-20% (upper row) and 40-80% (lower row). The trigger $p_T$ range is 2.5-4.0 GeV/c and the associated $p_T$ -selection is 1.0-2.5 GeV/c. The left row shows correlation functions constructed with opposite charge pairs and the right row shows correlation functions obtained for same charge pairs. The smooth line indicates a double gaussian fit to the data with Eq. 5.2*

## 5.2 Decomposition of Au+Au and Cu+Cu Correlation Functions

It was pointed out in chapter 3, that, in heavy ion collisions, pressure gradients can drive elliptic flow primarily toward the reaction plane. Therefore, the underlying event does not have to be isotropic (as is assumed for d+Au collisions), but can exhibit a harmonic modulation (cf. Eq. 3.8) with a given anisotropy amplitude $v_2$. This complication requires a reliable decomposition technique which can remove the flow correlations to reveal the resulting jet correlations. An important step for such a decomposition is the determination of $v_2$. In this section, the procedure to obtain reliable $v_2$ values through a reaction plane analysis is detailed. Subsequently, the technique for robust decomposition of the data to obtain reliable jet functions is demonstrated.

### 5.2.1 Reaction Plane and Reaction Plane Resolution

An important prerequisite for accurate determination of $v_2$ via the reaction plane method, is the requirement that the reaction plane itself is reconstructed free of non-flow contributions, ie. jet correlations in this case. This is needed to avoid any potential jet biases and thus an overestimate of $v_2$. A procedure that minimizes jet contributions to the reaction plane measurement is to require a large pseudorapidity gap between the reaction plane and

the particles correlated with it [A+05e]. In PHENIX, the BBC is separated from the central arm by 2-3 units in pseudorapidity. It is assumed, that this $\Delta\eta$ gap is sufficient to significantly suppress jet contributions to the $v_2$ measurement [A+03e].

The anisotropy amplitude $v_2$ is determined via a standard reaction plane analysis [P+98] in a three step procedure. In the first step, an estimated azimuth for the reaction plane ($\Psi_R$) is reconstructed by correlating the hits in the BBC photomultiplier tubes $n_{hit}$ with the azimuthal angle ($\phi$) of the tubes:

$$tan(2\Psi_{RP}) = \frac{\sum n_{hit}sin(2\phi)}{\sum n_{hit}cos(2\phi)} \tag{5.3}$$

In this step the reaction plane distribution was flattened where necessary, following the prescription outline in Ref. [P+98]. This flattening significantly reduces the possibility for errors in the measurement due to reaction plane bias. In the second step, the reaction plane resolution is estimated from the distribution of the difference between the reaction planes reconstructed from the BBCN and BBCS, respectively. For perfect reaction plane determination, both BBCN and BBCs would give identical results. In the final step, the azimuthal distribution of reaction products with respect to the reaction plane is generated and fitted with Eq. 3.8 to extract a raw anisotropy $p_2$. The corrected anisotropy coefficient $v_2$ is obtained by dividing this raw anisotropy by the reaction plane resolution.

Figure 5.3 shows the corrected reaction plane distributions as obtained
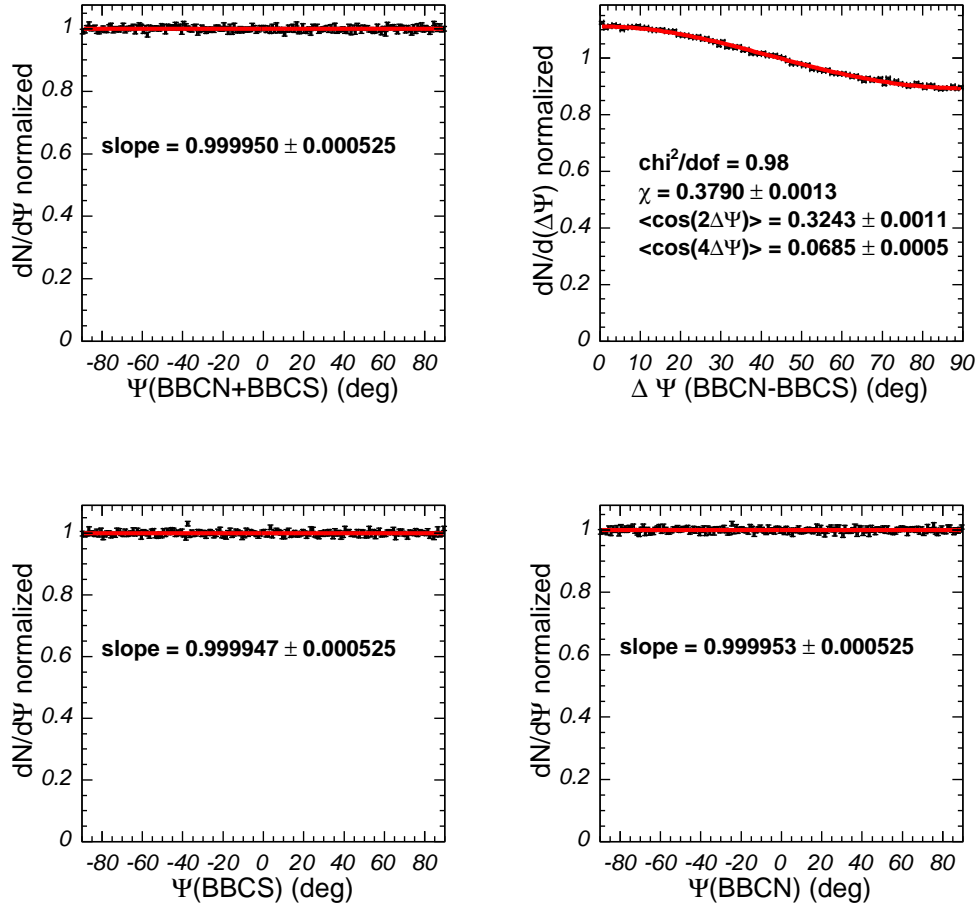
**Figure 5.3:** *Distribution of reaction plane angles ($\Psi_{BBC}$) for event planes determined in BBCN, BBCS and BBCN+BBCS. The reaction plane resolution is obtained from a fit to the $dN/d(\Psi_{BBCN} - \Psi_{BBCS})$ distribution.*

from BBCN, BBCS and both BBC's together. As can be seen from the straight line fits (solid lines in the figure), all three distributions are flat, as they should be. The distribution of the azimuthal difference between the reaction planes obtained from BBCN and BBCS separately is also shown in the figure. If only collective flow correlations contribute to the distribution of subevents, the distribution can be described with a harmonic function, as shown in Ref.[Oll95].

$$dN/d(\Psi_1 - \Psi_2) = \frac{e^{-x^2}}{2} \left( \frac{2}{\pi}(1 + \chi^2) + z(I_0(z) + L_0(z)) + \chi^2(I_1(z) + L_1(z))) \right)$$

(5.4)

Here, $z = \chi^2 cos(\Psi_1 - \Psi_2)$, $I_0$ and $I_1$ are Bessel functions, $L_0$ and $L_1$ are modified Struve functions. The reaction plane resolution can be inferred from the $\chi$ parameter, following the prescription of Ref.[Oll95]. A fit to the data with Eq.5.4 is shown in the upper right hand panel of Fig.5.3. It is noteworthy, that this equation assumes only harmonic contributions to the reaction plane, and any significant jet bias, if present, should be reflected in the $\chi^2/dof$ of the fit. In all cases, these fits yielded rather good $\chi^2/dof$ values of $\sim 1$.

Azimuthal anisotropy parameters ($v_2$), obtained for Run2 Au+Au collisions at $\sqrt{s_{NN}} = 200GeV$, have been plotted as a function of $N_{part}$ and $p_T$ (inset) in Fig. 5.4, for reference.
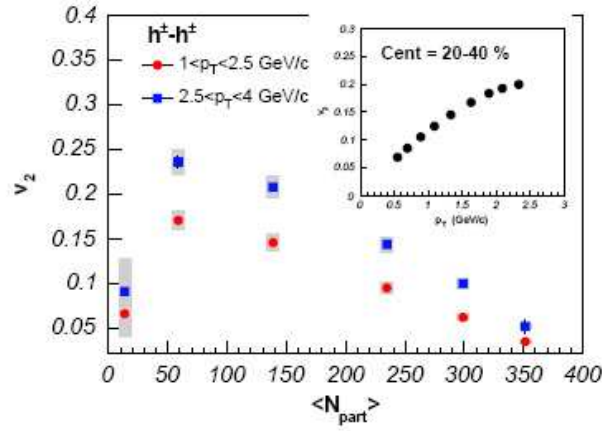
**Figure 5.4:** *Azimuthal anisotropy parameter $v_2$ as a function of $N_{part}$ and $p_T$ (inset) in Run2 Au+Au collisions at $\sqrt{s_{NN}} = 200 GeV$.*

## 5.2.2 Decomposition of the Correlation Functions via ZYAM and Harmonic Extinction

A detailed description of the ZYAM and Harmonic Extinction approaches for removing flow correlations from measured correlation functions was given in chapter 3. Briefly, for the ZYAM technique, the jet-function is extracted via subtraction of the harmonic term from the correlation function. The normalization is fixed by assuming that the jet-function has zero yield at minimum (ie. ZYAM). A demonstration of the ZYAM decomposition technique is given in Fig. 5.5. This figure displays a correlation function for 20-40% Cu+Cu collisions (black squares), where the trigger hadrons have been selected in the window $2.5 < p_T < 4$ GeV/c and associated hadrons between $1 < p_T < 2.5$

GeV/c. The solid red line represents the background modulated by the reaction plane $v_2$ and the dotted line indicates the background level, $a_o$. The jet function is obtained via ZYAM subtraction of the harmonic term from the correlation function and is shown as blue circles (referenced to $a_o$).
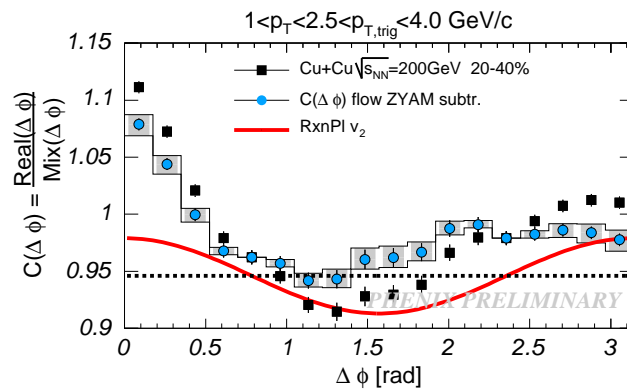


**Figure 5.5:** *Correlation function for 20-40% Cu+Cu collisions with trigger hadrons between $2.5 < p_T < 4$ GeV/c and associated hadrons between $1 < p_T < 2.5$ GeV/c (see text). The solid line represents the reaction plane $v_2$ and the dotted line indicates $a_o$. The jet function is obtained via subtraction of the harmonic term from the correlation function and is shown as blue circles (referenced to $a_o$).*

The second decomposition method, the harmonic extinction technique, sets $v_2$ in the correlation function to zero by requiring that trigger particles fall in a specific extinction window perpendicular to the reaction plane. In this technique, the resulting correlation function is equal to the jet-function

plus a flat background. If no strong reaction plane dependent jet-modification is present, or if the experimental reaction plane resolution is insufficient to reveal such a modification, the jet-functions extracted from the harmonic extinction technique and the ZYAM method should be comparable.

Figure 5.6 shows a representative selection of Au+Au correlation functions (black squares) for several centralities and particle species permutations as indicated. The background level, modulated by the reaction plane $v_2$, is indicated by the solid red line. Invoking the ZYAM condition yields the subtracted jet-pair distribution (blue data points) which is referenced to the background level, $a_\circ$. The gray boxes represent the systematic error on this distribution which is largely due to the uncertainty in $v_2$. The correlation function obtained with the extinction bite, is given by the red squares, and has been referenced to $a_\circ$ to facilitate shape comparisons with the ZYAM result. As can be seen from all four figures, the jet-functions obtained via both methodologies are in extremely good agreement.
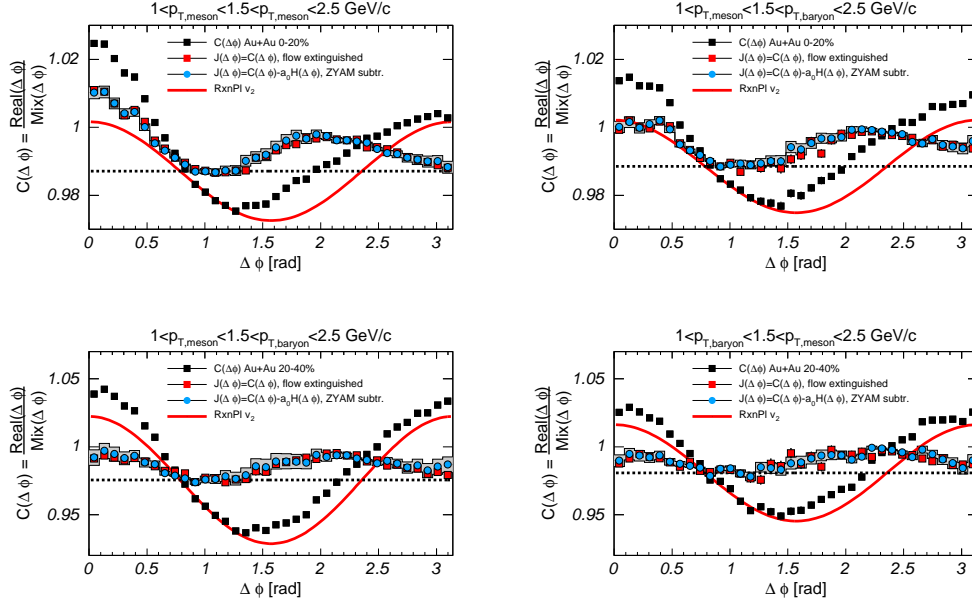
**Figure 5.6:** *Inclusive correlation functions (black squares), ZYAM subtracted jet functions (blue circles), and elliptic flow extinguished jet functions (red squares) for Au+Au collisions, as indicated (see text). The solid line represents the reaction plane $v_2$ and the dotted line indicates $a_o$. Upper left panel: Correlation Function for trigger mesons with $1.5 < p_T < 2.5$ GeV/c and associated mesons for $1 < p_T < 1.5$ GeV/c for 0-40% Au+Au collisions. Upper right panel: Correlation Function for trigger baryons with $1.5 < p_T < 2.5$ GeV/c and associated mesons for $1 < p_T < 1.5$ GeV/c for 0-40% Au+Au collisions. Lower left panel: Correlation Function for trigger baryons with $1.5 < p_T < 2.5$ GeV/c and associated mesons for $1 < p_T < 1.5$ GeV/c for 20-40% Au+Au collisions. Lower right panel: Correlation Function for trigger mesons with $1.5 < p_T < 2.5$ GeV/c and associated baryons for $1 < p_T < 1.5$ GeV/c for 20-40% Au+Au collisions.*

## 5.3   A Word on Systematic Errors

The analysis of jet pair distributions from correlation functions is a complicated multi-step process. Several sources of systematic uncertainties enter at the various stages. The systematic errors associated with obtaining robust correlation functions, pair cuts, etc. are relatively small and are estimated to be smaller than 2-3%. The largest contribution to the systematic error on the decomposition of the correlation function is due to elliptic flow subtraction. This error is dominated by the uncertainty on the reaction plane resolution. In Au+Au (Cu+Cu) collisions. it is 6% (14%), except for the most peripheral collisions, where a conservative 40% error has been estimated. The larger error for the smaller colliding system arises from the much larger reaction plane resolution. A systematic error is associated with the determination of the background level via the ZYAM procedure. This error is estimated by invoking the minimization algorithm with respect to different functional forms that each give a good representation of the data. It is generally very small and of the order of 2-3%. When extracting pair yields from the correlation functions an additional source of systematic error is the uncertainty on the single particle yields. This uncertainty is on average 10%.

# Chapter 6

# Results

Here, the results on jet-induced two particle correlations are described and discussed. The chapter is subdivided into four sections. Section 6.1 investigates jet mediated correlations in d+Au collisions and charts out basic trends and features of extracted jet properties such as yields and widths. Cold nuclear matter effects on these (di)jet signals are searched for by studying the centrality dependence of the jet observables. The results in this section are used as a baseline measurement for jet studies in heavy ion collisions. Such studies in Au+Au collisions are presented in section 6.2 for charged hadron correlations as a function of centrality. More matter with higher energy density is produced in central Au+Au collisions, compared to a peripheral collision sample. Therefore, these investigations provide a powerful tool to probe jet-modification by the hot and dense collision medium. A more differential measurement that specifically targets the particle species dependence

of jet-modification is reported in section 6.3. Finally, in section 6.4 it is suggested that the system size dependence of jet-modification can be utilized as a complementary tool to probe for path-length dependent jet alteration. An initial attempt in that direction is made via a systematic comparison of jet pair distributions in Cu+Cu and Au+Au collisions.

## 6.1 Jet-induced Di-Hadron Correlations in d+Au Collisions

Deuteron + gold collisions provide an important baseline measurement for the heavy ion program. The operational strategy, generally employed at RHIC, is that in heavy ion collisions both, hot nuclear matter effects, and "trivial" effects, already present in cold nuclear matter, can manifest themselves in the data. In d+Au collisions, no hot final state medium is created. Therefore this system is ideally suited to study initial state effects and cold nuclear matter influences on the respective observables. Thus d+Au collisions serve as a "null" experiment that one can compare the heavy ion data against. Specifically for the case of jet-modification measurements, any signal observed in Au+Au and Cu+Cu collisions over and above that of the d+Au data, can be attributed to the high energy density medium expected to be created in central and semi-central heavy ion collisions.

Two long standing observations of cold nuclear matter effects are especially important with regard to jet measurements.

The cross section for high $p_T$ particle production in collisions with nuclear targets is known to increase faster than the number of binary collisions [C$^+$75]. At lower beam energies, this so called "Cronin" enhancement of the yields has been observed to be proportional to the atomic mass of the target to some power ($A^\alpha$) [C$^+$75, A$^+$79b, S$^+$92].

A clear atomic mass dependence of the (di)jet acoplanarity has also been reported in particle collisions with nuclei at these lower energies [S$^+$90, C$^+$94, N$^+$94]. The common explanation for this (di)jet broadening is in terms of additional transverse momentum transfer to the acoplanarity momentum vector $\vec{k_T}$ (cf. section 1.2). Such a $k_T$ increase can arise due to multiple scattering of the hard-scattered partons in the nucleus [Acc02]. This picture is corroborated by the observation of the E683 collaboration, that the momentum transfer is approximately proportional to the path-length $L$ of the parton in the cold nuclear medium $< k_T^2 > \propto A^{1/3} \approx L$ [N$^+$94]. The $p_T$ increase of the partons in the multiple scattering picture, should also result in a yield increase for energetic particles, consistent with "Cronin" enhancement.

Recent results from RHIC, at much higher beam energies and at midrapidity, have shown that the yield of intermediate $p_T$ particles in d+Au collisions (at $\sqrt{s_{NN}} = 200 GeV$) is enhanced compared to the yield in p+p collisions (at the same energy), scaled by the number of binary collisions [A$^+$03f].

The data are reasonably well explained by multiple scattering models [QV04]. However, a recent conjecture by Hwa and Yang, that invokes the yield enhancement via the recombination of hard and soft partons [HY04] can also describe the data. This latter mechanism does not predict (di)jet broadening.

At present, a consistent explanation of all available data on "Cronin" enhancement and (di)jet broadening is still elusive. It is not even clear, if the observed cross-section increase for the singles yield is necessarily connected to the same mechanisms that cause (di)jet broadening. Since sizable "Cronin" enhancement is still observed in d+Au collisions at $\sqrt{s_{NN}} = 200 GeV$, it will be interesting to see whether (di)jet broadening also persists to such high beam energies. In d+Au collisions the mass number is obviously fixed, however, one can gain an additional measure of control over how much nucleus the hard scattered partons see, by varying the centrality of the collision. Centrality dependent jet-correlation measurements can thus serve as a complementary tool to distinguish between different model scenarios of "Cronin" enhancement and (di)jet broadening at RHIC energies.  Jet modification studies in d+Au collisions at RHIC are therefore important in their own right.

The remainder of this section is organized as follows. First, a detailed set of jet properties is given for centrality integrated results (for 0-80% of the geometrical cross-section). The main goal, here, is to carefully investigate if

the observed correlation structures attributed to (di)jets do indeed behave according to expectations from jet physics. Furthermore, the reported results serve as baseline measurements for the jet correlation studies in Au+Au and Cu+Cu collisions. Second, the centrality dependence of extracted jet properties is examined with an eye toward possible (di)jet broadening and yield enhancement similar to what has been observed at lower beam energies [C$^+$75, A$^+$79b, S$^+$92, S$^+$90, C$^+$94, N$^+$94].

## 6.1.1 Centrality Integrated Results

In chapter 3 it was explained, that the ratio of the area under the jet correlated part of the correlation function to the total area of the correlation function can be related to the fraction of jet correlated particle pairs. This "jet pair fraction" has been extracted from double gaussian fits (with Eq. 5.2) to 0-80% most central d+Au correlation functions. The jet pair fractions for correlations with a trigger particle selected in a transverse momentum interval of $3 < p_T < 5 GeV/c$ and different associated particle $p_T$ selections (as indicated) are reported in Fig. 6.1. The results for the near-side gaussian peak are depicted as filled circles, while the away-side results are shown as open circles. The jet pair fraction for near- and away-side jets rises steadily as a function of associated particle $p_T$. Jet fragmentation is expected to play

an increasingly important role in particle production at high transverse momentum and the $p_T$ trend of the jet pair fraction in Fig. 6.1 is consistent with this expectation. The somewhat slower rise of the away-side jet pair fraction, compared to the near side, mainly reflects the limited $\eta$ acceptance of the PHENIX detector. The jet pair fractions can be converted into pairs per
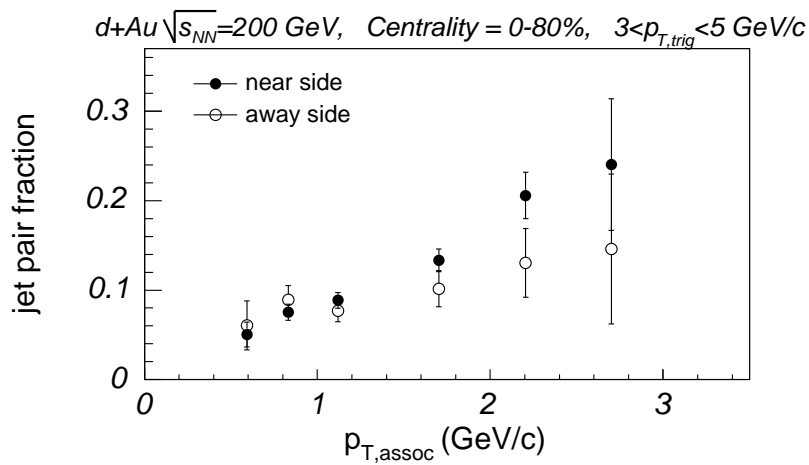


**Figure 6.1:** *Jet pair fractions for correlations with a trigger particle selected in a transverse momentum interval of $3 < p_T < 5 GeV/c$ and different associated particle $p_T$ selections for near-side (filled symbols) and away-side (open symbols) correlations (see text).*

trigger (or conditional) yields, following the prescriptions of chapter 3. Given a trigger particle, the conditional yield can be interpreted as the probability of finding jet correlated associated partner particles. Conditional yield values as a function of associated particle $p_T$ are depicted in Fig. 6.2. The red

circles indicate results for a trigger particle between $2.5 < p_{T,trig} < 4 GeV/c$
and the blue squares show the corresponding results for a trigger $p_T$ selec-
tion of $4 < p_{T,trig} < 6 GeV/c$. The results for the higher trigger $p_T$ have
been multiplied by 10 for display purposes. Filled and open symbols denote
the near-side and away-side yields, respectively. Several observations can be
made from Fig. 6.2. First, the associated yield for the higher trigger $p_T$ se-
lection is systematically larger than for the lower trigger $p_T$. This mild yield
difference is consistent with the notion, that higher momentum particles have
more jet-correlated partner particles than their low $p_T$ analogs. Second, the
yield of jet-associated particles falls approximately exponentially with part-
ner $p_T$. This is indicative of the fact that most jet fragments are produced at
low transverse momentum. However, there is a mild difference between the
rate of the exponential drop for the two different trigger $p_T$ selections, show-
ing that there is some trigger $p_T$ dependence in the shape of the dN/d$p_{T,asspc}$
distributions.

The first investigation of jets via assorted azimuthal correlations was
undertaken at the ISR in the 1970's. There, the variable $x_E$ was introduced
and defined as follows:

$$x_E = -\frac{\vec{p_T}_{trig} \cdot \vec{p_T}_{assoc}}{p_{T,trig}^2} = -\frac{p_{T,assoc}}{p_{T,trig}} cos(\Delta\phi) \qquad (6.1)$$
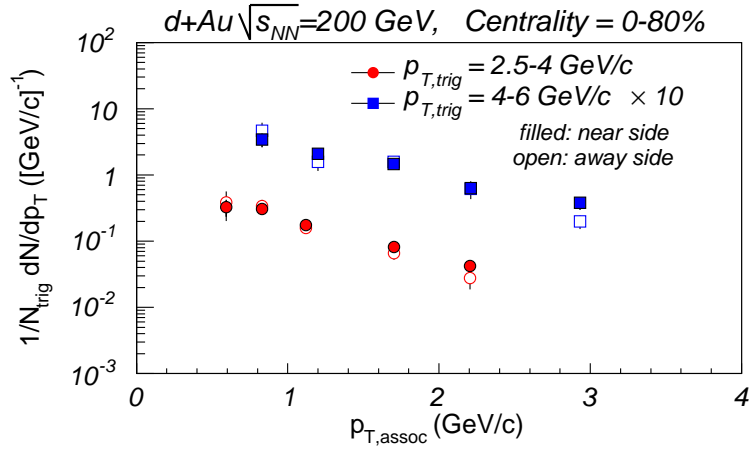
**Figure 6.2:** *Conditional yield as a function of associated particle $p_T$. The red circles indicate results for a trigger particle between $2.5 < p_{T,trig} < 4 GeV/c$ and the blue squares show the corresponding results for a trigger $p_T$ selection of $4 < p_{T,trig} < 6 GeV/c$. The results for the higher trigger $p_T$ have been multiplied by 10 for display purposes. Filled and open symbols denote the near-side and away-side yields, respectively.*

One of the important findings was the observation that the away-side conditional yield distributions in $x_E$ scale independent of the transverse momentum of the trigger particle [K$^+$79, A$^+$79a]. In Fig. 6.3, $x_E$ distributions have been obtained for the away-side conditional yields of Fig. 6.2. The red circles show again the results for $2.5 < p_{T,trig} < 4 GeV/c$ and the blue squares show the yields for $4 < p_{T,trig} < 6 GeV/c$. The trigger particle dependence in the conditional yield distributions, evident when plotted versus $p_{T,assoc}$, is not
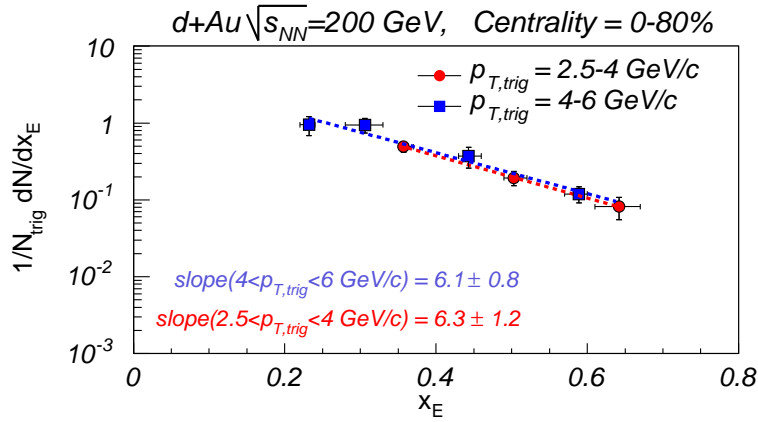
**Figure 6.3:** *Away-side $x_E$ distributions for two trigger $p_T$ selections as indicated.*

observed when the yields are graphed against the $x_E$ variable, *ie.* the distributions scale. The discovery of $x_E$ scaling at the ISR led people to believe that the $x_E$ distribution on the away-side could be related to the fragmentation function. This argument was supported by the assumption, that at high enough trigger $p_T$, $x_E \approx z_{assoc}/z_{trig}$, where $z = p/p_{jet}$ is the fraction of the total jet momentum, that a given jet fragment carries. Following this reasoning, the CCOR collaboration extracted inverse slope parameters from exponential fits to their $x_E$ distributions [A$^+$79a]. These inverse slopes were on average 5.3. Exponential fits to the $x_E$ distributions in Fig. 6.3 yield inverse slopes of $6.1 \pm 0.8$ and $6.3 \pm 1.2$ for $4 < p_{T,trig} < 6 GeV/c$ and $2.5 < p_{T,trig} < 4 GeV/c$, respectively. These values are somewhat larger than what has been measured in p+p collisions at the ISR. In recent work [Tan06], M. J. Tannenbaum has

presented analytic calculations, showing that while the $x_E$ distributions scale, there is no straightforward way to relate their shape to the shape of the fragmentation function. More precisely, he demonstrates that for the case of an exponential fragmentation function $D(z) = Be^{-bz}$, the $x_E$ distribution becomes an incomplete gamma function and only relates to the fragmentation function via the ratio $B/b$. Hence, widely different fragmentation functions can in principle result in very similarly shaped $x_E$ distributions. It is still reassuring to see, though, that the $x_E$ distributions in d+Au collisions at RHIC scale as expected for jet physics.

Besides conditional yield information, one can also extract topological information from a jet correlation study. Gaussian widths (in $\Delta\phi$) for away-side peaks (open circles) and near-side peaks (filled circles) are given in Fig. 6.4. The results have been obtained for various bins in associated particle $p_T$ and a trigger $p_T$ selection of $3 < p_{T,trig} < 5 GeV/c$. The away-side widths are consistently larger than the near-side widths. This can be easily understood, since the near-side angular widths only reflect the fragmentation process of the near-side jet. The away-side widths, however, are determined by a combination of the independent fragmentation of the near- and away-side jet, as well as the acoplanarity ($k_T$) of the (di)jet system. The narrowing of the near-side and away-side widths with associated particle momentum reflects the fact that more energetic jet fragments carry a larger fraction of the parton momentum and thus appear closer to the jet axis.
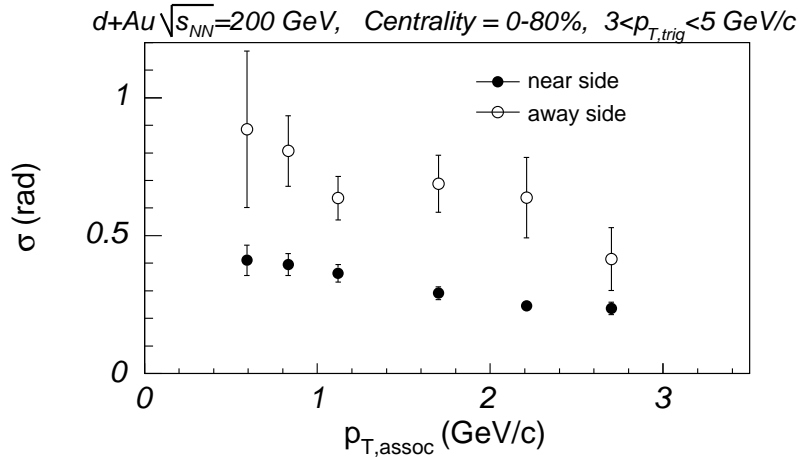
**Figure 6.4:** *Gaussian widths as a function of associated partner $p_T$. The results of away-side peaks (open circles) and near-side peaks (filled circles) are for a trigger $p_T$ selection of $3 < p_{T,trig} < 5 GeV/c$.*

Already when the author of this thesis was born, strategies were developed to relate the jet correlation topology to jet fragmentation variables [FFF77]. Most recently, this effort was revived for the case of azimuthal correlations at RHIC [Rak04]. In Ref. [Rak04] it was argued, that the jet fragmentation transverse momentum $j_T$ (the component of the particle transverse momentum, perpendicular to the jet transverse momentum) can be extracted from the width of the near-side correlation peak. The projection of $j_T$ into the transverse plane is denoted $j_{T,y}$ and can be approximated from the near-side width $\sigma_N$ and the average trigger and associated particle $p_T$, $< p_{T,trig} >$ and

$< p_{T,assoc} >$, respectively [A$^+$05d].

$$\sqrt{< j_{T,y}^2 >} \approx \sigma_N \frac{< p_{T,trig} >< p_{T,assoc} >}{\sqrt{< p_{T,trig} >^2 + < p_{T,assoc} >^2}} \quad (6.2)$$

Assuming a gaussian near side jet peak, $j_{T,y}$ and $j_T$ have a simple relationship ($\sqrt{< j_T^2 >} = \sqrt{2}\sqrt{< j_{T,y}^2 >}$).

Values for $\sqrt{< j_{T,y}^2 >}$ and $\sqrt{< j_T^2 >}$ are given in Fig. 6.5. These results have been obtained for an average trigger transverse momentum of $< p_T > \approx 3.5 GeV/c$ and are graphed as a function of the associated particle $p_T$. The error bars indicate statistical and systematic errors. The latter are dominated by the uncertainty of the approximations for Eq. 6.2 and are of the order of 5% and independent of $p_T$. The $\sqrt{< j_T^2 >}$ rises as a function of $p_{T,assoc}$ and seem
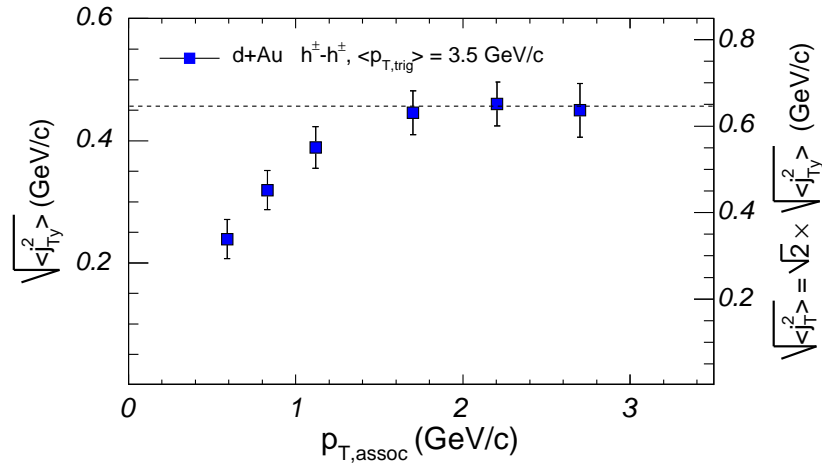


**Figure 6.5:** *Values for $\sqrt{< j_{T,y}^2 >}$ and $\sqrt{< j_T^2 >}$ as a function of associated partner $p_T$ (see text).*

to reach a plateau value above $p_T = 2 GeV/c$. The rising trend of $\sqrt{< j_T^2 >}$

for low $p_{T,assoc}$ reflects a kinematic cutoff (known as Seagull effect, resulting from the requirement that $j_{T,y} < p_T$. A combined fit to these data points and results from other complementary PHENIX correlation analyses above $p_T = 2GeV/c$ yields a value of $\sqrt{<j_T^2>} = 0.64 \pm 0.02(stat) \pm 0.04(sys)GeV/c$ for d+Au collisions [A$^+$05d]. This number is in good general agreement with measurements of $\sqrt{<j_T^2>}$ in p+p collisions at the much lower ISR energies [A$^+$80].

In short, the centrality integrated jet properties, presented here, behave very much as expected for jet-induced correlations, therefore strongly supporting the operational assumption that the double peak structures in the two particle correlation can be attributed to the fragmentation of (di)jets. Furthermore, these results provide baseline cold nuclear matter comparisons for the heavy ion data (which will be presented in later sections of this chapter).

## 6.1.2 Centrality Dependence of Jet Properties

Multiple scattering models that aim to describe the "Cronin" enhancement at RHIC, also predict an increase in the away-side jet width with increasing collision centrality [Acc02, QV04, BPLF04]. Figure 6.6 depicts gaussian near-side (filled circles) and away-side (open circles) widths for three centrality selections and $1 < p_{T,assoc} < 2.5 < p_{T,trig} < 4GeV/c$. The widths are

plotted as a function of the number of binary collisions ($N_{coll}$) for each centrality class. Neither the away-side, nor the near-side widths appear to show much broadening. This observation is in contrast to earlier measurements at lower energies, that found strong (di)jet broadening [S$^+$90, C$^+$94, N$^+$94] and possibly suggests a change in mechanism for the "Cronin" effect at these high energies. Hwa and Yang recently proposed that recombination of hard and
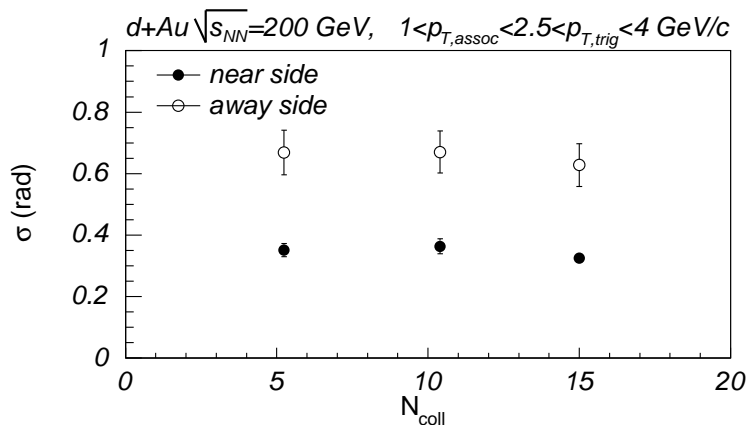


**Figure 6.6:** *Gaussian near-side (filled circles) and away-side (open circles) widths for three centrality selections and $1 < p_{T,assoc} < 2.5 < p_{T,trig} < 4 GeV/c$.*

soft partons could lead to the observed "Cronin" enhancement of the singles yields [HY04]. Their model does not give rise to any (di)jet broadening. However, they initially predicted a large increase in the conditional yields (factor two from peripheral to central collisions) [HY04]. This recombination model has subsequently been refined and the latest calculations indicate

an $\approx 30\%$ increase, instead [HT]. Figure 6.7 depicts conditional yields as a function of $N_{coll}$ for the partner and trigger transverse momentum selection of $1 < p_{T,assoc} < 2.5 < p_{T,trig} < 4GeV/c$. No huge yield increase is observed. However, the statistical uncertainties do not rule out a 20-30% yield change from peripheral to central d+Au collisions.
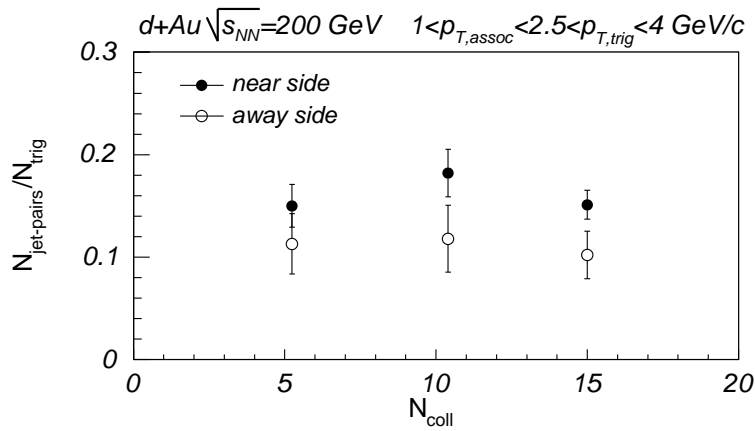


**Figure 6.7:** *Near-side (filled circles) and away-side (open circles) conditional yields for three centrality selections and $1 < p_{T,assoc} < 2.5 < p_{T,trig} < 4GeV/c$.*

In summary, although strong "Cronin" enhancement has been reported for the inclusive singles yields in d+Au collisions at $\sqrt{s_{NN}} = 200GeV$ [A$^+$03f], the two particle correlation analysis of the same data does not appear to show any evidence for significant (di)jet broadening. Taken together, these observations differ from results obtained for lower energy particle-nucleus collisions, where "Cronin" enhancement and (di)jet broadening have been

observed and attributed to multiple scattering of the parton in the nuclear target [C$^+$75, A$^+$79b, S$^+$92, S$^+$90, C$^+$94, N$^+$94]. A suggested recombination scenario can explain the yield enhancement of intermediate $p_T$ particles in d+Au collisions at $\sqrt{s_{NN}} = 200 GeV$, without invoking simultaneous (di)jet broadening. A predicted 30% increase in the conditional jet yields from peripheral to central d+Au collisions by this model, cannot be ruled out by the data.

## 6.2 Jet-Modification for Charged Hadrons in Au+Au Collisions

Jet studies via multiparticle azimuthal correlations are a powerful tool to probe the high energy density partonic matter believed to be created in heavy ion collisions at RHIC. As a hard-scattered parton traverses the hot QCD matter, it can lose energy before fragmenting into hadrons [Bjo82, App86]. This energy loss is expected to be sensitive to several properties of the medium, such as the gluon density, formation time and path length traversed [Bjo82, App86, Bla86, WG92]. It is believed, that this process can result in significant modification to jet topologies and yields, therefore enabling jets to be utilized as tomographic short wavelength probes of the fireball.

Azimuthal correlation studies allow for a statistical separation of the jet-signal from the underlying event (see chapter 3). They give simultaneous access to both shape and yield information from jets. Two particle correlations at high transverse momentum have shown, that the away-side jet is suppressed in central and semi-central Au+Au collisions [A+03c], thus giving direct evidence for jet energy-loss.

A question of great current interest is how the lost energy is redistributed in the medium and what consequences result from the medium's response to the jets. An active discussion on how jets can couple to the surrounding high

energy density matter is currently ongoing. Several recent theoretical efforts have stirred particular excitement. It has been proposed, that shower quarks can recombine with soft quarks from the medium, thereby changing both shape and yield of the jets [G$^+$03, HW04]. Another theoretical approach predicts that jet-modification can be sensitive to the jets inclination angle with respect to the flow field [A$^+$04c]. Perhaps one of the most intriguing proposals is that a hard scattered parton, traversing a partonic fluid with essentially the speed of light, can induce "conical flow" or "mach shocks" not unlike supersonic booms [Sto05, CS$^+$04, RM05, RR06]. In the simplest case of a static medium, the angle of the jet induced mach cone ($\theta_M$) only depends on the speed of sound ($c_S$) in the medium, i.e. $cos(\theta_M) = c_s/c$ [CS$^+$04], where $c$ is the speed of light. The experimental verification of conical flow could thus provide a reliable estimate for the speed of sound in the high energy density medium. Similar cone structures have been hypothesized to arise from Cherenkov gluon radiation [MW05, KMW05]. In this latter case, the refractive index of the medium should be the controlling parameter [KMW05]. All of these mechanistic conjectures, though, require significant coupling of the jets to a strongly interacting high energy density medium.

In this section, two particle azimuthal correlations of a high $p_T$ trigger particle ($2.5 < p_{T,trig} < 4 GeV/c$) with an associated particle at intermediate $p_T$ ($1 < p_{T,assoc} < 2.5 GeV/c$) are utilized to probe for jet interactions with the medium. The centrality dependence of these correlations is believed to

provide a large lever arm for jet modification. In peripheral collisions, very little to no hot and dense matter is thought to be produced. For gradually more central selections, as the overlap between the two nuclei increases, larger amounts of matter with higher energy density are created [A$^+$05c]. Therefore, jet modification should become increasingly prominent for semi-central and central collisions. Findings are compared to results from d+Au collisions, where no hot and dense final state medium is expected to be formed. Finally, a comparison of the data to a theoretical model of mach shocks in a strongly interacting, expanding medium will be discussed.

Figure 6.8 depicts ZYAM subtracted (see chapter 3) distributions of jet pairs (per trigger particle) for six centrality selections, as indicated. The distributions have been normalized to $1/N_{trig}dN/d\Delta\phi$ and are folded into the region $\Delta\phi = 0 - \pi$. The ZYAM method determines a minimum ($\Delta\phi_{min}$) in the distribution, based on a minimization procedure with respect to a functional fit of the data (see section 3.3.1). The minima (in rad) for the depicted jet functions are $\Delta\phi_{min} = 0.94, 0.96, 0.98, 0.91, 0.86, 1.06$ for the respective centralities of 0-5%, 5-10%, 10-20%, 20-40%, 40-60% and 60-90% of the geometrical cross section. The uncertainty on these minima related to the ZYAM assumption is indicated by the hatched area in the figure. Hereafter, the part of the distribution from $\Delta\phi = 0 - \Delta\phi_{min}$ is called the near-side, and the region from $\Delta\phi = \Delta\phi_{min} - \pi$ is denoted away-side. The jet pair distribution in the most peripheral sample (60-90%, Fig. 6.8 (f)),

evidences a clear near-side peak at $\Delta\phi = 0$ and a broader and smaller away-side peak at $\Delta\phi = \pi$. This shape compares well to the jet functions measured in d+Au collisions (cf. Fig. 5.1) and is reminiscent of (di)jet mediated pair correlations.

The jet pair distribution in panel (e), for 40-60%, does not show much change for the near-side jet. However, the away-side jet is clearly broadened compared to the jet function in the peripheral bin. Turning to even more central collisions, the shape of the near-side peak still appears to be unchanged; the near-side conditional yield, however, rises as a function of centrality, hinting at some jet modification. A strong centrality dependence in both yield and shape can be observed for the away-side jet peak. This peak is significantly broadened in the semi-central and central samples and possibly even evidences a local minimum at $\Delta\phi = \pi$. To give the reader a quantitative feel for how the systematic uncertainties in the $v_2$ subtraction influence the shape of the jet-pair distributions, the dashed (solid) line represents the jet function that would result if one subtracted an azimuthal anisotropy amplitude $(v_{2,assoc} \times v_{2,trig})$ which was lower (larger) by one unit of the systematic error. For reference, the jet pair distributions obtained by subtracting a $v_{2,assoc} \times v_{2,trig}$ product lowered by twice the systematic error are given as dotted lines in the figure. It is interesting to note, that the local minima at $\Delta\phi = \pi$ depend strongly on the magnitude of the $v_2$ subtraction, but the observation of broad and plateauing away-side peaks for the central

and semi-central bins remains robust.

The shape of the away-side peaks in central and semi-central collisions seems inconsistent with purely gaussian (di)jet broadening. However, these shapes appear compatible with recent conjectures of jet modification in a strongly interacting QGP [G$^+$03, HW04, A$^+$04c, Sto05, CS$^+$04, RM05, RR06], including the possibility of jet-induced mach cones. This latter prediction is particularly interesting. If it could be confirmed, it might allow to constrain the speed of sound in the nuclear collision medium. One of the main objectives of nuclear reaction studies at RHIC is the exploration of the equation of state (EOS) for QCD matter. The equation of state links the energy density ($\epsilon$) and the pressure ($p$). The most simple equation of state is given by $\epsilon = 1/c_s^2 p$, where $c_s^2$ is the speed of sound in the medium squared. Reliable experimental estimates of $c_s$ can therefore serve to constrain the EOS.

Inspired by this result, Renk and Ruppert have modeled the propagation of sound waves in expanding central collisions [RR06]. Their approach allows for a realistic acoplanarity of the (di)jet system, that has been tuned to reproduce the peripheral Au+Au and minimum bias d+Au correlations. Figure 6.9 has been taken from Ref. [RR06] and depicts a comparison of different model predictions to the most central (0-5%) away-side correlation from Fig. 6.8. The data points represent the jet function for 0-5% most central collisions from this analysis. Note, that the convention for $\Delta\phi$ has changed. The peak, appearing at $\Delta\phi = \pi$ in Fig. 6.8 (a), now is plotted at $\Delta\phi = 0$, *i.e.*

the jet function has been flipped. Only the away-side region of the jet pair distribution is shown and compared to three curves. The dash-dotted line represents the jet pair distribution, that the model predicts if the jet deposits 50% of its energy into the medium. Clearly, this does not result in enough yield at $\Delta\phi \approx 60°$ to reproduce the data. However, the model shows remarkable aggrement in shape and yield with the experimental jet function, if the jet is allowed to lose almost all its energy (90%) in the medium (solid curve). The dashed line depicts the predicted conditional yield distribution for an ideal QGP value of the speed of sound $c_s \approx 1/\sqrt{3}$. This distribution peaks at too low values of $\Delta\phi$ to reproduce the data, therefore indicating that much lower speed of sound values than for the ideal QGP need to be invoked. It is amusing, that a recent estimate of the speed of sound from elliptic flow data also seems to yield such low values [IT06]. It should be noted, that the model from Ref. [RR06] is certainly not the only way to describe the data and that it is not possible to distinguish between the aforementioned jet modification models purely on the basis of the charged hadron jet pair correlations, shown in this section. However, these jet pair distributions provide first evidence for significant coupling of jets to a strongly interacting colored medium and the conjecture of jet induced mach shocks cannot be ruled out, at present.

To further investigate (di)jet modification on a more quantitative level, the integrated per trigger yields have been obtained for the near-and away-side regions of the jet pair distribution along with the root-mean-square

widths. These values are plotted versus the average number of participants ($N_{part}$) for each centrality sample in Fig. 6.10 (a) and (b), respectively. Results for the near-side peaks from Au+Au are denoted by filled circles and their analogs for the away-side are depicted as open circles. These results are to be compared to the same quantities from minimum bias d+Au collisions (shown as filled and open squares). Turning first to the widths, good overall agreement between the most peripheral Au+Au results and the d+Au data is observed for near- and away-side peaks. If one traces the centrality evolution of these widths one observes little to no change for the near-side within errors. Although statistical and systematic errors (indicated by colored bands) are sizable, the away-side widths for all but the most peripheral bin are significantly enlarged, consistent with strong medium induced (di)jet broadening. The yield of jet associated partner particles per trigger particle for away-side jets seems to rise from peripheral to mid-central collisions, and possibly decreases again for the 0-5% most central sample. This is a strong evidence for centrality dependent yield modification of the away-side jets. The near-side conditional yields exhibit a similar but less pronounced trend with centrality, which might be indicative of some (albeit small) yield modification to the near-side jets. Taken together, these results differ from earlier observations of jet-induced two particle correlations at much higher transverse momentum [A+03c]. These latter measurements show an away-side peak that is reduced in yield, but unmodified in shape. A simple "surface bias" picture [DLP05]

can seemingly reconcile the two measurements. This picture (illustrated in Fig. 6.11) relies on the idea that the matter is very opaque to jets. In this case, triggering on high $p_T$ particle pairs would be tantamount to selecting (di)jets with tangential orientation relative to the fireball (cf. Fig. 6.11 (b)). For such a picture, no strong away-side modification is expected. However, triggering on a medium $p_T$ particle could preferentially select weakly modified or unmodified jets, i.e. near side jets close to the surface of the fireball (cf. Fig. 6.11 (a)). By contrast, for this latter condition, the recoiling jet would have to traverse almost the whole fireball resulting in strong away-side jet modification.

In summary, jet pair distributions for intermediate $p_T$ particles have been examined as a function of collision centrality in Au+Au collisions at $\sqrt{s_{NN}} = 200 GeV$. For semi-central and central collisions, these distributions are strongly modified in both yield and shape. As the centrality is increased, the number of jet-associated partner particles per trigger particle rises. The away-side jet peak is significantly broadened for all but the most peripheral collisions and the shape seems to suggest the existence of a local minimum at $\Delta\phi = \pi$. Taken together, these results clearly indicate strong modification of the away-side jet in the intermediate $p_T$ region in Au+Au collisions at $\sqrt{s_{NN}} = 200 GeV$. The modification pattern is compatible with recent predictions of jet interactions with a strongly coupled medium [G$^+$03, HW04, A$^+$04c, Sto05, CS$^+$04, RM05, RR06].
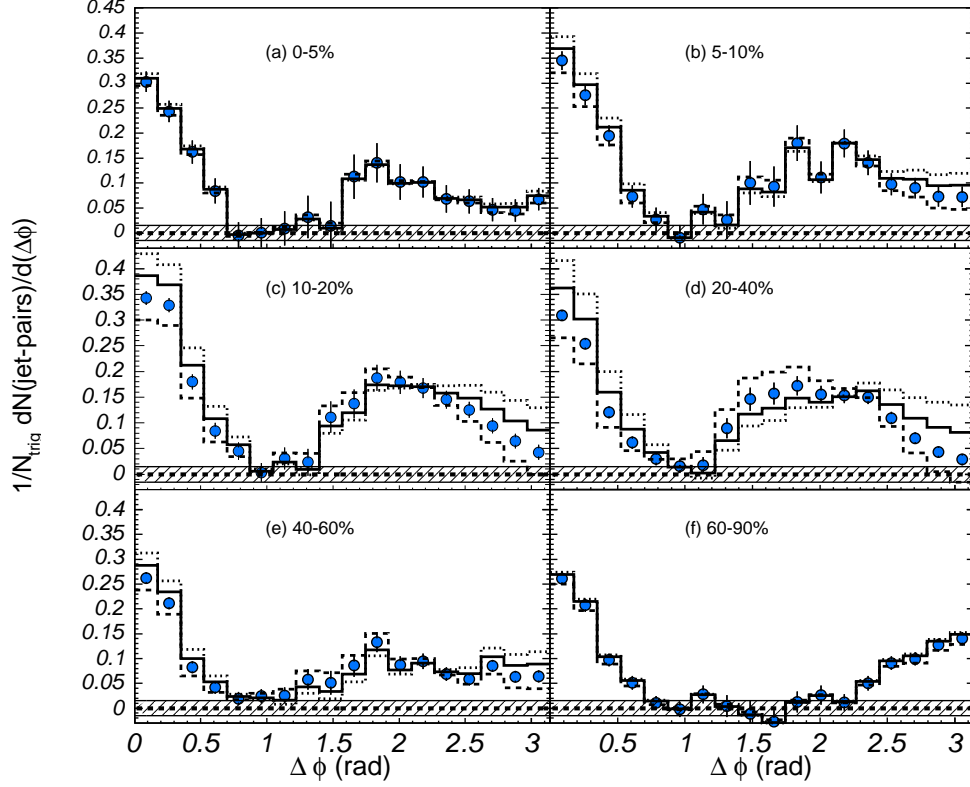
**Figure 6.8:** *Jet pairs (per trigger particle) for six centrality selections, as indicated. The distributions have been normalized to per trigger yields $(1/N_{trig}dN/d\Delta\phi)$ and are folded into the region $\Delta\phi = 0 - \pi$. The dashed (solid) lines represents the jet functions that would result if one subtracted an azimuthal anisotropy amplitude $(v_{2,assoc} \times v_{2,trig})$ which was lower (larger) by one unit of the systematic error. For reference, the jet pair distributions obtained by subtracting a $v_{2,assoc} \times v_{2,trig}$ product lowered by twice the systematic error are given as dotted lines.*
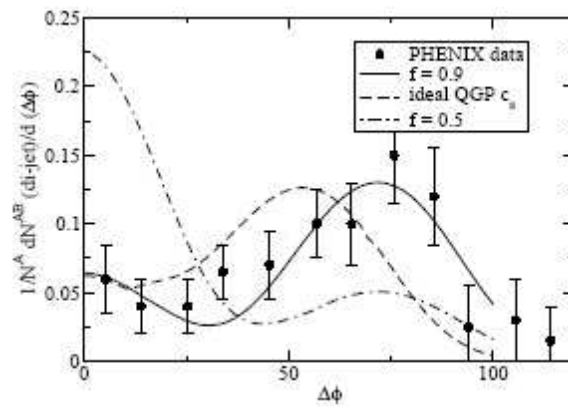
**Figure 6.9:** *The data points represent the jet function for 0-5% most central collisions from this analysis. The solid, dashed and dash-dotted lines represent model calculations. Figure reproduced from Ref.[RR06].*
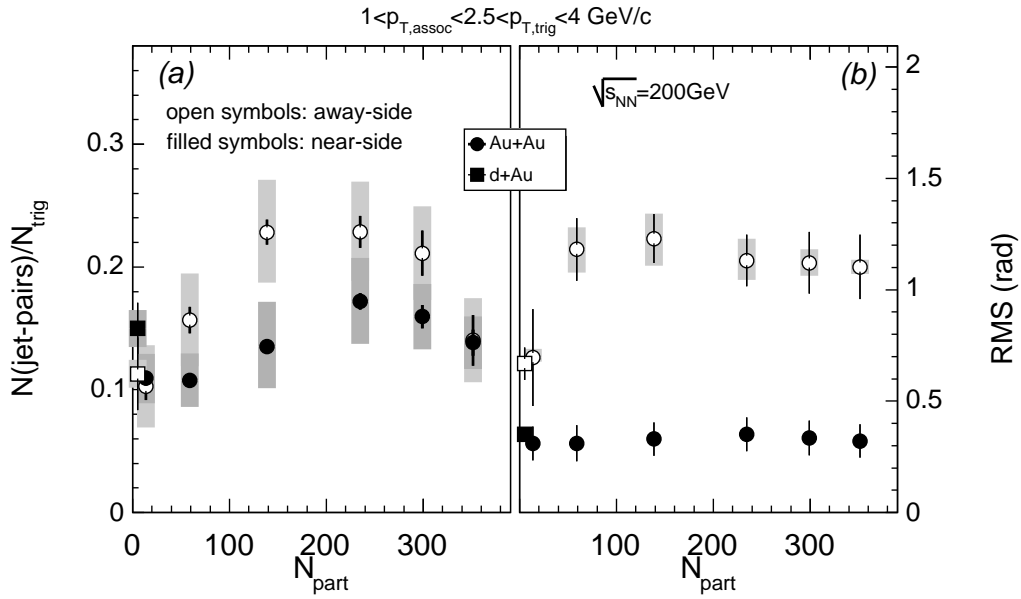
**Figure 6.10:** *Summary Jet yields (a) and RMS widths (b) as a function of $N_{part}$. Au+Au results for the near-side peaks are denoted by filled circles and their analogs for the away-side are depicted as open circles. These results are to be compared to the same quantities from minimum bias d+Au collisions (shown as filled and open squares).*
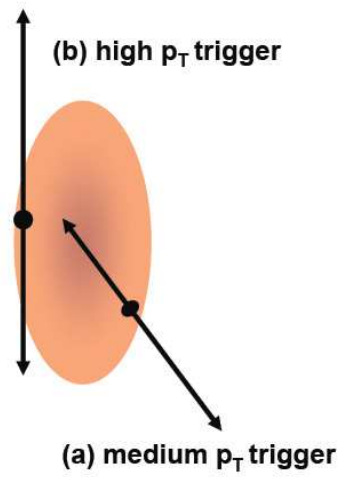
**Figure 6.11:** *Schematic illustration of the "surface bias" picture. (a) Case of a medium $p_T$ trigger particle; (b) Case of a high $p_T$ trigger particle (See text).*

## 6.3   Jet-Modification for Mesons and Baryons

## in Au+Au Collisions

One of the most interesting results from RHIC has been the observation that proton production at intermediate transverse momentum is significantly enhanced as a function of centrality in Au+Au collisions at $\sqrt{s_{NN}} = 200$ GeV [A$^+$03g]. This increase in the proton yields is $p_T$ dependent. For central Au+Au collisions, high transverse momentum ($p_T > 2 GeV/c$) protons are almost as abundant as pions. Interestingly enough, the proton yields in these regions appear to scale with the number of binary nucleon-nucleon collisions [A$^+$03g]. One may expect such a scaling if proton production is dominated by hard processes and unmodified by the medium. Contrary to the protons and anti-protons, the single particle yields of neutral pions have been found to be significantly suppressed in Au+Au collisions at $\sqrt{s_{NN}} = 200 GeV$ [A$^+$02]. This latter observation has been attributed to jet energy loss in the nuclear collision medium (cf. Ref. [JW05] and references therein).

The large enhancement with $p_T$ and centrality in the $p/\pi$ ratio, and the scaling behavior of protons and anti-protons (sometimes affectionately called the "baryon puzzle" at RHIC) begs the question if protons from jet fragmentation are modified by the medium.

A particular limitation of studying jet-modification via the scaling behavior of single particle yields is, that no shape information for jets can be

deduced. Moreover, in this observable, jet fragments cannot be separated from the other particles in the event. Therefore important effects can be masked by soft particle production, which is still expected to play a significant role in the intermediate transverse momentum range.

The technique of azimuthal correlation functions allows to reconstruct jets statistically and gives access to crucial jet-properties, such as widths and yields. This method can therefore provide much more direct insight into the particle species dependence of jet modification. In this section, jet mediated correlations are examined for identified associated mesons (pions and kaons) and baryons (protons and anti-protons) with unidentified trigger hadrons at $2.5 < p_{T,trig} < 4 GeV/c$.

Representative $\Delta\phi$ distributions for jet-associated baryons (indicated by filled blue circles) and mesons (red filled squares) per trigger hadron are depicted in Fig. 6.12. Panels (a) and (c) report results for central (0-20%) collisions and mid-central (20-40%) jet-functions are shown in panels (b) and (d). The error bands on the data points represent the systematic error from the $v_2$ subtraction. Less jet-associated baryons are found than their meson counterparts. This seems consistent with the expectation that jet fragmentation products are mostly pions. To facilitate shape comparisons for both particle species, the baryon jet pair distributions have been multiplied to match the meson jet pair distributions on the away-side. The multiplication factors are 5 and 2, for the lower associated $p_T$ bin ($1 < p_{t,assoc} < 1.3 GeV/c$,
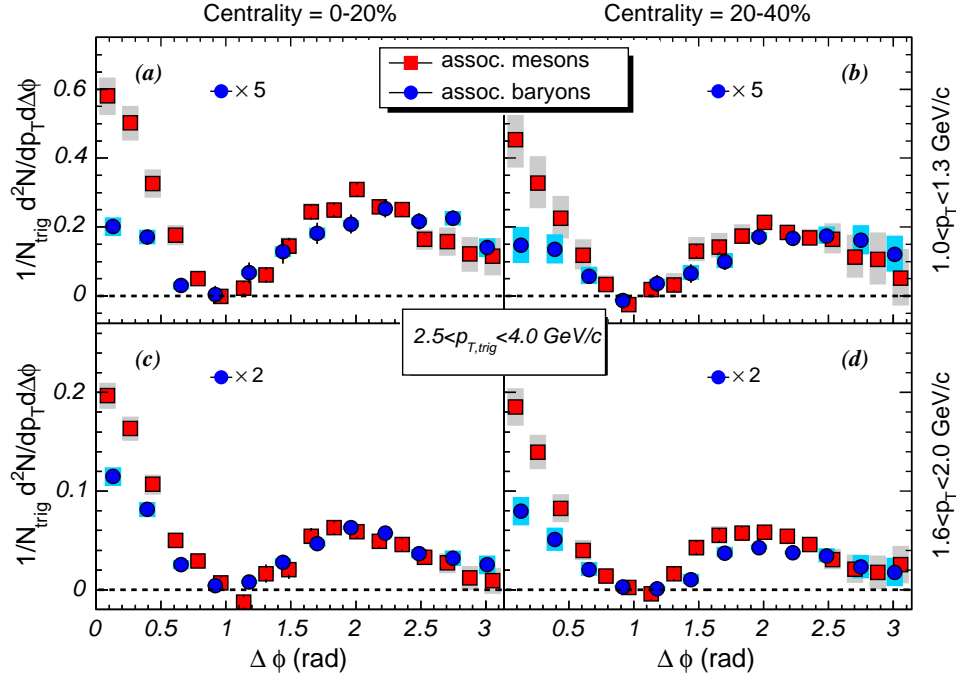
**Figure 6.12:** *Representative $\Delta\phi$ distributions for jet-associated baryons (protons and anti-protons) and mesons (pions and kaons) per trigger particle. Panels (a) and (c) report results for central (0-20%) collisions and mid-central (20-40%) jet-functions are shown in panels (b) and (d).*

top row) and higher associated $p_T$ bin ($1.6 < p_{t,assoc} < 2.0 GeV/c$, bottom row), respectively. This already indicates a strong $p_T$ dependent change in particle composition for jets in Au+Au collisions at $\sqrt{s_{NN}} = 200 GeV$.

The topological information, that can be extracted from Fig. 6.12 is most enlightening. Clearly, jet mediated hadron-meson correlations result in a more asymmetric jet function than hadron-baryon correlations. This is

tantamount to saying that relative to their respective away-side yields, less baryons are found in the near-side jet peak than mesons. The difference in asymmetry between the associated meson and baryon jet-functions becomes less pronounced when the associated particle $p_T$ is raised. This observation could be reflective of trigger bias effects on the near-side, or a change of particle composition in the away-side jet. The more interesting topological result, however, is in the shape of the away-side peaks, which are rather similar for jet-associated meson and baryon correlations. These peaks appear strongly broadened and non-gaussian, with a possible local minimum at $\Delta\phi = \pi$. It is interesting to note, that similar shapes have been observed for jet mediated correlations between unidentified charged hadrons (see the previous section). These results clearly indicate strong medium modification to jet-associated baryons and mesons at intermediate $p_T$ in Au+Au collisions at RHIC and may help to constrain jet-modification models.

Given the yield differences between baryons and mesons, revealed in Fig. 6.12, it seems natural to ask how the conditional yield for these species evolves with centrality and associated particle transverse momentum ($p_{T,assoc}$).

Per trigger yields (CY) for several $p_{T,assoc}$-bins and four centrality selections (0-20%, 20-40%, 40-70% and 70-90%), as indicated, are summarized in Fig. 6.13 The near side conditional yields are shown in the left column and the away-side conditional yields in the right column. The upper row depicts jet-associated baryon yields and the lower row depicts their meson
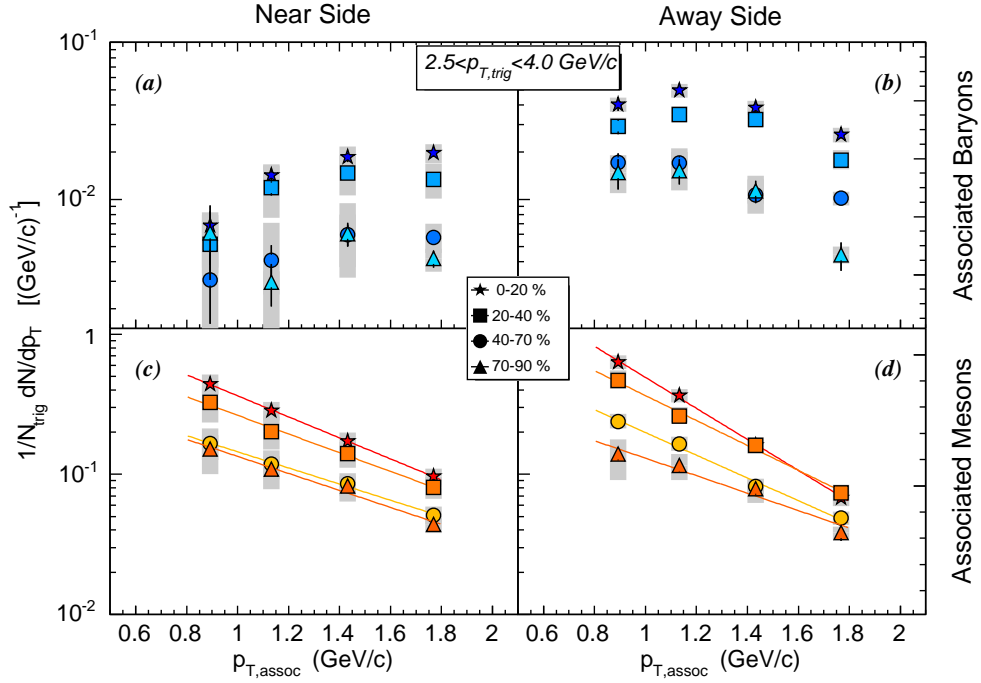
**Figure 6.13:** *Per trigger yields (CY) for several $p_{T,assoc}$-bins and four centrality selections (0-20%, 20-40%, 40-70% and 70-90%).*

counterparts. The solid lines in the lower panels are to guide the eye. Turning first to the jet-associated meson yields (cf. Fig. 6.13(c,d)), we can see that for all four centralities, the near-side yields decrease exponentially with associated particle $p_T$. Very little (if any) apparent slope change of the distributions with centrality is observed. This trend is in agreement with the $p_T$ and centrality dependence of jet-correlated hadron pairs per trigger particle in d+Au collisions (cf. section 6.1). On the away-side, the conditional yields behave differently. While the $p_{T,assoc}$-dependence of the away-side yields is

still exponential, the more central the sample, the steeper this dependence. Such a behavior is consistent with expectations of an away-side yield increase at lower $p_{T,assoc}$ due to parton energy-loss via induced gluon radiation in the medium. The near-side and away-side conditional yields for mesons at a given $p_T$ rise with centrality, in agreement with earlier observations for charged hadrons (compare section 6.2).

Shifting focus to the results for associated baryons, one can clearly distinguish a rising trend of the near-side conditional yields with $p_{T,assoc}$ that seems to saturate at $p_{T,assoc} \approx 1.6 - 1.8$ GeV/$c$. This trend differs substantially from what is observed for jet-associated mesons. However, it is in good qualitative agreement with momentum spectra for $p$ and $\bar{p}$ in quark and gluon jets from $e^+ + e^-$ collisions as measured by the DELPHI collaboration [A+00]. This is evidenced by Fig. 6.14 which depicts momentum spectra for pions, kaons and protons in quark jets (panels (a)-(c), respectively) and gluon jets (panels (d)-(f), respectively). Fig.6.14 is reproduced from Ref. [A+00]. Turning back to Fig. 6.13, it is rather interesting to note, that already for peripheral collisions, the conditional yield distribution of the away-side has a different shape than the near-side. It seems to exhibit a plateau at about $p_{T,assoc} \approx 1.1$ and decreases for $p_{T,assoc} > 1.2$. Since little to no medium modification is expected in peripheral collisions, this result might suggest a trigger bias origin for the steep near-side drop-off in the associated baryon yields at low $p_T$.

Since the associated meson yields in Fig. 6.13 fall exponentially, even
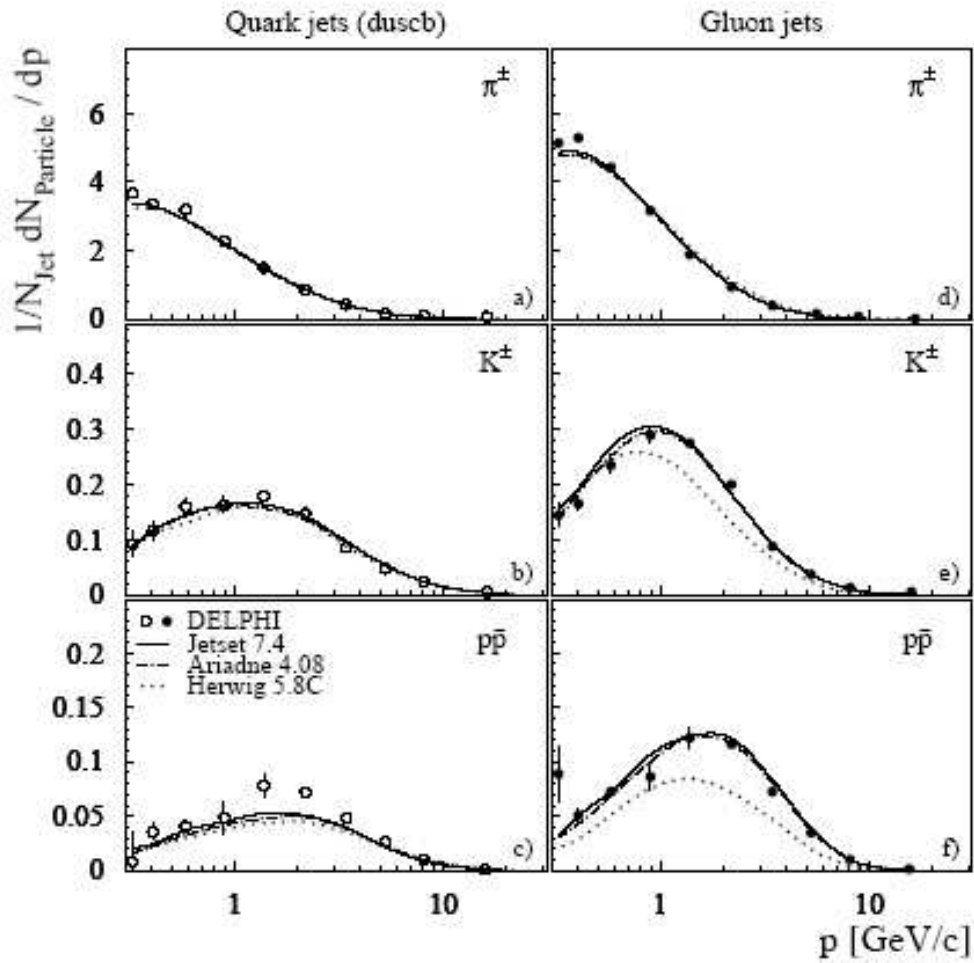
**Figure 6.14:** *Momentum spectra of pions, kaons and protons in quark jets (panels (a),(b),(c), respectively) and gluon jets (panels (d),(e),(f), respectively), in $e^+ + e^-$ collisions. Measurement by the DELPHI collaboration. Figure reproduced from Ref. [A+00].*

small $p_T$-dependent modifications with centrality can be easily identified as slope changes. The complicated shape of the away-side conditional yield

distributions for jet-associated baryons makes it more difficult to discern such effects. However, a yield change (either increase or decrease) of the order of what is observed for mesons, cannot be ruled out from these distributions, when the statistical and systematic errors are taken into account.

To further probe for medium modification of meson and baryon conditional yields, it is instructive to investigate how the ratio of jet-associated baryons to jet-associated mesons behaves with $p_T$. Figure 6.15 shows these ratios for the near-side (left panel) and away-side (right panel) for three centrality bins (0-20% black circles, 20-40% gray squares and 70-90% open triangles). In peripheral collisions, the near side baryon to meson conditional yield ratio compares well with the singles $p/\pi$ ratio in gluon jets from $e^+ + e^-$ collisions (solid black line) [A$^+$00], but is larger on the away-side. One also immediately notices, that the baryon to meson conditional yield ratio rises with $p_T$ and centrality for the near-side as well as the away-side. However, this rise is much more pronounced for the away-side, possibly indicating that the medium modifies the particle species composition within the away-side jet. These results might indicate, that at least some of the baryon enhancement observed in the measurement of the single particle distributions, arises from different medium induced yield modifications of the jet-associated baryons and mesons.

In conclusion, it has been demonstrated that the high energy density medium in Au+Au collisions at $\sqrt{s_{NN}} = 200 GeV$ modifies the distribution
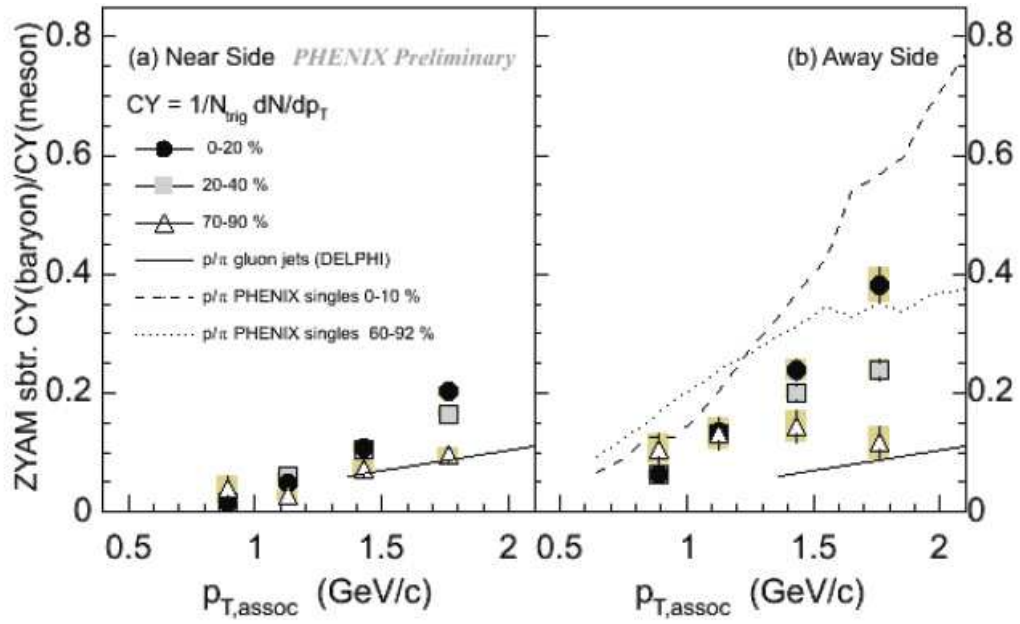
**Figure 6.15:** *Ratio of jet associated baryons to jet associated mesons for three centrality bins (0-20% black circles, 20-40% gray squares and 70-90% open triangles).*

of jet-associated mesons and baryons per trigger hadron, both in shape and yield. These results provide stringent tests for theoretical models aiming to describe jet-modification at RHIC.

# 6.4 System Size Dependence of Jet Modification

In the previous two sections (6.2 and 6.3) it has been demonstrated that the high energy density medium in Au+Au collisions at $\sqrt{s_{NN}} = 200 GeV$ strongly modifies jet induced two particle correlations. The modifications are similar for jet-associated mesons and baryons and show qualitative agreement with various model predictions of jet alteration in a strongly interacting QGP [G$^+$03, HW04, A$^+$04c, Sto05, CS$^+$04, RM05, RR06, MW05, KMW05]. These results clearly suggest, that jet-correlation studies hold much promise for reliable estimates of transport coefficients, viscosity or the speed of sound in the medium. Despite the abundance of theoretical predictions, still very little is known from experiment about the mechanistic origin of jet modification at RHIC. A crucial example of great importance is the relative influence that energy density and path length exert on the alteration of jet properties. Both quantities vary with increasing overlap region of the collision. Therefore, the observation of centrality dependent jet modification cannot easily distinguish the predominance of either the energy density or the path-length on the modification process. Moreover, reliable estimates of the path-length dependence for jet modification can serve to constrain jet suppression models. It has been predicted, that the energy loss of a parton in a static QCD medium should be proportional to the square of the path length

traversed [BSZ00]. Calculations that take the expansion of the medium into account yield a linear path length dependence, instead [GLV02]. In this context, it is interesting to recall, that jet-modification might depend on the inclination angle of the jet with respect to the flow field (cf. Ref. [A$^+$04c]). Such modifications might further complicate the path length dependence.

A first attempt to study path-length effects at fixed energy density, employed two particle correlations relative to the reaction plane [A$^+$04a]. The underlying assumption for these studies is that triggering on a particle perpendicular (parallel) to the reaction plane, preferentially selects jets aligned with the long (short) axis of the elliptic overlap zone. Indeed, an initial sensitivity to path length effects was demonstrated [A$^+$04a]. In this section, a complementary approach that does not suffer from reaction plane resolution effects is suggested.

Measurements of the transverse energy per particle by SPS and RHIC experiments show very little change over the range $\sqrt{s_{NN}} \approx 20 - 200 GeV$ [A$^+$05c]. This seems to suggest, that almost all of the beam energy increase goes into particle production. Recently, the PHOBOS collaboration compared a preliminary measurement of the charged particle pseudorapidity density in Cu+Cu collisions at $\sqrt{s_{NN}} = 200 GeV$ with their previous measurement in Au+Au collisions at the same energy and for the same number of participating nucleons $N_{part}$. Essentially no difference within errors was found [R$^+$]. In combination, these observations indicate that for the same

$N_{part}$, matter with very similar energy density is created in both collision systems. However, since the overlap regions in Au+Au and Cu+Cu are different for the same number of participating nucleons, the effective path lengths for hard scattered partons in this matter should also differ. Systematic comparisons of jet-pair correlations from Cu+Cu and Au+Au collisions can therefore serve as a complementary tool for the investigation of path length effects on jet modification. An initial comparison is attempted in this section.

Distributions of associated charged hadrons (at $1 < p_{T,assoc} < 2.5 GeV/c$) per trigger hadron ($2.5 < p_{T,trig} < 4 GeV/c$) have been obtained for several centrality selections in Cu+Cu collisions at $\sqrt{s_{NN}} = 200 GeV$. A subset of three representative jet pair distributions (in $\Delta\phi$) is shown in Fig. 6.16. The red data points indicate the distribution for peripheral Cu+Cu collisions (40-80%). This jet-pair distribution evidences two well defined peaks at $\Delta\phi = 0$ and $\Delta\phi = \pi$, reminiscent of jet-correlations in d+Au or peripheral Au+Au collisions. The green and blue data points represent results for a mid-central (20-40%) and central (0-10%) event sample. These latter distributions are much broader on the away-side than their peripheral counter part. No apparent change of the near-side peak with centrality is observed for all three distributions in Fig. 6.16. All in all, this seems to suggest strong away-side modification for jet-induced two particle correlations in Cu+Cu. The modification pattern appears to be very similar to what has been observed for Au+Au collisions (see section 6.2).
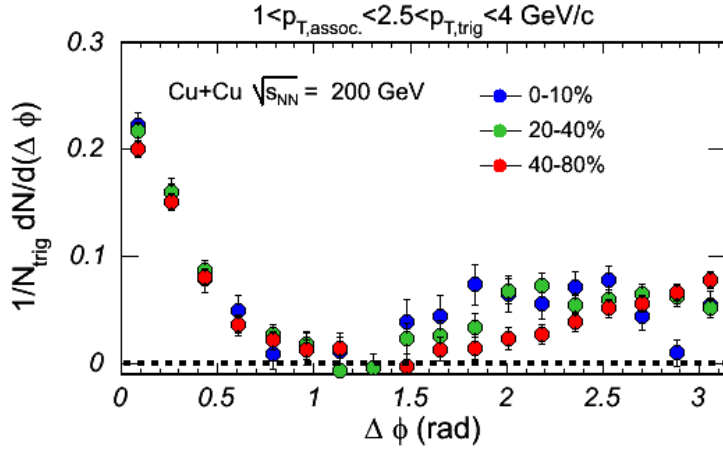
**Figure 6.16:** *Cu+Cu charged hadron jet-pairs per trigger particle as a function of Δφ for three centralities (0-10% blue data points, 20-40% green data points and 40-80% red data points).*

A more quantitative comparison of a jet-pair distribution from Cu+Cu collisions to its partner from Au+Au (at $N_{part} \approx 74$) can be seen in Fig. 6.17. In both cases, trigger particles at $2.5 < p_{T,trig} < 4 GeV/c$ have been correlated with associated particles at $1 < p_{T,assoc} < 2.5 GeV/c$. These correlations do not seem to show a strong dependence on the system size, thereby suggesting that energy density is the predominant factor for jet modification. However, small differences between these distributions can be observed. The jet-function for Au+Au seems slightly enhanced in yield and possibly even broader on the away-side. This is in line with naive expectations of a larger effective path-length for jet alteration in Au+Au. A simple estimate of angle
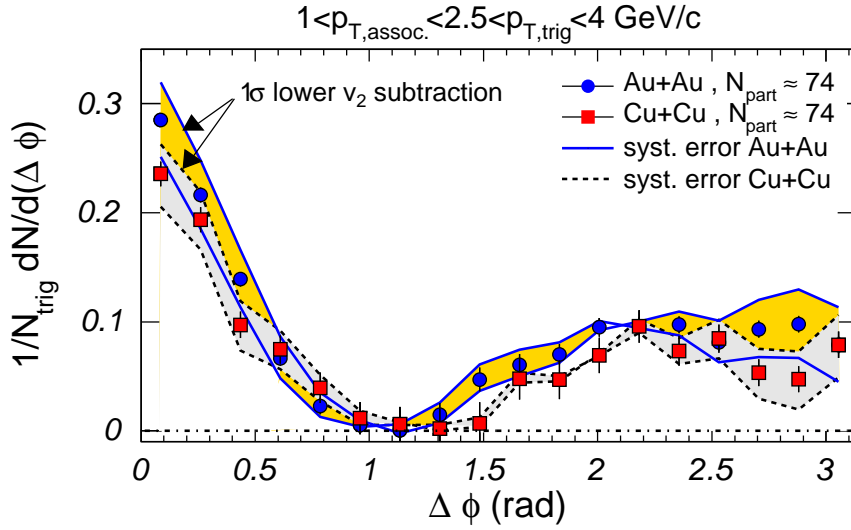
**Figure 6.17:** *Comparison of jet-pair distributions per trigger particle for Au+Au (blue points) and Cu+Cu (red squares) collisions at $N_{part} \approx 74$. The solid (dashed) lines represent the Au+Au (Cu+Cu) jet-pair distributions, that one would obtain by subtracting a harmonic contribution with an amplitude that has been lowered (indicated on plot) or raised by one unit of the systematic error.*

integrated path-lengths can be made with a Glauber model and the assumption of an elliptic overlap region. Such an exercise yields a difference in effective path length of 20-30% between both systems at $N_{part} \approx 74$. It should be noted, however, that this estimate does assume uniform jet production in the overlap region. To the extend, that triggering on a high $p_T$ particle selects near-side jets preferentially from the surface of the fireball [DLP05], the above assumed value of the effective path length difference between the two systems would constitute an upper estimate. Even with the

relatively large systematic errors from the $v_2$ subtraction on both distribu-tions, though, it appears fair to say that a quadratic path-length dependence for jet modification seems disfavored by these data.
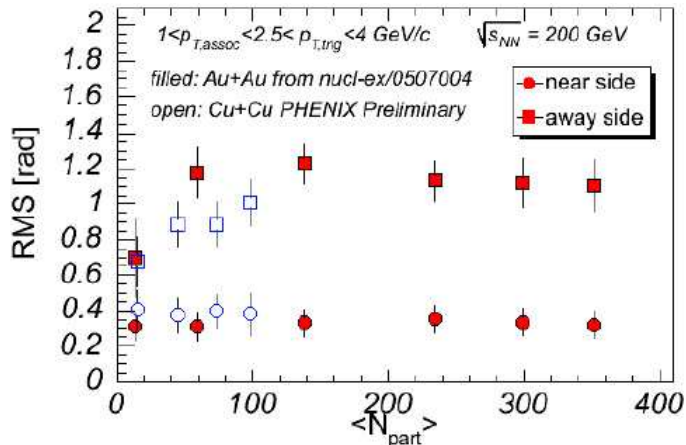


**Figure 6.18:** *Comparison of RMS widths from near- and away-side peaks for Cu+Cu and Au+Au collisions (see text).*

A summary of $N_{part}$ dependent away-side broadening in both systems is given in Fig. 6.18. Filled red data points indicate the RMS widths from section 6.2. Also shown are the corresponding widths from the Cu+Cu anal-ysis as open symbols. Circles denote the near-side widths and squares show the widths for the away-side peaks. In brief, the near-side widths for both systems seem to agree and do not appear to change with centrality within the errors. Centrality dependent broadening is evidenced by the away-side widths and seems to show a smooth dependence with $N_{part}$.

In conclusion, jet modification has been studied as a function of colliding

system size. It is suggested, that such studies provide a complementary method of attack for investigating path length dependent jet alteration. Jet-pair distributions in Au+Au and Cu+Cu collisions have been obtained for the same $p_T$ selections. In semi-central and central collisions, the away-side jet appears strongly broadened in both systems. For the same number of participating nucleons ($N_{part} \approx 74$), the away-side modifications do not show a striking system size dependence, therefore suggesting that energy density plays a major role in jet modification. Small, but observable differences between the two distributions serve to constrain models which predict strong path-length dependent jet modification.

## Chapter 7

# Conclusion and Outlook

## 7.1 Conclusions

The main goal of this work has been to utilize jet modification as a short wavelength tomographic probe of the high energy density medium, created in heavy ion collisions at RHIC. To this end, the two particle correlation function method has been used to measure correlations due to jets and elliptic flow in d+Au, Au+Au and Cu+Cu collisions. The overall strategy has been to search for modification of jet-induced correlations by the hot and dense medium produced in Au+Au and Cu+Cu collisions. These modifications can then be compared to their analogues in d+Au collisions, where only cold nuclear matter effects are expected. Any signal observed in Au+Au and Cu+Cu collision that differs from the d+Au correlation pattern, can then be attributed to the high energy density medium formed in heavy ion collisions.

This strategy has been very successful and several important conclusions have been drawn.

As a first step, the correlation structures in d+Au collisions have been put under the magnifying glass and have been found to behave very much as expected for jet physics. Within errors, no modification of jet properties has been found.

A novel decomposition technique has been utilized to separate the jet mediated correlations in Au+Au and Cu+Cu collisions from the underlying harmonic correlations due to elliptic flow. The extracted jet pair distributions for peripheral events, where little to no high energy density matter is produced, are very similar in yield and shape to the jet pair distributions measured in d+Au collisions. For mid-central and central collisions, where significantly more matter at higher energy densities is produced, the jet-pair distributions at intermediate transverse momentum ($p_T$) are strongly broadened on the away-side and suggest a possible local minimum at $\Delta\phi = \pi$. Jet-associated mesons and baryons are modified by the medium in very similar fashion. This discovery agrees qualitatively with several model predictions for jet modification in a strongly interacting Quark Gluon Plasma, including the conjecture, that fast partons can induce "mach cones" as they traverse the QCD fluid with essentially the speed of light. A study of the system size dependence of jet-correlations has been proposed as a complementary tool to investigate path-length effects on jet alteration. A systematic comparison of

jet pair distributions in Au+Au and Cu+Cu collisions for the same selection of $p_T$ and number of participating nucleons shows no large dependence on entrance channel. This observation is interpreted as an indication that it is the energy density of the fireball that plays a major role in jet modification. Small but observable differences between these distributions can serve to constrain models invoking large path-length dependent energy loss.

These new experimental results provide an important basis for further study of the transport properties of the high energy density matter produced in heavy ion collisions at RHIC.

## 7.2   Suggestions for Further Study

This work has attempted a systematic comparison of jet-properties for a variety of colliding systems at $\sqrt{s_{NN}} = 200 GeV$ by means of two particle azimuthal correlation functions. The basic characteristic trends of jet-induced correlations have been traced in d+Au collisions and their centrality dependence has revealed little (if any) cold nuclear matter modification. For Au+Au collisions, substantial modifications of baryons and mesons associated with the away-side jet have been observed. These findings have been interpreted as evidence that jets interact strongly with the high energy density medium. A study of the system size dependence of jet correlations has revealed initial complementary insight into the path-length dependence of jet

modification.

So what are the next steps?

- Much excitement has evolved around the question of jet-induced conical flow in Au+Au collisions at RHIC, since such a phenomenon, if confirmed, could grant access to the speed of sound in the collision medium. Novel techniques are needed to further dissect the thought-provoking away-side structures reported on in this work. These techniques need to allow for reliable discrimination between the many (and rather different) jet modification models. Three particle correlations have been demonstrated to reveal additional topological insight over and above the shape information available from particle pair measurements [L$^+$94]. Such studies hold much promise in distinguishing cone geometries from other away-side structures. The two large RHIC experiments have already started such an analysis trajectory [Aji05, Ule05].

- Jet-induced correlations involving identified particles at intermediate and moderately high transverse momentum can potentially serve to constrain models for jet modification. It would therefore be useful to further elaborate the correlation measurements for identified particles that have been initiated in this work. Specifically, one should extend correlation measurements, that fully identify trigger and associated partner particles, to the higher transverse momentum region.

In this regard, it will be important to carefully chart out modification patterns in the correlation function with respect to all permutations of particle species. In PHENIX, high transverse momentum ($p_T > 2.5 GeV/c$) charged particle identification is done using the ToF detector, which has a relatively small aperture. Correlation studies that rely on the ToF detector suffer from acceptance losses in exactly the region of the correlation function that has been identified as the most interesting for jet modification. A study, that utilizes the full PHENIX acceptance, correlates neutral pions ($\pi^0$'s, reconstructed via the detection of their decay photons in the Electromagnetic Calorimeter) with associated identified charged hadrons. Since the author had a few spare cpu cycles to burn, an "amuse-geule" of $\pi^0$ triggered correlation functions for 30-60% Au+Au collisions at $\sqrt{s_{NN}} = 200 GeV$ is provided in Figs. 7.1 and 7.2 for associated mesons and baryons at $0.8 < p_{T,assoc} < 2.5 GeV/c$, respectively. A clear $\pi^0$ peak is visible in the invariant mass distribution of photons selected from the same event (black data points, panel (a)) and absent in the analogous background distribution of photons from unrelated events (green data points, panel (a)). For the $\pi^0$ transverse momentum range depicted in these Figs. ($3 < p_{T,trig} < 5 GeV/c$), the signal to background ratio is a very good 1.25. Looking at panel (c) in Figs. 7.1 and 7.2, we can see that the correlation function for associated mesons is slightly more asymmetric

than its baryon counterpart, indicating that the differences in associ-
ated meson and baryon jet pair distributions, reported in section 6.3
of this work, reach out to the higher trigger $p_T$ region. No separation
of the jet-signal from the background has been attempted, here. It
is hoped, that these results will stimulate the interest in further and
more detailed investigations of $\pi^0$ triggered correlation functions for
identified associated particles.
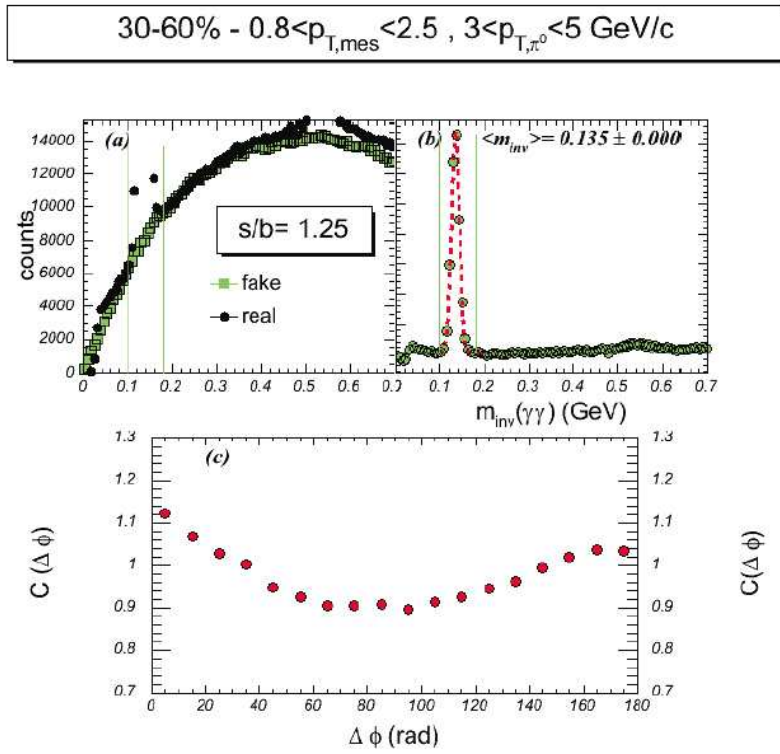


**Figure 7.1:** *Correlation functions of a $\pi^0$-trigger at $3 < p_{T,trig} < 5 GeV/c$ with an associated meson at $0.8 < p_{T,assoc} < 2.5 GeV/c$ (panel (c)). The $\pi^0$ is reconstructed via the invariant mass distribution from photon pairs (panel (a)).*
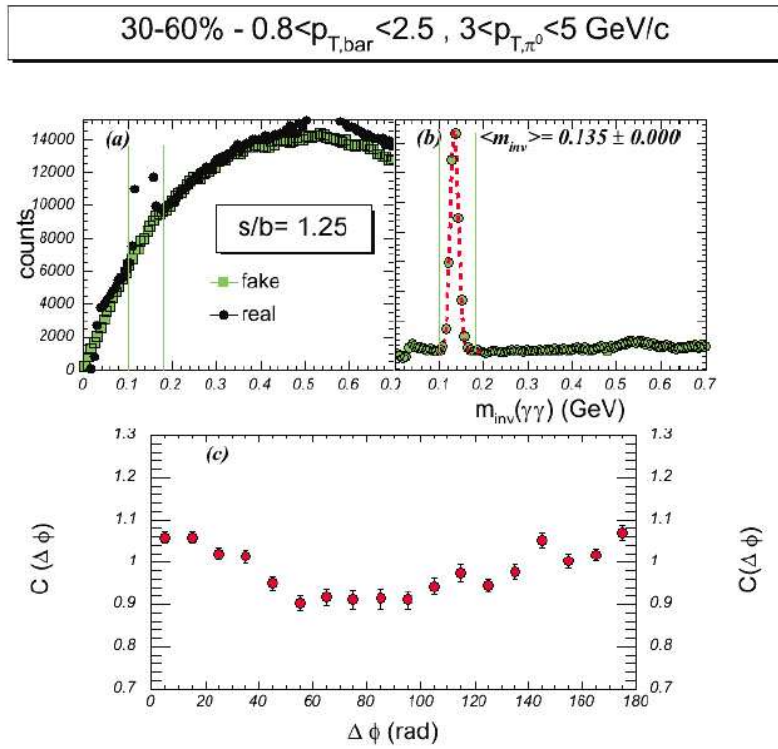
**Figure 7.2:** *Correlation functions of a $\pi^0$-trigger at $3 < p_{T,trig} < 5 GeV/c$ with an associated baryon at $0.8 < p_{T,assoc} < 2.5 GeV/c$ (panel (c)). The $\pi^0$ is reconstructed via the invariant mass distribution from photon pairs (panel (a)).*

- Another area that needs further work, is the extension of particle species for jet correlation measurements. An important example is the utilization of the $\phi$-meson as associated partner particle. The $\phi$-meson is characterized by a mass close to the proton mass and, since it is a meson, two constituent quarks. The proton, as a baryon, is made of three constituent quarks. A comparison of correlations involving the $\phi$

and protons, therefore, hold much promise to constrain issues of quark recombination on jet modification.

- Finally, the study of system size effects on jet modification could be intensified. Once the full data set for Cu+Cu collisions will be reconstructed, it is hoped that the large increase in statistics will allow for much more differential investigations.

# Bibliography

[A+79a]   A. L. S. Angelis et al. *Physica Scripta*, 19:116, 1979.

[A+79b]   D. Antreasyan et al. *Phys. Rev.*, D19:764, 1979.

[A+80]    A. L. S. Angelis et al. *Phys. Lett.*, B97:163, 1980.

[A+97]    P. Abreu et al. *Phys. Lett.*, B407:174–184, 1997.

[A+00]    P. Abreu et al. *Eur. Phys. J.*, C17:207, 2000.

[A+02]    K. Adcox et al. *Phys. Rev. Lett.*, 88:022301, 2002.

[A+03a]   K. Adcox et al. *Nucl. Instrum. Meth.*, A499:469–479, 2003.

[A+03b]   C. Adler et al. *Nucl. Instrum. Meth.*, A499:433–436, 2003.

[A+03c]   C. Adler et al. *Phys. Rev. Lett.*, 90:032301, 2003.

[A+03d]   C. Adler et al. *Phys. Rev. Lett.*, 90:082302, 2003.

[A$^+$03e]    S. S. Adler et al. *Phys. Rev. Lett.*, 91:182301, 2003.

[A$^+$03f]    S. S. Adler et al. *Phys. Rev. Lett.*, 91, 2003.

[A$^+$03g]    S S Adler et al. *Phys. Rev. Lett.*, 91:172301, 2003.

[A$^+$03h]    M. Aizawa et al. *Nucl. Instrum. Meth.*, A499:508–520, 2003.

[A$^+$03i]    M. Allen et al. *Nucl. Instrum. Meth.*, A499:549–559, 2003.

[A$^+$03j]    L. Aphecetche et al. PHENIX calorimeter. *Nucl. Instrum. Meth.*, A499:521–536, 2003.

[A$^+$03k]    S H Aronson et al. *Nucl Instrum Meth.*, A499:480–488, 2003.

[A$^+$04a]    J. Adams et al. *Phys. Rev. Lett.*, 93:252301, 2004.

[A$^+$04b]    K. Adcox et al. *Phys. Rev.*, C69:024904, 2004.

[A$^+$04c]    N. Armesto et al. *Phys. Rev. Lett.*, 93:242301, 2004.

[A$^+$05a]    J. Adams et al. *Nucl. Phys.*, A757:102–183, 2005.

[A$^+$05b]    K. Adcox et al. *Nucl. Phys.*, A757:184–283, 2005.

[A$^+$05c]    S. S. Adler et al. *Phys. Rev.*, C71:034908, 2005.

[A$^+$05d]    S. S. Adler et al. 2005. nucl-ex/0510021.

[A$^+$05e]    N. N. Ajitanand et al. *Phys. Rev.*, C72:011902, 2005.

[A+05f]   I. Arsene et al. *Nucl. Phys.*, A757:1–27, 2005.

[Acc02]   Alberto Accardi, 2002. hep-ph/0212148.

[Aji03]   N. N. Ajitanand. *Nucl. Phys.*, A715:765–768, 2003.

[Aji05]   N. N. Ajitanand. 2005. nucl-ex/0511029.

[App86]   D. A. Appel. *Phys. Rev.*, D33:717, 1986.

[B+05]   B. B. Back et al. *Nucl. Phys.*, A757:28–101, 2005.

[BEF+04]   J. Bielcikova, S. Esumi, K. Filimonov, S. Voloshin, and J. P. Wurm. *Phys. Rev. C69*, C69:021901, 2004.

[Bjo82]   J. D. Bjorken, 1982. FERMILAB-PUB-82-059-THY.

[Bjo83]   J. D. Bjorken. *Phys. Rev.*, D27:140, 1983.

[Bla86]   J. P. Blaizot. *Phys. Rev.*, D34:2739, 1986.

[BMRS03]   Peter Braun-Munzinger, Krzysztof Redlich, and Johanna Stachel, 2003. nucl-th/0304013.

[BO04]   N. Borghini and J. Y. Ollitrault. 2004.

[BPLF04]   G. G. Barnafoldi, G. Papp, P. Levai, and G. Fai. *J. Phys.*, G30:S1125–S1128, 2004.

[BSZ00]    R. Baier, D. Schiff, and B. G. Zakharov. *Ann. Rev. Nucl. Part. Sci.*, 50:37–69, 2000.

[C⁺75]     J. W. Cronin et al. *Phys. Rev.*, D11:3105, 1975.

[C⁺94]     M. D. Corcoran et al. *Phys. Lett.*, B259:209, 1994.

[C⁺05]     Paul Chung et al. *PHENIX Analysis Note 319*, 2005.

[Chi03]    M. Chiu. *Nucl. Phys.*, A715:761, 2003.

[CS⁺04]    J. Casalderrey-Solana et al. 2004. hep-ph/0411315.

[DLP05]    Andrea Dainese, Constantin Loizides, and Guy Paic. 2005. hep-ph/0511045.

[FFF77]    R. P. Feynman, R. D. Field, and G. C. Fox. *Nucl. Phys.*, B128:1, 1977.

[G⁺03]     V. Greco et al. *Phys. Rev. Lett.*, 90:202301, 2003.

[Gho50]    S. N. Ghoshal. *Phys. Rev.*, 80:939–942, 1950.

[GLV02]    M. Gyulassy, P. Levai, and I. Vitev. *Phys. Lett.*, B538:282–288, 2002.

[H⁺04]     T. Hirano et al. 2004. nucl-th/0404039.

[Han01]    S. Hands. The Phase Diagram of QCD. *Contemp. Phys.*, 42:209–225, 2001.

[HKH+01]  P. Huovinen, P. F. Kolb, Ulrich W. Heinz, P. V. Ruuskanen, and S. A. Voloshin. *Phys. Lett.*, B503:58, 2001.

[HT]      R.C Hwa and Z. Tan. nucl-th/0503060.

[HW04]    R. C. Hwa and C. B. Wang. *Phys. rev.*, C70:024905, 2004.

[HY04]    Rudolph C. Hwa and C. B. Yang. *Phys. Rev. Lett.*, 93:082302, 2004.

[IT06]    Michael Issah and Arkadij Taranenko. 2006. nucl-ex/0604011.

[Jia03]   Jiangyong Jia. PhD thesis, Stony Brook University, 2003.

[JW05]    Peter Jacobs and Xin-Nian Wang. *Prog. Part. Nucl. Phys.*, 54:443–534, 2005.

[K+79]    C. Kourkoumelis et al. *Nucl. Phys.*, B158:39, 1979.

[K+01]    P. F. Kolb et al. *Nucl. Phys.*, A696:197–215, 2001.

[Kar02]   Frithjof Karsch. *Lect. Notes Phys.*, 583:209, 2002.

[KMW05]   V. Koch, A. Majumder, and Xin-Nian Wang. 2005. nucl-th/0507063.

[L+93]    Roy A. Lacey et al. *Phys. Rev. Lett.*, 70:1224, 1993.

[L+94]    J Lauret et al. *Phys. Lett.*, B339:22, 1994.

[Lac05]    Roy A. Lacey. 2005. nucl-ex/0510029.

[M+02]    J. Mitchell et al. *Nucl. Instrum. Meth.*, A482:491–512, 2002.

[MW05]    A. Majumder and Xin-Nian Wang. 2005. nucl-th/0507062.

[N+94]    D. Naples et al. *Phys. Rev. Lett.*, 72, 1994.

[Oll92]    Jean-Yves Ollitrault. *Phys. Rev.*, D46:229–245, 1992.

[Oll95]    J.-Y. Ollitrault. *Nucl. Phys.*, A590:561c, 1995.

[P+98]    A. M. Poskanzer et al. *Phys. Rev.*, C58:1671–1678, 1998.

[QV04]    Jian-wei Qiu and Ivan Vitev. 2004. hep-ph/0405068.

[R+]    G. Roland et al. Proc. 18th Intl. Conf. on Ultrarelativistic Nucleus-Nucleus Collisions, Quark Matter 2005, nucl-th/0510042.

[Rak04]    Jan Rak. *J. Phys.*, G30:S1309, 2004.

[RM05]    Jorg Ruppert and Berndt Muller. *Phys. Lett.*, B618:123–130, 2005.

[RR06]    Thorsten Renk and Jorg Ruppert. *Phys. Rev.*, C73:011901, 2006.

[S+90]    C. Stewart et al. *Phys. Rev.*, D42, 1990.

[S+92]    P. B. Straub et al. *Phys. Rev. Lett.*, 68:452, 1992.

[SG86]    H. Stoecker and W. Greiner. *Phys. Rept.*, 137:277, 1986.

[Shu80]   Edward V. Shuryak. *Phys. Rept.*, 61:71, 1980.

[Sta05]   P. Stankus. Technical report, PHENIX Technical Note 412, 2005.

[Sto05]   H. Stoecker. *Nucl Phys.*, A750:121, 2005.

[T$^+$01]   D. Teaney et al. 2001. nucl-th/0110037.

[TA05]   C. Targett-Adams. 2005. hep-ex/0507024.

[Tan06]   M. J. Tannenbaum. *Internal Phenix Analysis Note*, 487, 2006.

[Ule05]   Jason G. Ulery, 2005. nucl-ex/0510055.

[W$^+$91]   S. Wang et al. *Phys. Rev.*, C44:1091–1095, 1991.

[WG92]   X.-N. Wang and M. Gyulassy. *Phys. Rev. Lett.*, 68:1480, 1992.